

Faint, illegible text on the left page, possibly bleed-through from the reverse side.

## Table and Figure Captions

Table 1. Summary of key findings and statistical results.

Figure 1. Graphical representation of the data trends over time.

Table 2. Detailed breakdown of the experimental parameters and their effects.

Figure 2. Comparison of the two groups under different conditions.

Table 3. Final results and conclusions drawn from the study.

## Table and Figure Captions

- Fig. 1.1 The proton-proton reaction chain. Reaction flow and branching ratio are shown.
- Fig. 1.2 The CNO cycle. Reaction flow and branching ratio are shown.
- Fig. 1.3 Expected solar neutrino spectra at the earth from the SSM [ref 1-5] are shown for each reaction. Solid and dotted lines indicate p-p chain and CNO cycle reactions, respectively. Flux units are [ $\text{cm}^2/\text{sec}/\text{MeV}$ ] for continuum and [ $\text{cm}^2/\text{sec}$ ] for line spectra ( ${}^7\text{Be}$  and pep neutrinos).
- Fig. 1.4 Solar neutrino flux observed by  ${}^{37}\text{Cl}$  experiment [ref 1-2] from 1970 (run 18) to 1990 (run 114) is plotted (white circles with error bars) in units of  ${}^{37}\text{Ar}$  production rate (background is not subtracted) and in units of SNU (1 SNU =  $10^{-36}$  captures/atom/sec). Sun-spot numbers (dashed line) are inversely super-imposed with an arbitrary normalization.
- Fig. 1.5 Extraction procedures of germanium atoms are compared for SAGE and GALLEX experiments.
- Fig. 3.1 Solar neutrino spectra distorted by neutrino oscillations are shown for typical just-so oscillation parameters ( $\delta m^2, \sin^2 2\theta$ ) = ( $8 \times 10^{-11} \text{eV}^2, 1$ ).
- Fig. 3.2 The regions where neutrino oscillations can be tested by various neutrino sources are shown in the  $\delta m^2$ - $\sin^2 2\theta$  plane. "H", "O" and "V" indicate the horizontal, orthogonal and vertical part in the MSW region, respectively.
- Fig. 3.3 Diagrams for neutrino elastic scattering. Electron type neutrinos have charged current interactions (a) or (b) in matter.
- Fig. 3.4 Excluded region [ref 1-17] in  $\delta m^2$ - $\sin^2 2\theta$  plane by the study of day/night flux variation in Kamiokande is shown (90% C.L.).
- Fig. 4.1 Cross sections of dominant neutrino scattering in water below 20 MeV are shown.
- Fig. 4.2 Kinematical opening angles of neutrino-electron elastic scattering are shown for various energies of incident neutrino in terms of recoil electron total energy.
- Fig. 4.3 Schematic view of the Kamiokande tank and cavity are shown. Units in the figure are [mm].
- Fig. 4.4 Schematic view of new 20-inch PMT is shown. Units in the figure are [mm].
- Fig. 4.5 Bleeder-chains for Kam-2 PMT (left side) and new PMT (right side) are compared.
- Fig. 4.6 Electron trajectories simulated for Kam-2 PMT dynode.
- Fig. 4.7 Typical transit time spread obtained by new 20-inch PMT [ref 4-13].

- Fig. 4.8 Typical pulse height distribution of new 20-inch PMT [ref 4-13]. One photo-electron peak is clearly seen.
- Fig. 4.9 The effect of magnetic field on the performance of new 20-inch PMTs are shown [ref 4-13].
- Fig. 4.10 The dependence of cathode current on the photo-electron conversion point is shown in (a) [ref 4-13]. Position is defined according to an opening angle from the center on the photo-cathode semi-sphere. The dependence of anode pulse height (relative gain) on the conversion point is shown in (b) for several PMTs [ref 4-13].
- Fig. 4.11 Timing resolution as a function of pulse-height is shown for Kam-2 PMT with Kam-2 electronics (dots), Kam-2 PMT with Kam-3 electronics (dashes) and new PMT with Kam-3 electronics (solid). New PMT drastically improved timing resolution in the entire pulse-height region, and new electronics improved timing resolution around 0.1 photo-electron.
- Fig. 4.12 Schematic view of light reflectors installed for Kam-3 is shown. Materials used are also shown.
- Fig. 4.13 Vertex resolution for electron as a function of electron total energy is shown. Precise vertex reconstruction was applied to the Monte Carlo events for the comparison. Dotted, dashed and solid lines denote Kam-2 gain $\times$ 1, Kam-2 gain $\times$ 2 and Kam-3 vertex resolution, respectively.
- Fig. 4.14 Angular resolution for electron as a function of electron total energy is shown by dotted (Kam-2 gain $\times$ 1), dashed (Kam-2 gain $\times$ 2) and solid (Kam-3) lines.
- Fig. 4.15 Energy resolutions of Kam-2 gain $\times$ 1 (dots), Kam-2 gain $\times$ 2 (dashes) and Kam-3 (solid) are shown as a function of electron total energy.
- Fig. 4.16 Multi-photon effect on energy resolution is schematically shown. Typical geometry causing vertex dependency of the energy scale is used. Kam-2 (no reflector) observes same number of hits and also same number of photons in both near and far PMT plane. Kam-3 (with reflector) catches larger number of photons due to reflectors, and larger number of hits in the case of far PMT plane, but number of hits in the case of near PMT plane does not increase. Therefore, number of photons will offer better energy resolution in ideal case (if we can count number of photons correctly), but number of hits will not improve energy resolution so much.
- Fig. 4.17 Typical Cherenkov ring image of 10 MeV electron is shown by a perspective drawing and exploded view. Ideal (opening angle is 42°) Cherenkov ring is shown in the perspective drawing. Hit PMT is shown by a circle and the size of the circle is proportional to its pulse height.

- Fig. 4.18 On-line data flow is schematically shown. Time and charge information are acquired by micro VAX-II on-line computer through CAMAC interface. The data is first stored and accumulated in the disk system, and then they are transmitted to a VAX station 3800 outside of the mine through an optical link and written to 3480-CMT.
- Fig. 4.19 Signal processing in the ATM module is schematically shown.
- Fig. 4.20 Trigger efficiency curve as a function of electron energy is shown. This is made from Fig. 4.21 by convoluting energy resolution.
- Fig. 4.21 Trigger efficiency curve as a function of electron visible energy is shown. Physics analysis is based on the visible energy. This efficiency was measured by two level trigger calibration. Trigger thresholds were set at two levels: one is the same as normal data taking, and the other is a sufficiently low threshold to guarantee full efficiency around the normal threshold. All data taken with a low threshold were analyzed and visible energies were reconstructed. Then, a trigger flag from the normal threshold was checked and the trigger efficiency as a function of visible energy was obtained.
- Fig. 4.22 Trigger threshold (solid) and analysis threshold (dots) are chronologically shown. Trigger threshold is defined by the energy where the trigger efficiency becomes 50%.
- Fig. 4.23 Decay chains of U-Ra and Th series are shown with half lives and decay modes.
- Fig. 4.24 Flow lines of water purification system (solid) and radon-free air system (dots) are schematically shown. Underlined instruments were newly installed for Kamiokande-3.
- Fig. 4.25 Event rate at a particular reduction step (effectively 6 MeV threshold and 1550 tons of effective volume), where the background is dominated by radon is plotted as a function of data taking time. We installed cooled charcoal in the beginning of December 1990. Solid line is decay curve with  $^{222}\text{Rn}$  half life (3.824 days). Measured radon concentration in the detector water is also shown. Data after the end of December 1990 is used for the solar neutrino analysis.
- Fig. 4.26 Schematic of the radon measurement system. Radon measurement system consists of two parts: water collection system (upper drawing) and radon concentrating system (lower drawing).
- Fig. 4.27 Schematic of Lucas (ZnS paint) counter is shown. Radon-rich gas is inserted through Swage lock. 2-inch PMT is attached on the Lucite window.

- Fig. 4.28 Typical pulse height distribution of radon measurement with Lucas counter (ADC counts vs. number of events) is shown.
- Fig. 4.29 Count rate of radon measurement is shown as a function of data taking time. Intrinsic background measurement was done for the period from 0 to 5500 minutes, and the average noise rate was 0.25 counts/minute. Radon gas extracted from 560 milli-liter of mine water (which contains 280 pCi/l of radon contamination) after 200 hours of decay time was inserted into Lucas cell at 5500 min for the calibration of the detection efficiency. At 14200 min, Lucas cell was vacuumed out and radon gas was extracted from the cell. After decaying the daughter atoms, radon gas extracted from 20 liters of tank water after 32 hours of decay time was inserted at 14500 min.
- Fig. 4.30 Count rates of the radon measurement soon after radon insertion and after vacuum disposition are shown as a function of time. Solid line is fitted result of the shape by a function expected from half lives of atoms in the decay chain.
- Fig. 4.31 Schematic of radon counter using solid state detector is shown. The daughter ions decayed from  $^{222}\text{Rn}$  inside the mesh anode are gathered onto PIN photo-diode by 60 to 100 V of bias voltage.
- Fig. 4.32 Observed energy spectrum by the SSD radon counter is shown. Decaying nuclei are clearly separated due to its good energy resolution.
- Fig. 4.33 SSD radon counter specially constructed for sinking into water is schematically drawn. Micro-porous film prohibits water from entering but allows radon gas to enter.
- Table 5.1 Isotopes accompanying beta and/or gamma rays with an energy greater than 7 MeV are listed with their half lives, emitted particles and released energies. The entries are chosen from nuclei whose mass numbers are less than or equal to 16.
- Fig. 5.1 Vertex difference between fast and precise reconstruction is shown. Data used are the final sample of solar neutrino analysis in Kam-3.
- Fig. 5.2 Opening angle distribution of Cherenkov photons from an incident electron direction obtained from 10 MeV Monte Carlo events is shown. This distribution is used for the direction reconstruction as a likelihood function.
- Fig. 5.3 Effective surface area is shown for the 20-inch PMT with and without the light reflector as a function of light direction. Light acceptance has increased due to light reflectors at angles smaller than 55 degrees.
- Fig. 5.4 Relation of electron total energy and effective number of hit PMTs is plotted. Monte Carlo events were generated in the whole volume and only

- the events reconstructed in the fiducial volume and clearing the gamma cut were used for obtaining the relation.
- Fig. 5.5 PMTs used for muon track reconstruction are schematically illustrated.
- Fig. 5.6 Monte Carlo simulation of electron tracks in water is shown for electrons with 10 MeV of kinetic energy. Twenty electron tracks are overlaid in the figure.
- Fig. 5.7 Pulse-height distribution of one photo-electron signal with Kam-3 electronics is shown. This distribution is obtained from low hit Ni+CF calibration data which statistically guarantees only one photo-electron in the hit signal. This distribution is used for the detector simulation.
- Fig. 5.8 Vertex spread of Ni(n, $\gamma$ )Ni' calibration data taken at the center of the detector is shown as a function of energy, together with that for Monte Carlo events. Vertex spread is defined by the radius where 68% of events are observed inside the sphere. The contribution of Cf background is statistically subtracted from the data. The vertex distribution of Monte Carlo events is well reproducing that of real data.
- Fig. 5.9 Vertex distribution of Ni+CF calibration data taken at the edge of the fiducial volume ( $x, y, z$ )=(0.08m, -0.16m, 4.5m) is compared with the Monte Carlo distribution. The contribution of Cf background is statistically subtracted. The distribution is well reproduced by the Monte Carlo simulation.
- Fig. 5.10 Pulse-height distributions of muons in inner-detector and anti-counter are shown. Muons are selected by inner-total-p.e. > 10000 for anti-counter or anti-total-p.e. > 400 for inner detector. Time difference cut  $\Delta T > 20 \mu\text{sec}$  is also applied to reject ringing noise.
- Fig. 5.11 Vertex distribution of the fast reconstruction step is shown. Region denoted by "cut" (1.5 m on average from the edge of the fiducial volume) is rejected before making the precise vertex reconstruction.
- Fig. 5.12 The "goodness" distribution of the fast reconstruction is compared between normal data and noisy data. The noise cut criteria is set at "goodness"  $\geq 0.4$ .
- Fig. 5.13 Normal data and noisy data are compared for the noise cut parameters  $N_{\text{hit}}/N_{\text{dsc}}$  and  $N_{\text{neg}}/N_{\text{dsc}}$ .
- Fig. 5.14 Vertex distribution of the precise reconstruction step is shown for the events above 6 MeV.
- Fig. 5.15 The definition of x-y-z axes are shown. Z-axis penetrates the center of the cylindrical tank vertically toward upper side. X-y plane is off-set by 60 cm below the center of the inner-detector. But, the fiducial volume in Kam-3 is

- set in a symmetric region ( $-3.37\text{m} \leq z \leq 4.57\text{m}$ ). X-axis is  $30.42^\circ$  rotated to south direction from east direction.
- Fig. 5.16 The energy spectra for full volume (open circles), fiducial volume (black diamonds), after spallation cut (open diamonds) and final sample (black circles) data are shown. Expected spectrum from the SSM [ref 1-5] is also shown (solid line).
- Fig. 5.17 Time difference distribution from muons ( $Q_{\text{eff}} \geq 20000$  p.e.) is shown for the events above 7 MeV. Short (several tens milli-second), middle (a few second) and long (about ten second) decay components are seen.
- Fig. 5.18 Spallation cut criteria is defined as a function of preceding muon pulse height and time difference from the muon. All low energy events in region denoted by "1" are rejected, and events in region "2" are rejected when the distance from the vertex to the muon track is less than 3 meters. Events in region "3" are rejected when the distance is less than 2 meters.
- Fig. 5.19 The distance of the vertex from the muon track is shown for the events before the spallation cut with the conditions of  $Q_{\text{eff}} \geq 20000$  p.e.,  $E_e \geq 9$  MeV and  $\Delta t < 1$  sec. Solid histogram is the observed distribution and dashed histogram is the contribution of random coincidence events which is obtained from random combinations of muons and low energy events (time difference is neglected).
- Fig. 5.20 Timing and spatial correlation of stopping muons (which do not have a decay electron) and low energy events are shown. Solid line in timing distribution is fitted result of the histogram decay curve with  $^{16}\text{N}$  decay ( $\tau=10.29\text{sec}$ ) and flat background. Dashed line in vertex distance distribution is the contribution of random coincidence events whose normalization is determined by the flat component of the decay curve fit.
- Fig. 5.21 The vertex distribution after the spallation cut is shown. Event rate at the edge of the fiducial volume is larger than that at the center of the volume.
- Fig. 5.22 The directional distribution of the events after the spallation cut with respect to the direction of the nearest wall is shown for the events of which the vertex is located within 1 meter from the edge of the fiducial volume (upper histogram) and for the events in the remaining region (lower histogram). Inner direction is defined as  $\cos\theta = -1$ . The excess toward the inner-direction is clearly seen for the events close to the wall.
- Fig. 5.23 Energy spectra after spallation cut are shown for every interval of 100 days of data taking. Only soft component below 8 MeV which is estimated to be originated by radon is decreasing.

- Fig. 5.24 Time differences from muons ( $10000 \leq Q_{\text{eff}} < 20000$ ,  $20000 \leq Q_{\text{eff}} < 40000$ ,  $40000 \leq Q_{\text{eff}}$ ) are shown for the data before and after the spallation cut. Contributions of spallation products are estimated from the decay components (time-correlating components) in the figures.
- Fig. 5.25 Energy spectra of anti-neutrinos from  $^{239}\text{Pu}$ ,  $^{241}\text{Pu}$ ,  $^{238}\text{U}$  and  $^{235}\text{U}$  [ref 5-9] are shown.
- Fig. 5.26 Anti-neutrino spectrum from reactors is shown for Kamioka site.
- Fig. 5.27 Expected energy spectrum of reactor neutrino events in Kamiokande is shown.
- Fig. 6.1 Angular distribution of solar neutrino events (normalized at each energy) is shown for the visible energy of recoil electron; 7, 10 and 15 MeV. These distributions are used for likelihood function of solar neutrino counting.  $\theta_{\text{sun}}$  is the opening angle from the direction to the sun.
- Fig. 6.2 (a) Angular distributions of final sample are shown for 200.3 days of 7.5 MeV threshold data and 314.2 days of 7.0 MeV threshold data. Superimposed solid histograms are expected solar neutrino distributions over the flat background and dashed histograms are the best fits of the excess toward the sun with expected angular distribution scaled by 0.543 (=data/SSM) and 0.591, respectively.  
(b) Same as (a) but for total 514.5 days of Kam-3 data and total 1557 days of Kamiokande data. Best fit values are 0.574 and 0.514, respectively.
- Fig. 6.3 Distribution of relative likelihood as a function of "solar  $\nu$  events" / "all events" for 1557 days of total combined data.
- Fig. 6.4 Energy spectrum of solar neutrino events from 1557 days of total combined data is shown. Data bins above 14 MeV are combined.
- Fig. 6.5 Energy spectrum of solar neutrino events from 1557 days of total combined data with respect to the expected event rate from the SSM [ref 1-5] is shown. Dashed lines are expected from SSM (ratio = 1) and best fit of all combined data (ratio = 0.514).
- Fig. 6.6  $^{37}\text{Ar}$  production rate as a function of sun-spot numbers are shown. Solid line is the best fit line of the correlation as seen in (eq 6-9), and dashed one is the shifted line of the best fit one to obtain the same average value derived by Davis et al.
- Fig. 6.7 Sun-spot numbers as a function of time (year) [ref 6-4] are plotted. Those values are averaged for every one month duration.
- Fig. 6.8 Solar neutrino flux with respect to the SSM prediction is plotted for every 200 days of data. Sunspot numbers for the periods are inversely superimposed in the figure.

- Fig. 6.9 Contour plots of  $\chi^2$  distribution in  $\alpha$ - $\beta$  plane are shown for different and common threshold of 7 data points. 68% and 90% contour lines are obtained by  $\chi^2 = \chi^2_{\min} + 2.28$  (68%) and 4.605 (90%), respectively. One sigma error and 90% C.L. region for a parameter are obtained at  $\chi^2 = \chi^2_{\min} + 1$  (1 sigma), 2.69 (90% C.L.).
- Fig. 6.10 Interesting regions for solar neutrino observation "S" and for anti-neutrino search "B" are illustrated. Region "A" ( $\cos\theta_{\text{sun}} < 0.8$ ) was used for the anti-neutrino search.
- Fig. 6.11 Observed energy spectrum with  $\cos\theta_{\text{sun}} < 0.8$  for 593.7 days of Kam-2 gain $\times$ 2 data is shown. This spectrum was used for deriving a flux limit of solar anti-neutrinos.
- Fig. 6.12 Spectrum independent  $\bar{\nu}_e$  flux limits are plotted. Circle plots show 90% C.L. upper limit of  $\bar{\nu}_e$  flux in unit of (/cm<sup>2</sup>/sec). <sup>8</sup>B solar neutrino spectrum expected by the SSM [ref 1-5] and calculated reactor  $\bar{\nu}_e$  spectrum are superimposed with the different unit of (/cm<sup>2</sup>/sec/MeV). These limits are obtained from Kam-2 gain $\times$ 2 data.
- Fig. 6.13  $\bar{\nu}_e$  flux limit as a ratio with <sup>8</sup>B solar neutrino flux expected by the SSM is plotted in unit of (/MeV). Attention is needed, because the unit of spectrum independent flux limit is (/cm<sup>2</sup>/sec) but the unit of <sup>8</sup>B solar neutrino flux is (/cm<sup>2</sup>/sec/MeV). We assumed that the  $\bar{\nu}_e$  spectrum is distributed over one MeV width, or one does not require a fine binding less than one MeV width. With such an assumption, these spectrum independent flux limits can be considered as normal ratios.
- Fig. 7.1 90% C.L. allowed region in  $\delta m^2$ - $\sin^2 2\theta$  plane by Kamiokande result on average flux (energy spectrum is not used) is shown. Two flavor neutrino oscillation is taken into account. But, earth effect is not considered.
- Fig. 7.2 90% C.L. allowed region in  $\delta m^2$ - $\sin^2 2\theta$  plane by Kamiokande result considering energy spectrum is shown.
- Fig. 7.3 90% C.L. allowed region in  $\delta m^2$ - $\sin^2 2\theta$  plane by Chlorine result from 1970 (run 18) to 1990 (run 114) is shown. Time variation of the flux is not considered.
- Fig. 7.4 90% C.L. allowed region in  $\delta m^2$ - $\sin^2 2\theta$  plane by Gallium result is shown. All available SAGE and GALLEX results are used (i.e. SAGE30 1990, SAGE60 1991, GALLEX-I June 1991 to April 1992 and GALLEX-II August 1992 to April 1993).
- Fig. 7.5 90% C.L. allowed region for all three types of experiments is shown. Shaded region appears by considering the earth effect.

- Fig. 7.6 Expected energy spectra at Kamiokande are shown for the typical parameters in the allowed region of Fig. 7.5. Parameters ( $\delta m^2, \sin^2 2\theta$ ) = ( $10^{-5.2} \text{eV}^2, 10^{-2.2}$ ) for non-adiabatic solution and ( $10^{-5.4} \text{eV}^2, 10^{-0.2}$ ) for quasi-vacuum solution are used. Plots are observed energy spectra and solid histograms are the expected energy spectra. In this calculation, earth effect was also taken into account.
- Fig. 7.7 Density distribution in the earth [ref 7-2] used for the calculation of earth effect is shown.
- Fig. 7.8 90% C.L. allowed region in  $\delta m^2$ - $\sin^2 2\theta$  plane by Kamiokande result (without energy spectrum information) is shown. In this region vacuum oscillations play an important role.
- Fig. 7.9 90% C.L. allowed region by Kamiokande result considering energy spectrum information is shown.
- Fig. 7.10 90% C.L. allowed region by Chlorine experiment is shown for just-so oscillation solution.
- Fig. 7.11 90% C.L. allowed region by gallium experiments is shown. Small regions around  $(\delta m^2, \sin^2 2\theta) = (10^{-11.1} \text{eV}^2, 1)$  and  $(10^{-10.9} \text{eV}^2, 0.5)$  are not allowed in the figure.
- Fig. 7.12 Electron and neutron number density in the sun [ref 1-5] used for the calculation of neutrino propagation. Horizontal axis is radius as a ratio to the solar radius. Vertical axis is the density in units of mol/cm<sup>3</sup> ( $=6.022 \times 10^{23} / \text{cm}^3$ ).
- Fig. 7.13 Akhmedov type magnetic profile [ref 7-6] in the sun is shown. Parameters for magnetic strength in the convection zone  $B_0$  and that in radiation zone  $B_1$  are given by 20 kGauss and 1 MGauss.
- Fig. 7.14 Distribution of solar neutrino production points for each neutrino emission reaction are shown. These distributions are considered in the neutrino oscillation and resonant spin flavor precession calculations.
- Fig. 7.15 Neutrino propagation of Majorana neutrinos in the hybrid model is shown for several magnetic profile and parameter sets:  
 constant magnetic field ( $B, \delta m^2, \sin^2 2\theta$ ) = (20 kG,  $3 \times 10^{-7} \text{eV}^2, 0.1$ ), (20 kG,  $7 \times 10^{-8} \text{eV}^2, 0.3$ ),  
 Akhmedov type magnetic field ( $B_0, B_1, \delta m^2, \sin^2 2\theta$ ) = (20 kG, 20 kG,  $7 \times 10^{-8} \text{eV}^2, 0.3$ ),  
 without magnetic field ( $\delta m^2, \sin^2 2\theta$ ) = ( $7 \times 10^{-8} \text{eV}^2, 0.3$ ),  
 Akhmedov type magnetic field ( $B_0, B_1, \delta m^2, \sin^2 2\theta$ ) = (3 MG, 20 kG,  $10^{-5} \text{eV}^2, 0.2$ ), and (1 MG, 50 kG,  $4 \times 10^{-7} \text{eV}^2, 1$ ).

- Neutrino energy is 10 MeV, and transition magnetic moment is fixed at  $10^{-11} \mu_B$ .
- Fig. 7.16 90% C.L. allowed regions in  $\delta m^2$ - $\sin^2 2\theta$  plane by Chlorine experiment are shown for various configuration of magnetic field. Both neutrino oscillation and spin flavor precession (of Majorana neutrinos) are now taking place, but the time variation of the experiment is not considered yet. Magnetic profile in the sun is an Akhmedov type profile with  $B_1 = 1M, 3M, 300k, 100k, 0$  Gauss and  $B_0 = 1k, 2k, 5k, 10k, 20k, 25k, 30k, 35k, 40k, 45k, 50k, 60$  kGauss for each  $B_1$  value, flat magnetic field only in the convection zone ( $r/R_{\text{sun}} > 0.65$ ) with 12 types of  $B_0$  values, and flat magnetic field in the sun also with 12 types of  $B_0$  values. Transition magnetic moment of neutrinos is fixed at  $10^{-11} \mu_B$ . Horizontal and vertical axes are in units of  $\log(\sin^2 2\theta)$  and  $\log(\delta m^2 [\text{eV}^2])$ .
- Fig. 7.17 Same plot as Fig. 7.16 but allowed by gallium experiments.
- Fig. 7.18 Same plot as Fig. 7.16 but allowed by Kamiokande result considering energy spectrum information. View port in  $\delta m^2$ - $\sin^2 2\theta$  plane is now expanded.
- Fig. 7.19 Parameter sets of  $(\delta m^2, \sin^2 2\theta)$  where time variation of the solar neutrino flux in Chlorine experiment can be explained at 90% C.L. in  $\alpha$ - $\beta$  parameter space (data/SSM =  $\alpha N_{\text{ss}} + \beta$ ) are plotted. Magnetic field in the convection zone ( $B_0$ ) is ranging from 1 kG to 60 kGauss as a free parameter, and 7 types of magnetic profiles are characterized by magnetic field in the radiation zone ( $B_1 = 1M, 3M, 300k, 100k$  and 0 Gauss for Akhmedov type profile) and the shape of the magnetic field (Akhmedov type, flat only in the convection zone, or flat in the sun). Magnetic (transition) moment of neutrinos is fixed at  $10^{-11} \mu_B$ .
- Fig. 7.20 Same plot as Fig. 7.19 but both the time variation in Chlorine experiment and neutrino deficit in gallium experiments (data/SSM =  $0.55 \pm 0.11$  at the solar maximum period) can be explained.
- Fig. 7.21 Expected flux variation of Chlorine, Gallium and Kamioka (9.3, 7.5 and 7.0 MeV thresholds) experiments in terms of magnetic amplitude in the convection zone ( $B_0$ ) are shown. Parameter sets of  $(B_1, \delta m^2, \sin^2 2\theta)$  are chosen from typical values obtained in Fig. 7.20: (1 MG,  $10^{-6.85} \text{eV}^2, 10^{-2.2}$ ), (3 MG,  $10^{-6.85} \text{eV}^2, 10^{-2.6}$ ), (300 kG,  $10^{-8.45} \text{eV}^2, 1$ ), (flat in the convection zone,  $10^{-7.55} \text{eV}^2, 0.01$ ), (flat in the convection zone,  $10^{-8.05} \text{eV}^2, 1$ ) and (flat,  $10^{-7.45} \text{eV}^2, 10^{-2.4}$ ). Obtained  $B_{\text{min}}$  (amplitude at solar minimum,  $N_{\text{ss}} \sim 20$ ) and  $B_{\text{max}}$  (at solar maximum,  $N_{\text{ss}} \sim 150$ ) are also shown in the figure.

- Fig. 7.22 Same plot as Fig. 7.19 but the time variation in Chlorine and Kamiokande experiments are satisfied at 90% C.L.
- Fig. 7.23 Same plot as Fig. 7.21 but parameter sets are chosen from the typical values obtained in Fig. 7.22: (1 MG,  $10^{-6.95} \text{eV}^2, 0.1$ ), (3 MG,  $10^{-6.95} \text{eV}^2, 0.1$ ), (0 G,  $10^{-7.65} \text{eV}^2, 10^{-0.3}$ ), (flat in the convection zone,  $10^{-7.65} \text{eV}^2, 10^{-0.3}$ ), (flat in the convection zone,  $10^{-8.35} \text{eV}^2, 10^{-2.5}$ ), (flat,  $10^{-7.95} \text{eV}^2, 10^{-1.2}$ ).
- Fig. 7.24 Same plot as Fig. 7.19 but all experiments are satisfied. This is a hybrid solution of the solar neutrino problem, which can explain both the neutrino deficits and their time variations.
- Fig. 7.25 Same plot as Fig. 7.21 but parameter sets chosen from the typical values obtained in Fig. 7.24: (300 kG,  $10^{-8.65} \text{eV}^2, 1$ ) and (flat in the convection zone,  $10^{-7.95} \text{eV}^2, 10^{-2.3}$ ).
- Fig. 7.26 Hybrid solution obtained by H.Nunokawa [ref 1-32] is shown.
- Fig. 7.27 Neutrino propagation is traced from the center of the sun to the surface of the sun and moreover to the earth for a hybrid solution parameter set,  $(\delta m^2, \sin^2 2\theta) = (2.2 \times 10^{-9} \text{eV}^2, 1)$  with flat magnetic field (50 kG, 20 kG and 10 kG) in the convection zone. Large amounts of  $\bar{\nu}_e$  are produced via the processes of resonant spin flavor precession ( $\nu_e$  to  $\bar{\nu}_\mu$ ) and neutrino oscillation in vacuum ( $\bar{\nu}_\mu$  to  $\bar{\nu}_e$ ). Neutrino energies are set at 10 MeV, and transition moment of neutrino is fixed at  $10^{-11} \mu_B$ .
- Fig. 7.28 Expected rates of solar  $\bar{\nu}_e$  events in Kamiokande final sample above 13 MeV for various magnetic profiles are shown. Contour lines are drawn at 0.01, 0.02, 0.05, 0.1, 0.2, 0.5 and 1 events/day. Change of magnetic amplitude in the convection zone is reflected in  $\bar{\nu}_e$  event rate for the parameter region of  $\delta m^2 < 10^{-6} \text{eV}^2, \sin^2 2\theta > 0.01$ . Change of magnetic amplitude in the radiation zone influences the  $\bar{\nu}_e$  event rate for the parameter region of  $10^{-6} \text{eV}^2 < \delta m^2 < 10^{-4} \text{eV}^2, 10^{-1.5} < \sin^2 2\theta < 10^{-0.5}$ .
- Fig. 7.29 Neutrino propagation is traced from the center of the sun to the surface of the sun and moreover to the earth for a parameter set for which  $\bar{\nu}_e$  event rate is influenced by the magnetic amplitude in the radiation zone,  $(\delta m^2, \sin^2 2\theta) = (10^{-5.8} \text{eV}^2, 10^{-0.7})$  with Akhmedov type magnetic profile (3 MG, 1 MG and 300 kG) in the radiation zone. Magnetic strength in the convection zone was set at 0G. Neutrino energies are set at 10 MeV, and transition moment of neutrino is fixed at  $10^{-11} \mu_B$ . In the figures only the probability to appear as  $\bar{\nu}_e$  is scaled by a factor of 10.
- Fig. 7.30 Expected energy spectrum of  $\bar{\nu}_e$  events is compared with the observed energy spectrum in final sample (Kam-2 gain $\times 2, \cos \theta_{\text{sun}} < 0.8$ ).

## Table and Figure Captions

- Fig. 7.31 Excluded regions of Hybrid parameters for Majorana neutrinos from  $\bar{\nu}_e$  flux limit in Kamiokande are shown. Various magnetic profiles are tested, but the excluded region of  $\delta m^2 < 10^{-6} \text{eV}^2$ ,  $\sin^2 2\theta > 0.01$  is not influenced by the shape of the magnetic field, and is relevant to both of the two flavor hybrid models using Majorana neutrinos. Obtained excluded region covers almost entire hybrid solution suggested in [ref 1-32].
- Fig. A.1 Schematic of 20-inch PMT is shown.
- Fig. A.2 Quantum efficiency of 20-inch PMT is shown together with the Cherenkov spectrum after traversing 15 m of pure water.
- Fig. A.3 Pulse height distortion in terms of photon conversion point (anode uniformity) is shown.
- Fig. A.4 Pulse height distortion in terms of magnetic field is shown.
- Fig. A.5 Current network around the detector to compensate for the geomagnetic magnetic field is schematically shown.
- Fig. A.6 Magnetic shield for 20-inch PMT is shown.
- Fig. A.7 Water-proof structure of 20-inch PMT is shown.
- Fig. A.8 Holders and support frames for 20-inch PMT is shown.
- Fig. B.1 On-line data flow of Kamiokande-2 is schematically shown.
- Fig. C.1 Ni converter for the absolute energy calibration using  $\text{Ni}(n,\gamma)\text{Ni}'$  is schematically drawn. Fission neutron from  $^{252}\text{Cf}$  is moderated by water in the converter and captured by Ni atoms, then  $\gamma$ -ray emissions arise.
- Fig. C.2 A transition scheme of  $^{58}\text{Ni}(n,\gamma)^{59}\text{Ni}$  is shown. Energies of the  $\gamma$ -rays are given at the top and bottom of the level diagram. Relative intensities of the  $\gamma$ -rays are denoted beside the transition arrows in percentage.
- Fig. C.3 Ni+Cf calibration spectrum is shown as a function of number of hit PMTs which is one of energy scales.
- Fig. C.4 Background spectrum of Ni+Cf calibration measured by Cf source with polyethylene container is shown as a function of number of hit PMTs.
- Fig. C.5  $\text{Ni}(n,\gamma)\text{Ni}'$  spectrum obtained by a subtraction of background contribution (Fig. C.4) from Ni+Cf calibration spectrum (Fig. C.3) is shown. Best fit of Monte Carlo spectrum is super-imposed. The width of the distribution is well reproduced by the Monte Carlo spectrum whereas only the peak value is adjusted.
- Fig. C.6 Relative  $\text{Ni}(n,\gamma)\text{Ni}'$  energy is shown. The spread of the energy is the ambiguity of the energy measurement in Kamiokande. The spread is inside a  $\pm 2.3\%$  region from the central value throughout the full observation time of Kam-2 and Kam-3.

## Table and Figure Captions

- Fig. C.7 Schematic of laser calibration system is drawn. Light emission of  $\text{N}_2$ -laser is fitted to Cherenkov spectrum by dye. Half of the light is sent to photo-diode to trigger, and rest is sent to MgO diffusing ball through a combination of seven pieces of light attenuator and a 70m length of quartz fiber.
- Fig. C.8 Typical measurement of laser calibration is shown with a two dimensional scatter plot of charge and timing values (called a TQ-map). One plot represents one light pulse.
- Fig. C.9 Typical two dimensional plot of  $\ln(L \times Q / S(\theta))$  vs.  $L$  of a penetrating muon, where  $L$  is the distance from light emission point to hit PMT,  $Q$  the pulse height of the hit PMTs and  $S$  the effective surface area of the PMT cathode from the direction of  $\theta$ . The slope of the fitted line (dashes) is the inverse of the light attenuation length.
- Fig. C.10 Measured light attenuation length is plotted as a function of data taking time. The attenuation length is now stable around 60m.
- Fig. C.11 Light attenuation coefficient as a function of wave length used for the Monte Carlo simulation in Kam-3 is shown. Rayleigh scattering limit is also shown in the figure.
- Fig. C.12 Gain variation of PMTs as a function of time is shown by using photo-electrons / track-length of penetrating muons as a gain estimator. The sudden increase ( $\times 1.27$ ) of photo-electrons in December 1990 is due to light reflectors installed for Kam-3. The variation of the gain was stable within 10% throughout the full observation time.
- Table D.1 Detector performance of Super-Kamiokande is compared with that of present Kamiokande-3 detector.



Faint, illegible text on the left page, possibly bleed-through from the reverse side.

Faint, illegible text on the right page, possibly bleed-through from the reverse side.

# The p-p chain

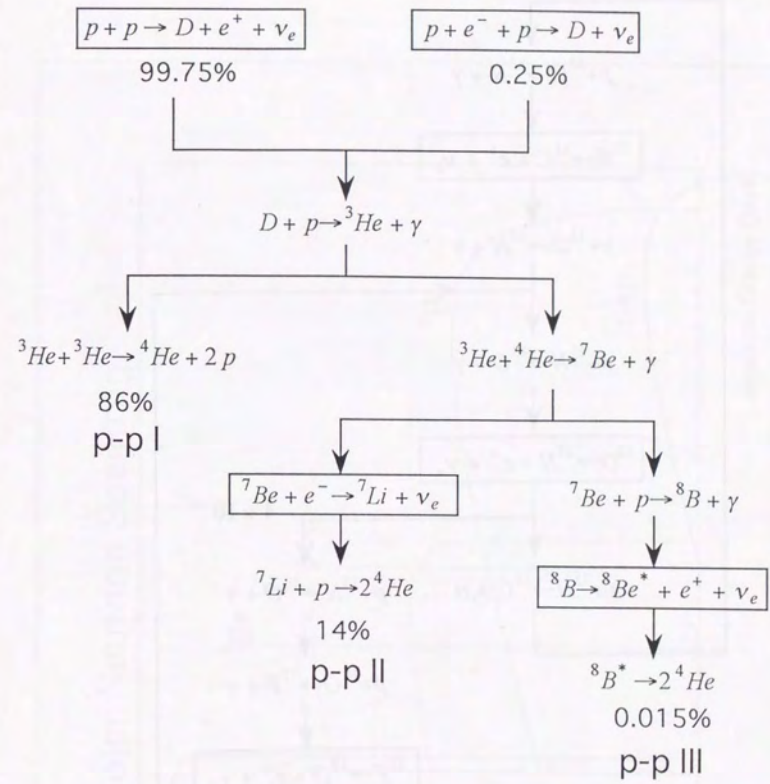


Fig. 1.1

## The CNO cycle

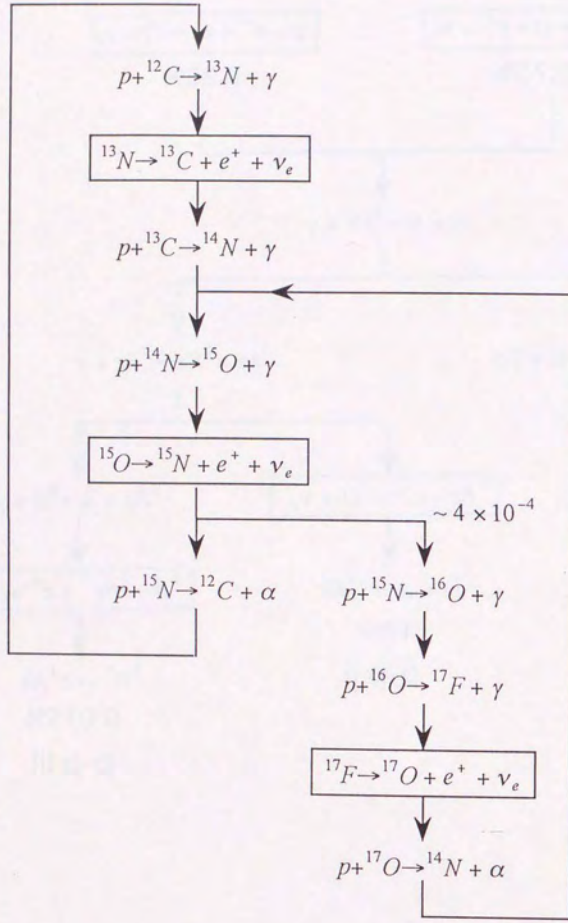


Fig. 1.2

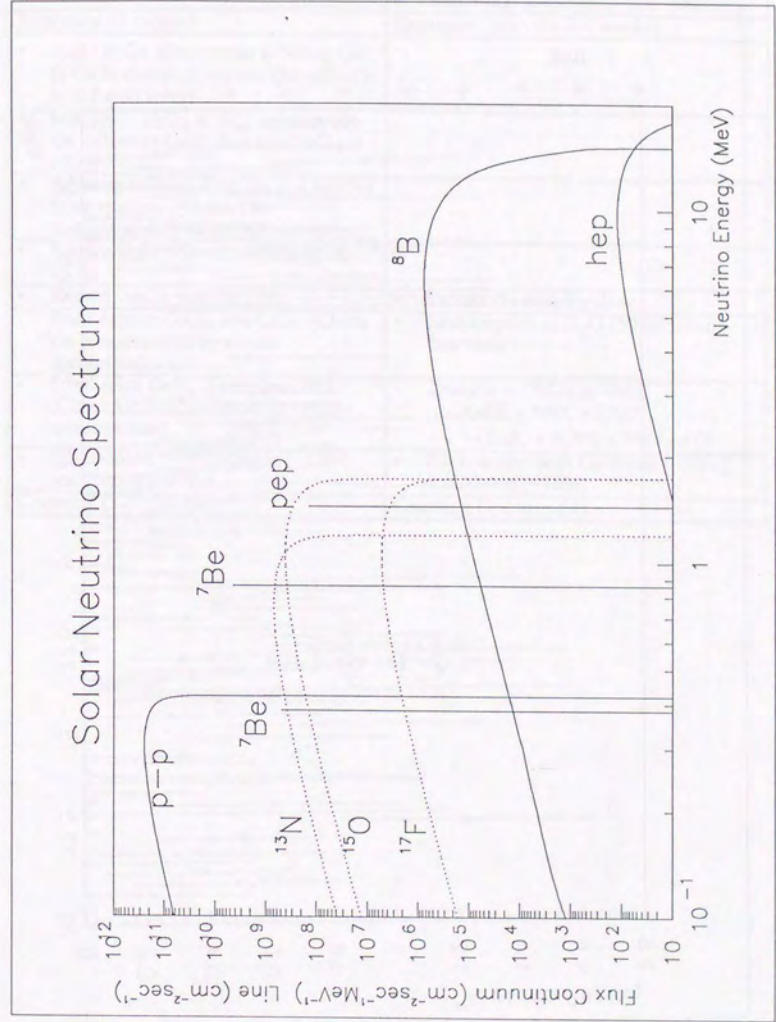


Fig. 1.3

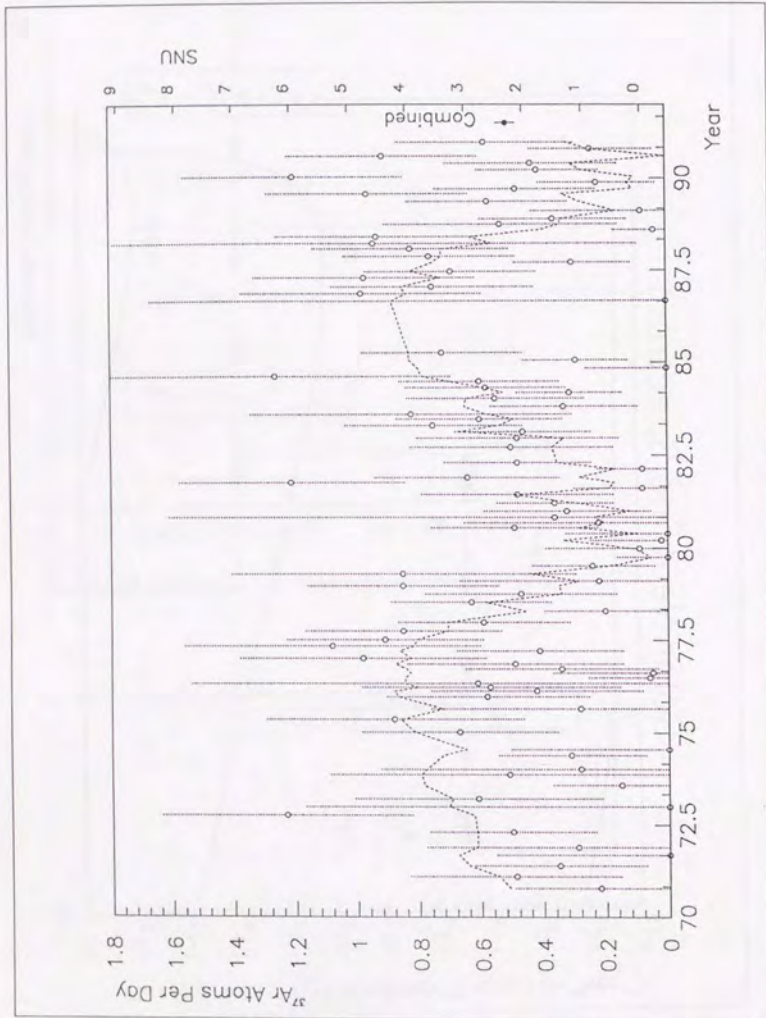


Fig. 1.4

### Gallium Extraction Chemistry & Procedures

SAGE (metal target)	GALLEX (aqueous solution)
	• Add 1 mg of carrier ( $^{70}\text{Ge}$ , $^{72}\text{Ge}$ ...)
Exposure (1 month)	Exposure (wait for 3-4 weeks)
• Add Ge-Ga alloy carrier (~500 $\mu\text{g}$ Ge) to Ga in chemical reactors (Metallic Ga is in liquid form)	-
• Mix $\text{H}_2\text{O}$ , $\text{H}_2\text{O}_2$ & $\text{HCl}$ solution into Ga (Oxidize Ge & dissolve $\text{GeCl}_4$ in $\text{HCl}$ )	-
• Separate solution from Ga and remove from reactors (Check Ge concentration with atomic absorption)	-
• Reduce $\text{H}_2\text{O}$ volume and add 12 M $\text{HCl}$	-
• Extract $\text{GeCl}_4$ with Ar flow	• Extract Ge with $\text{N}_2$ flow
• Back extract $\text{GeCl}_4$ into $\text{CCl}_4$ (Check Ge concentration by atomic absorption)	• Reabsorption in $\text{H}_2\text{O}$ (50 ml tritium-free water)
• Synthesize $\text{GeH}_4$ (Germane Gas) (Check Ge concentration by volume measurement)	• Transform $\text{GeCl}_4$ in $\text{GeH}_4$ $\text{GeCl}_4 + \text{KBH}_4 + 3\text{H}_2\text{O}$ $\rightarrow \text{GeH}_4 + \text{H}_3\text{BO}_3 + 3\text{HCl} + \text{KCl}$
• Fill counters with Germane (~10%) and Xenon (~90%)	• Fill counters with Germane (~30%) and Xenon (~70%)
Counting (3-5 months)	Counting (> 6 months)

Fig. 1.5

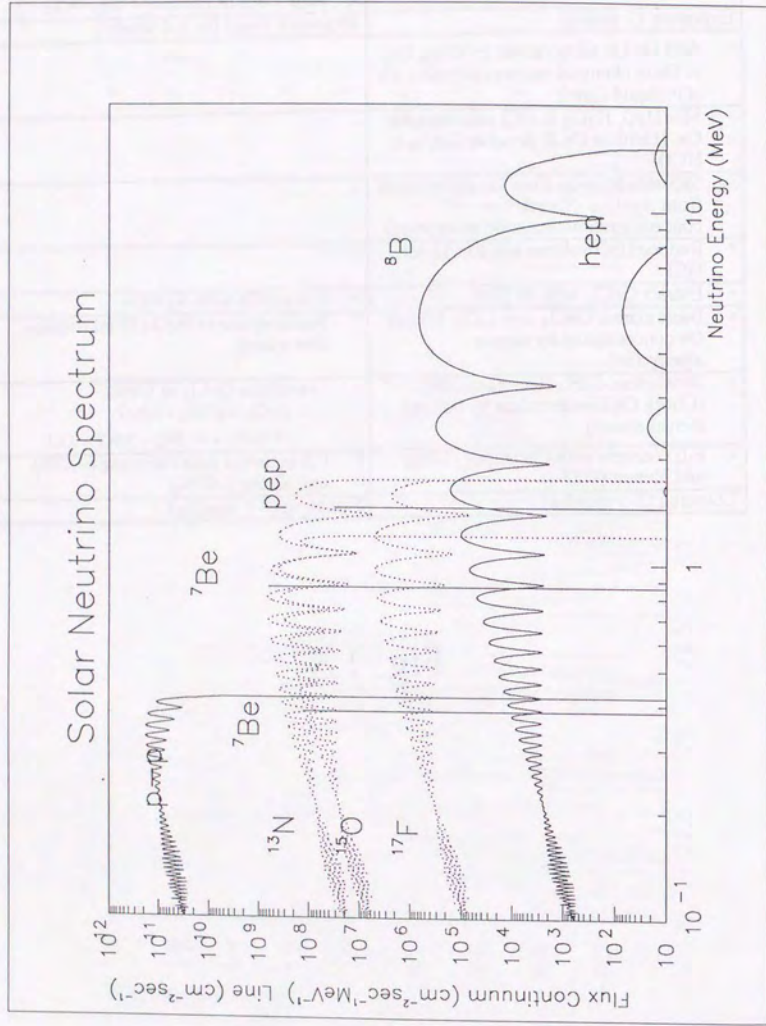


Fig. 3.1

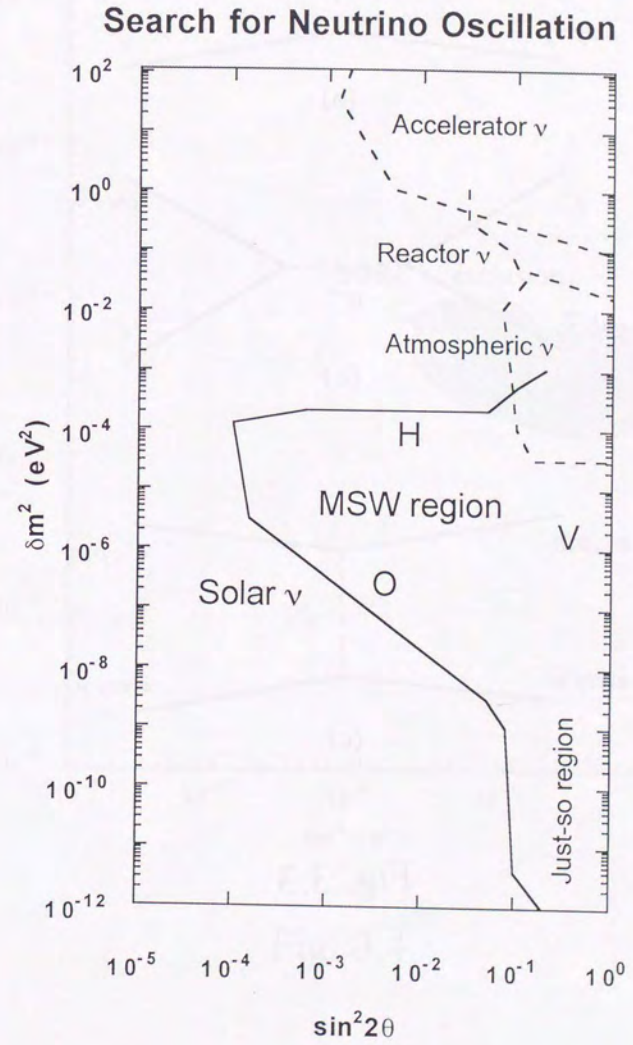


Fig. 3.2

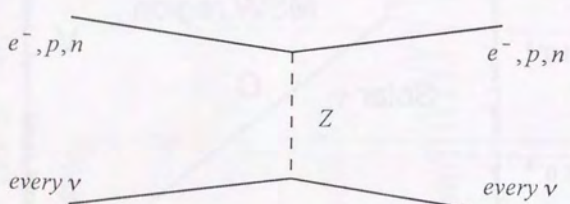
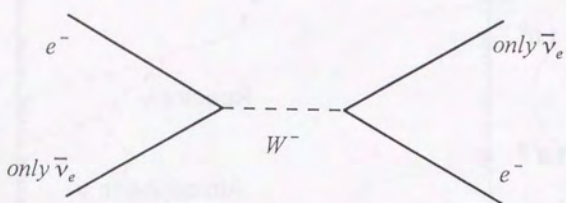
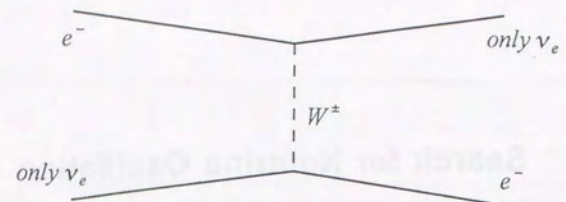


Fig. 3.3

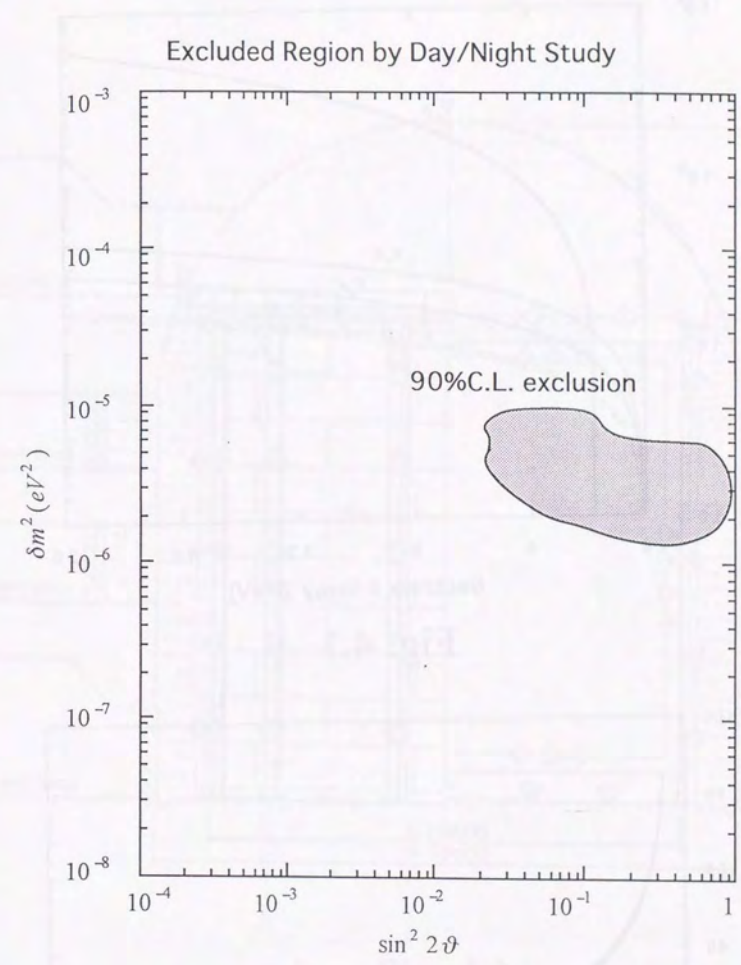


Fig. 3.4

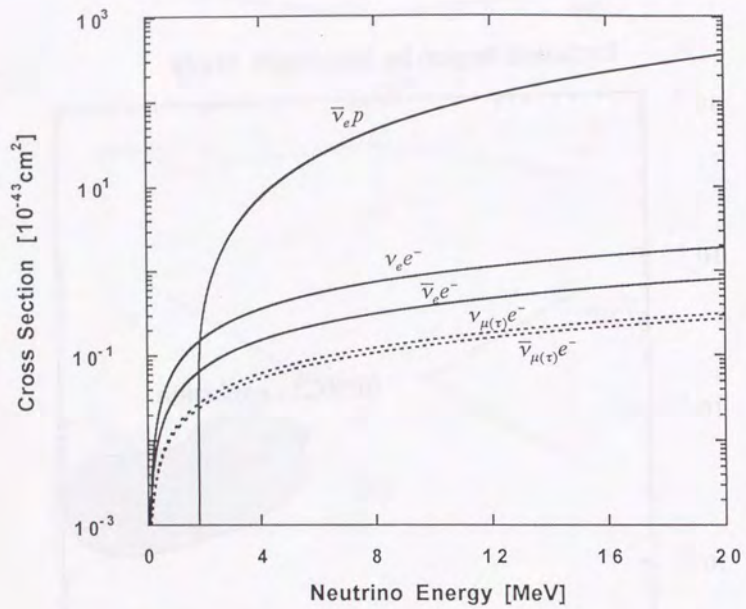


Fig. 4.1

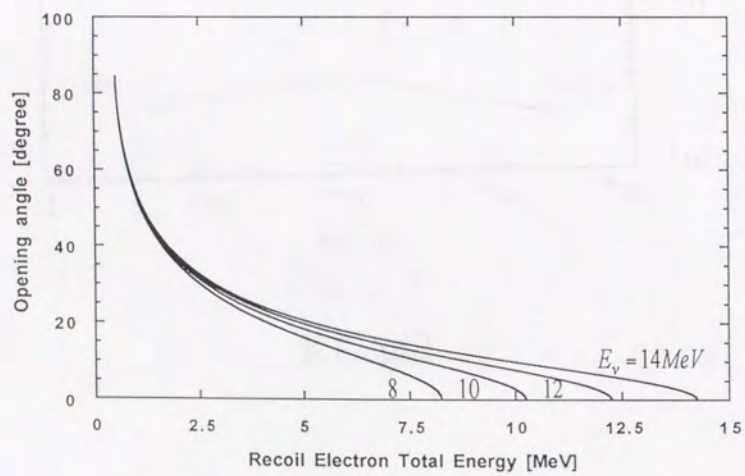


Fig. 4.2

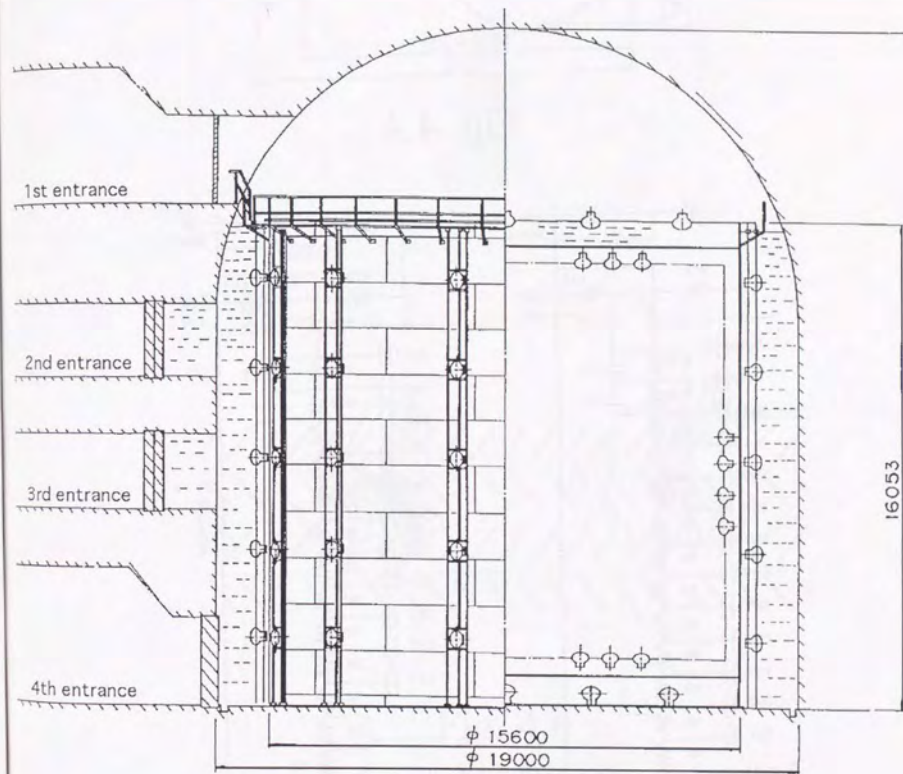


Fig. 4.3

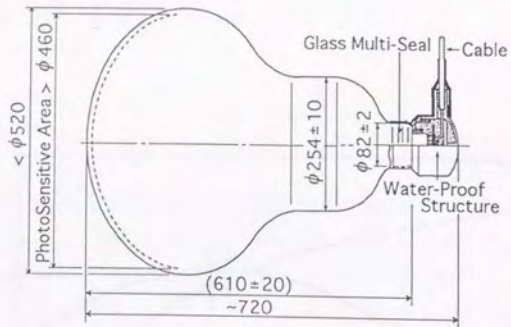
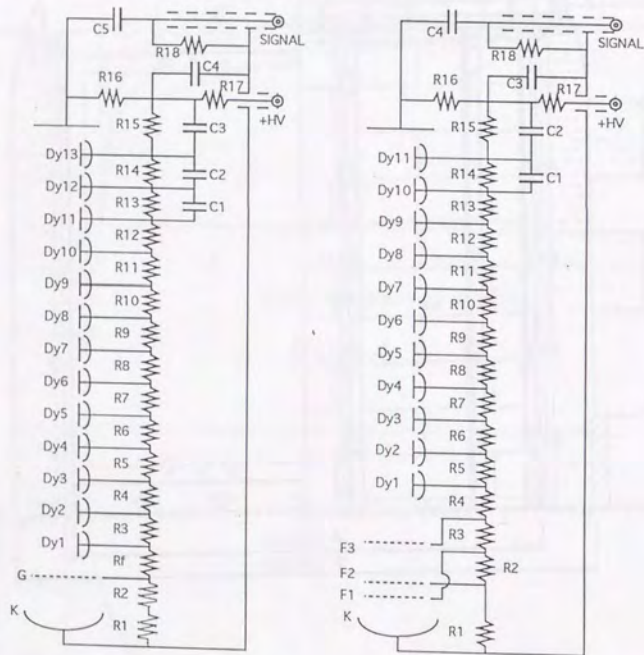


Fig. 4.4



R1, R2 : 1.1M  $\Omega$   
 R3-R15 : 274k  $\Omega$   
 R16 : 200k  $\Omega$   
 R17, R18 : 10k  $\Omega$   
 Rf : 15k  $\Omega$   
 C1-C3 : 0.01  $\mu F$   
 C4, C5 : 0.0047  $\mu F$

R1 : 1.3M  $\Omega$   
 R3 : 549k  $\Omega$   
 R4 : 5.49k  $\Omega$   
 R5 : 820k  $\Omega$   
 R2, R6-R15 : 274k  $\Omega$   
 R16 : 200k  $\Omega$   
 R17, R18 : 10k  $\Omega$   
 C1, C2 : 0.01  $\mu F$   
 C3, C4 : 0.0047  $\mu F$

Fig. 4.5

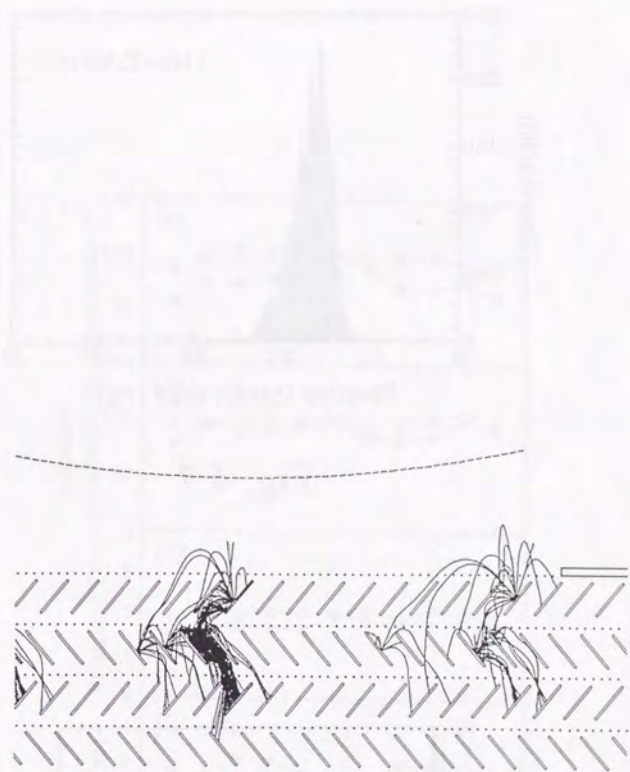


Fig. 4.6



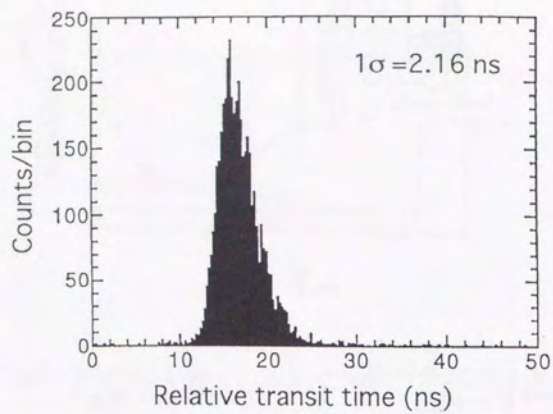


Fig. 4.7

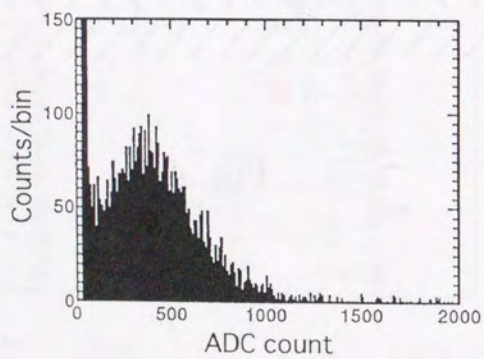


Fig. 4.8

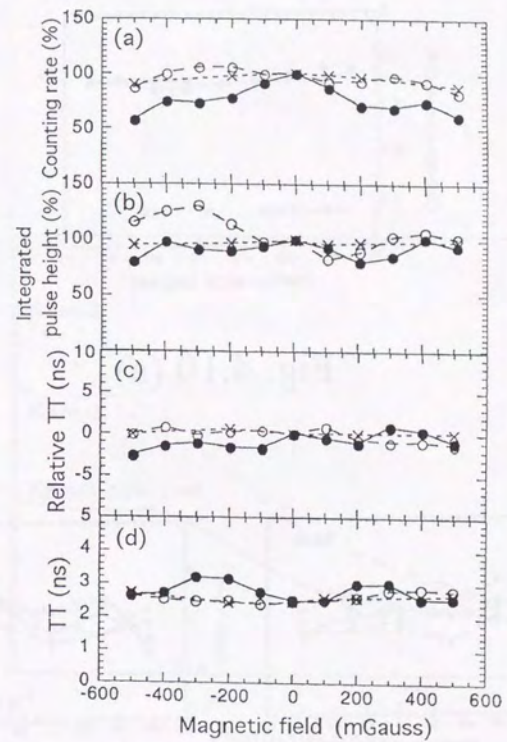


Fig. 4.9

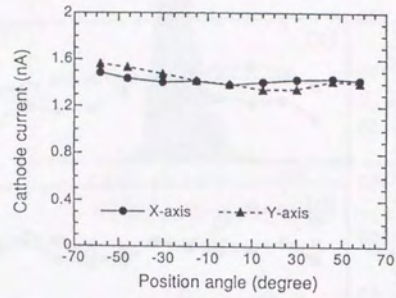


Fig. 4.10 (a)

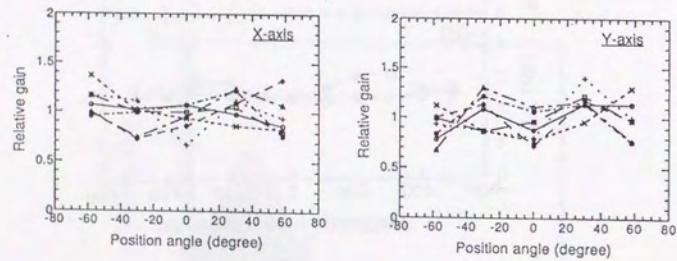


Fig. 4.10 (b)

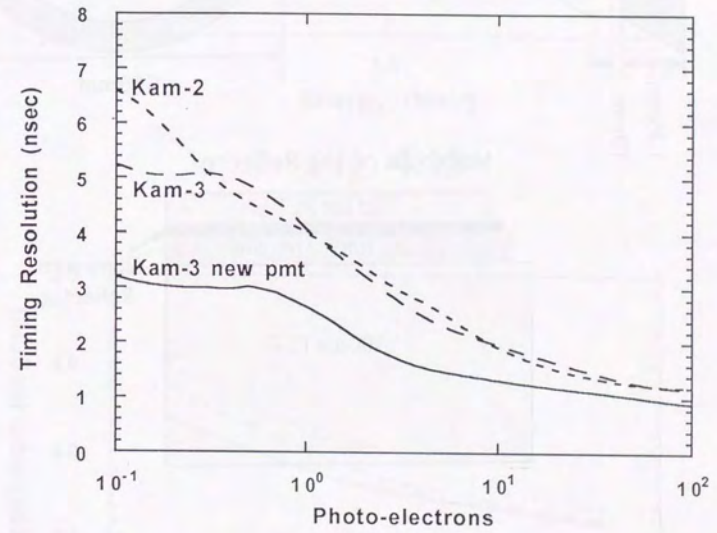


Fig. 4.11

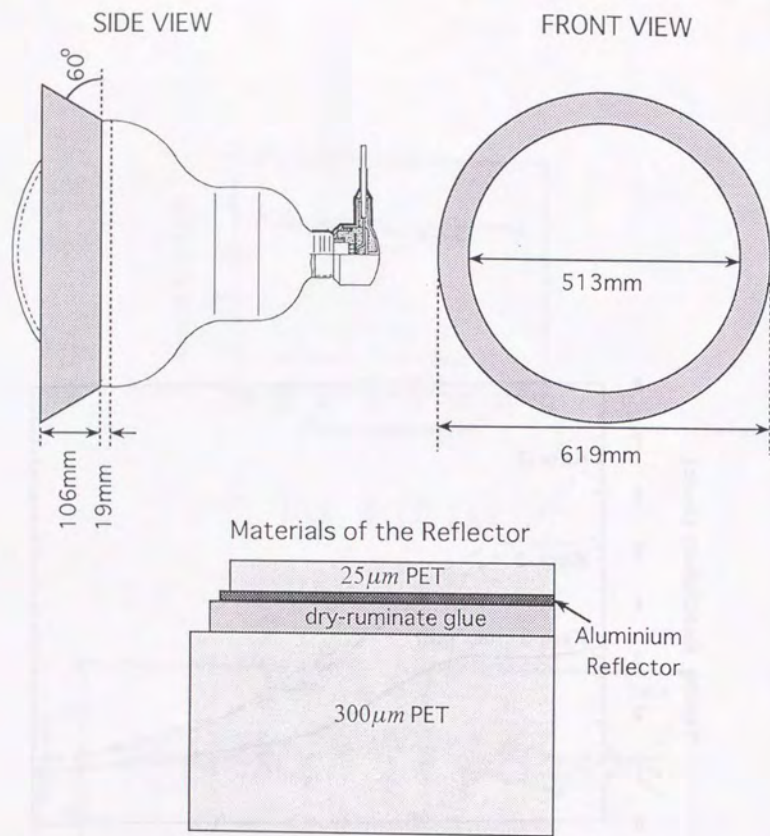


Fig. 4.12

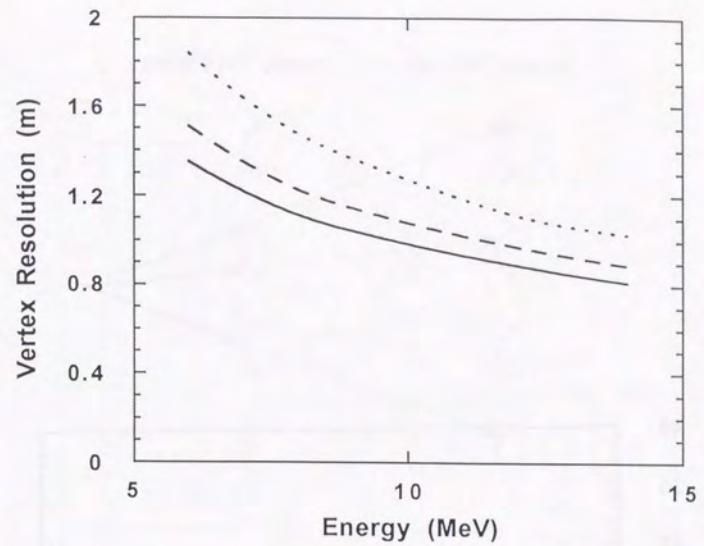


Fig. 4.13

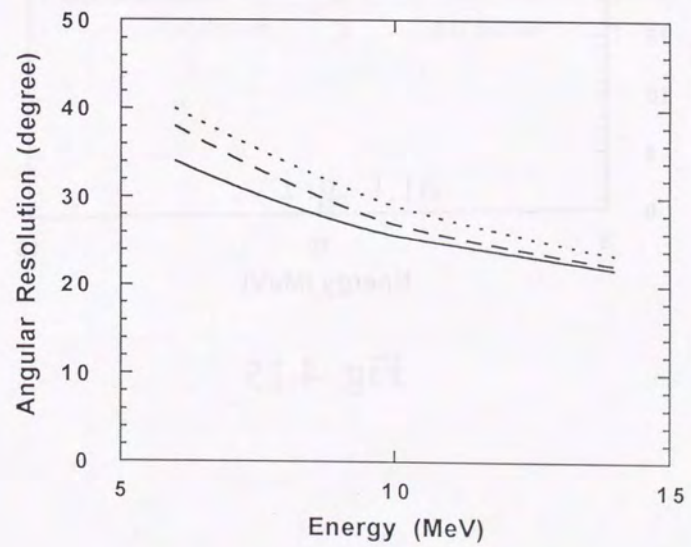


Fig. 4.14

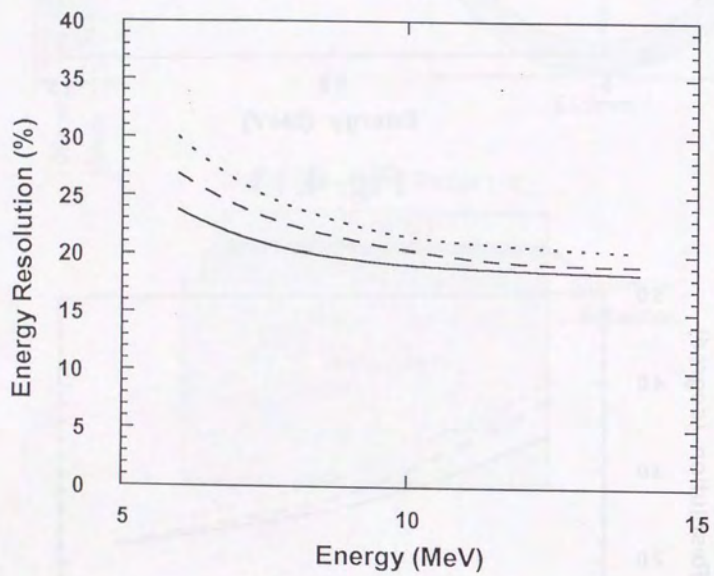
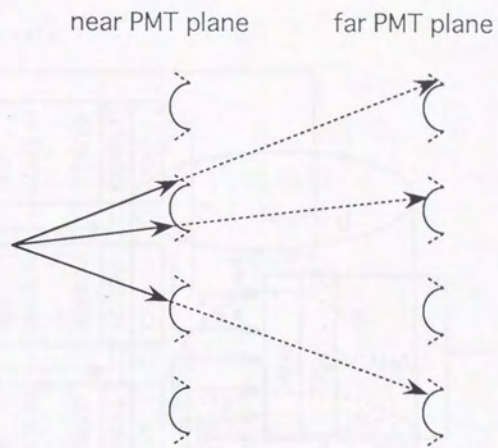


Fig. 4.15



Kam-2	# of hit PMTs	2	# of hit PMTs	2
	# of photons	2	# of photons	2
Kam-3	# of hit PMTs	2	# of hit PMTs	3
	# of photons	3	# of photons	3

Fig. 4.16

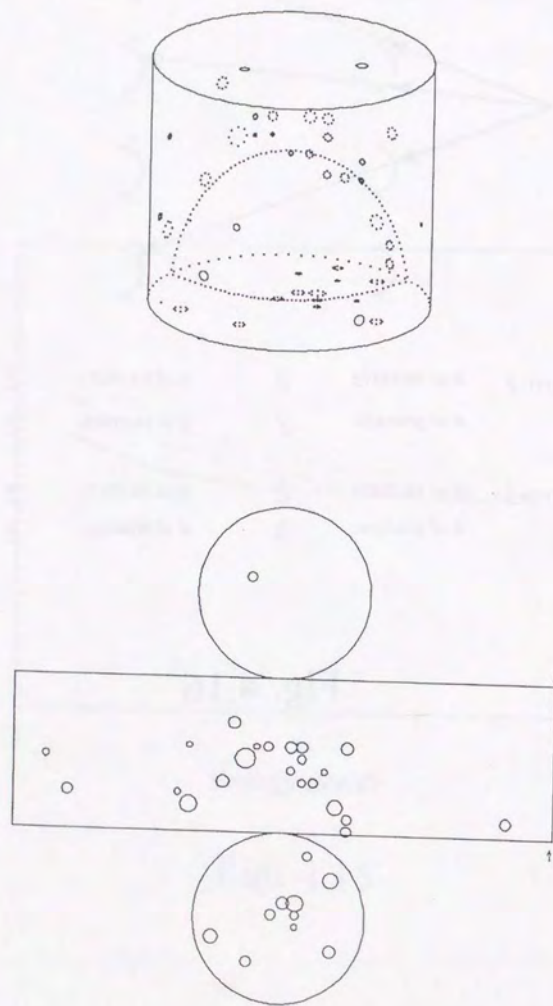


Fig. 4.17

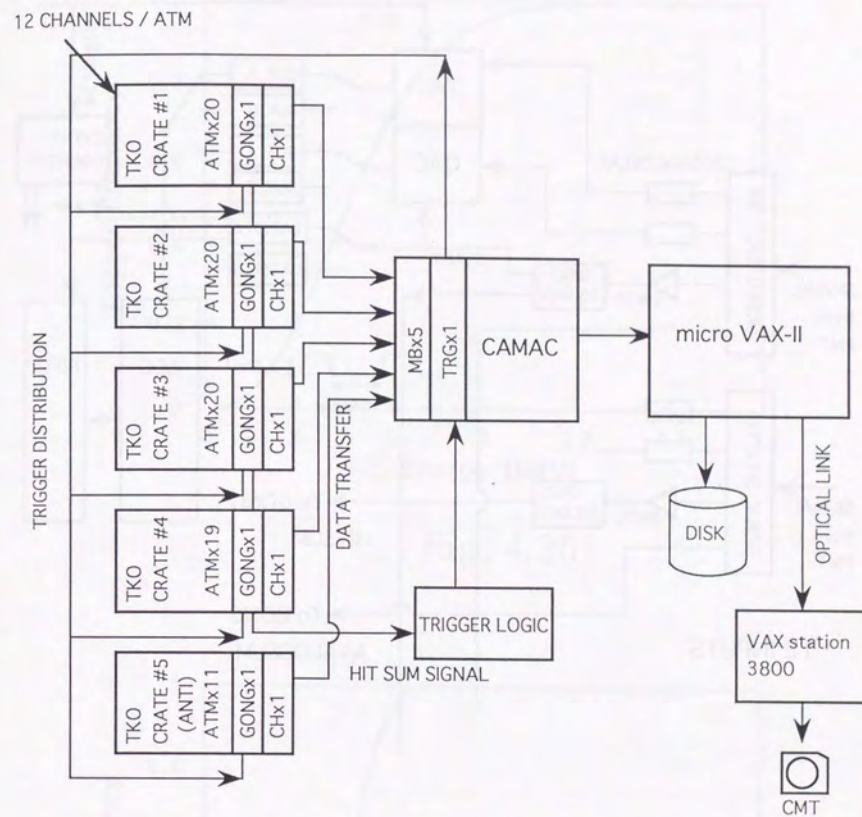


Fig. 4.18

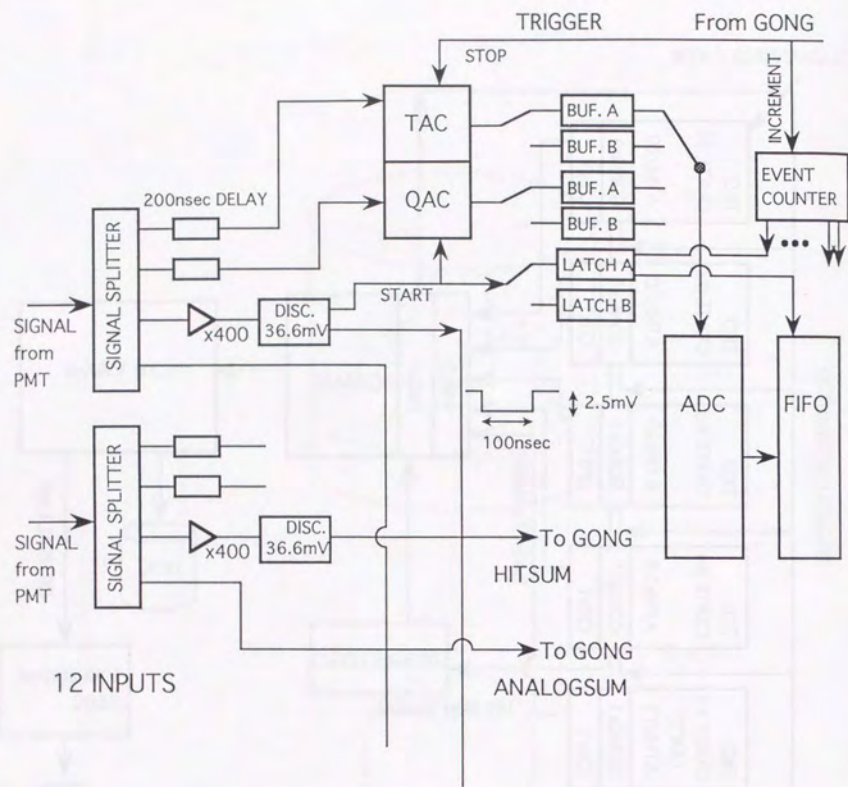


Fig. 4.19

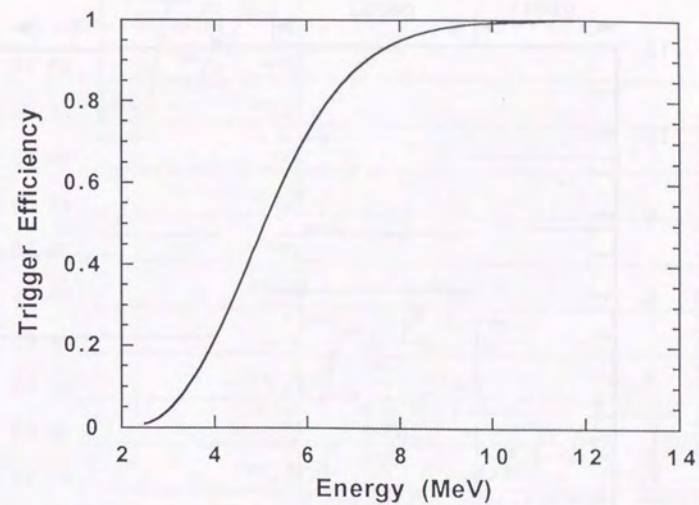


Fig. 4.20

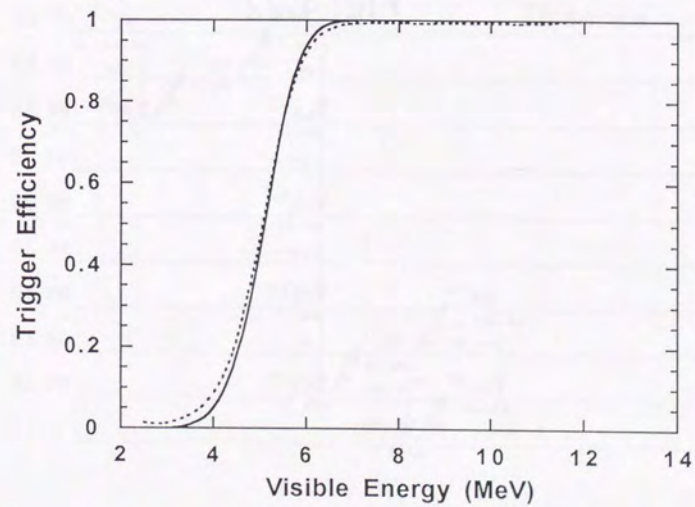


Fig. 4.21

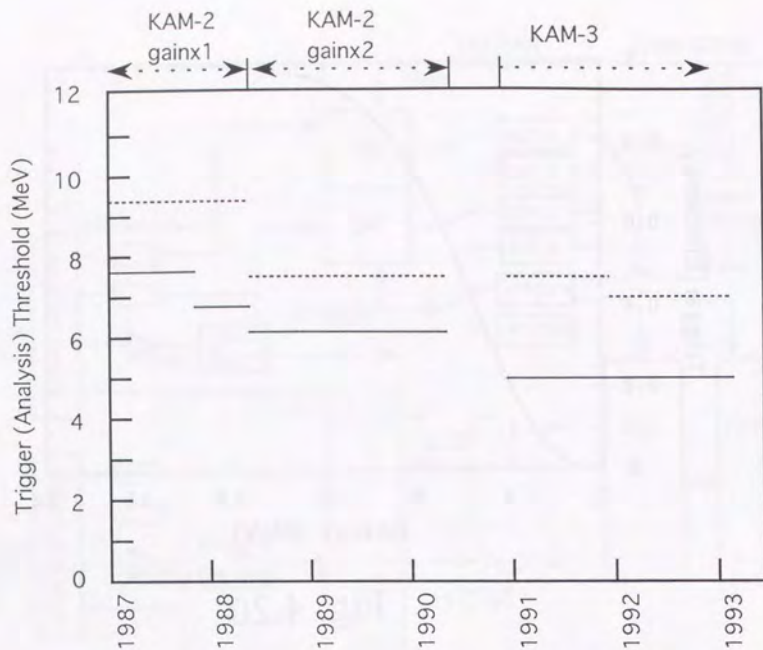


Fig. 4.22

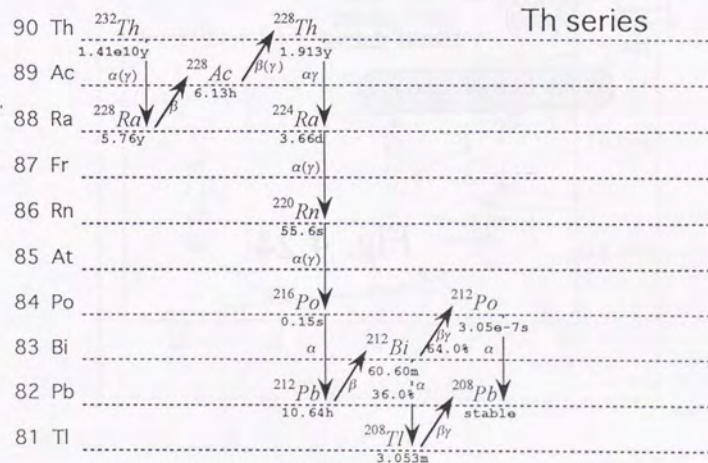
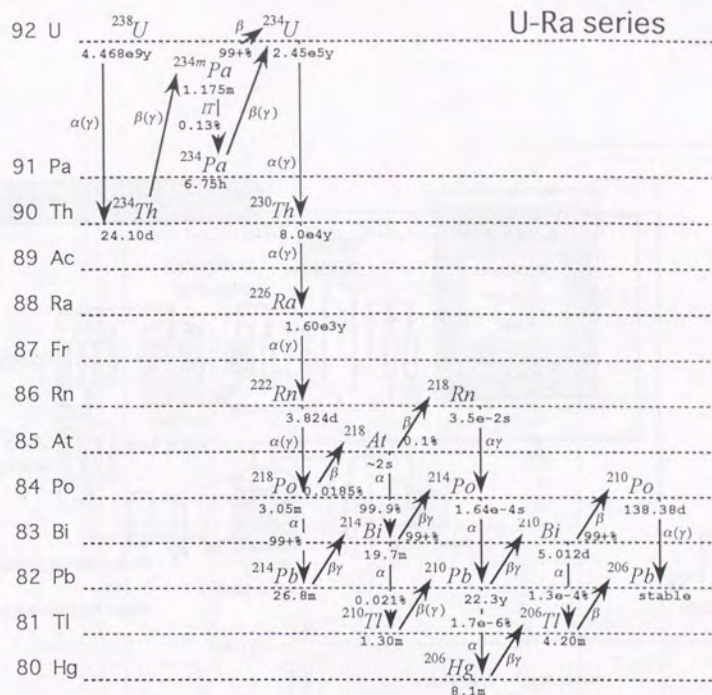


Fig. 4.23

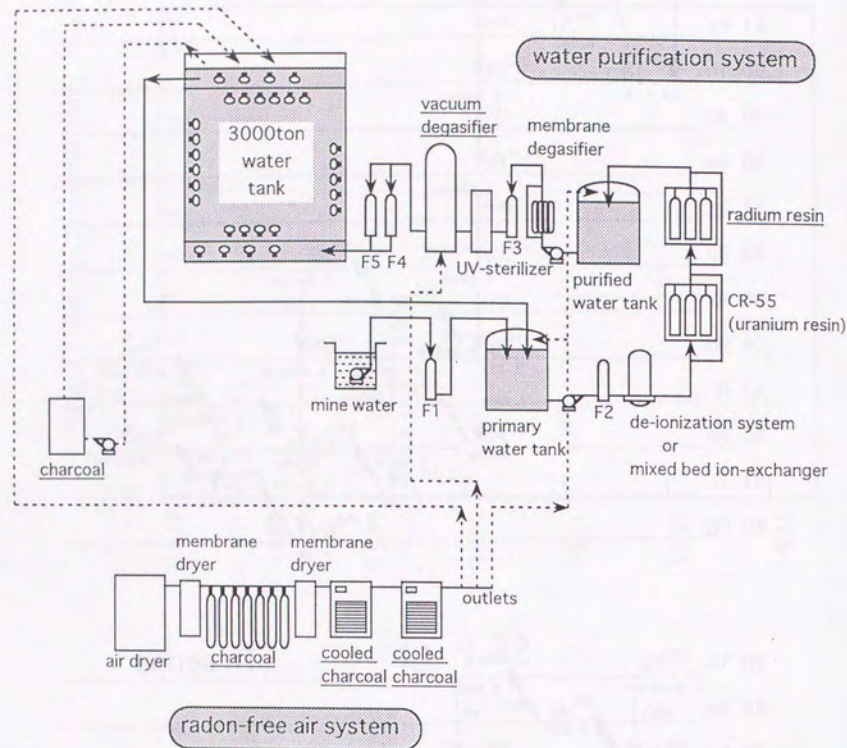


Fig. 4.24

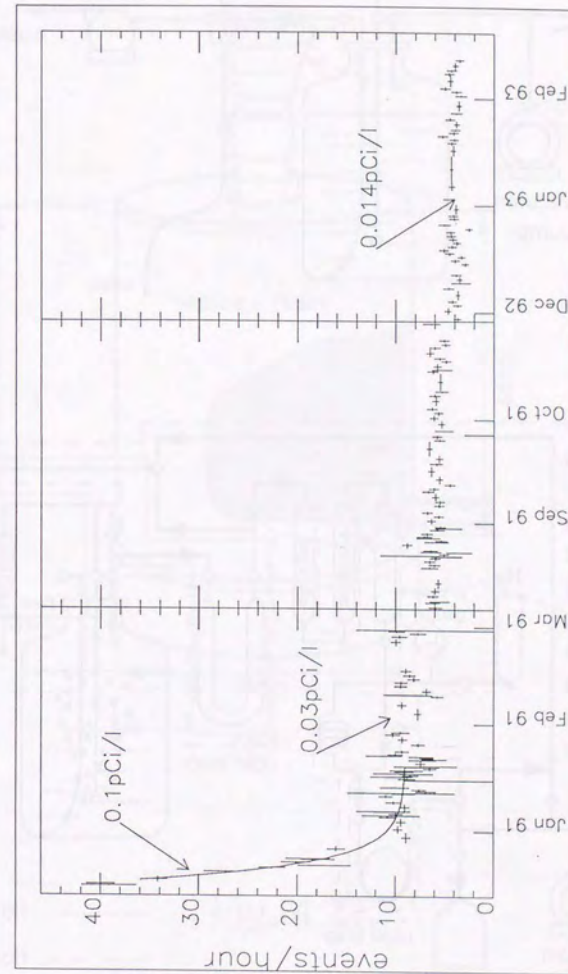


Fig. 4.25



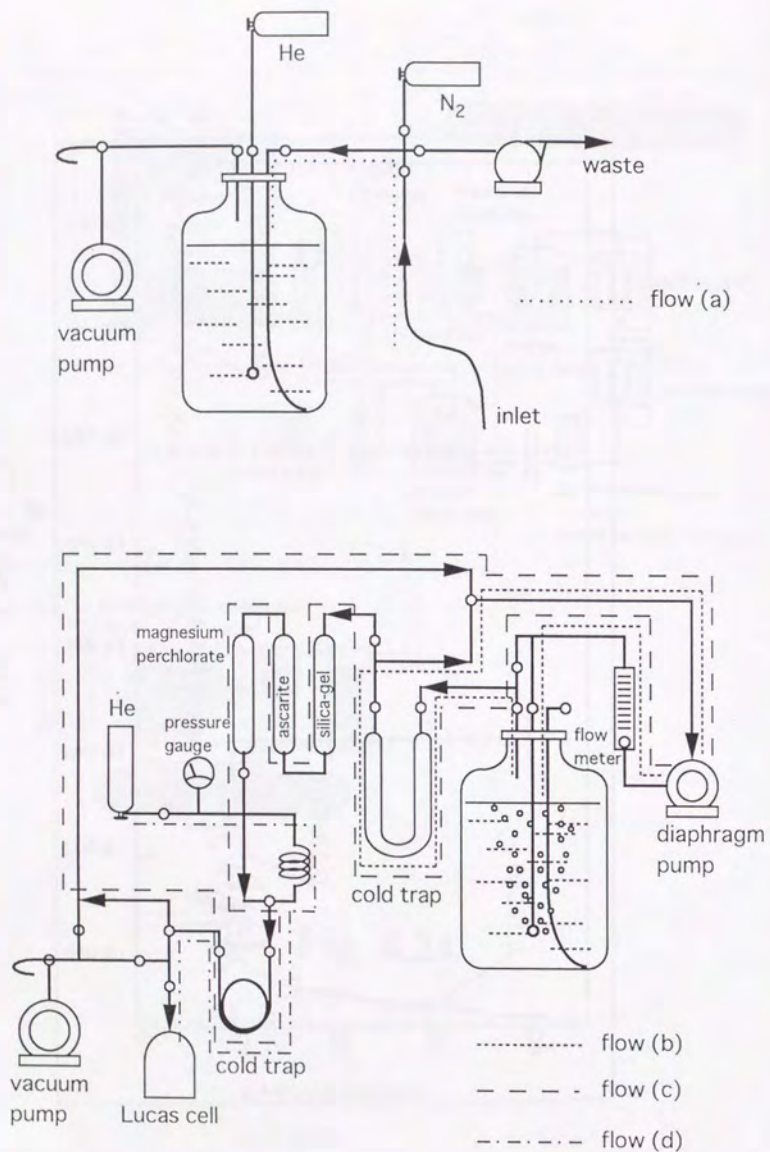


Fig. 4.26

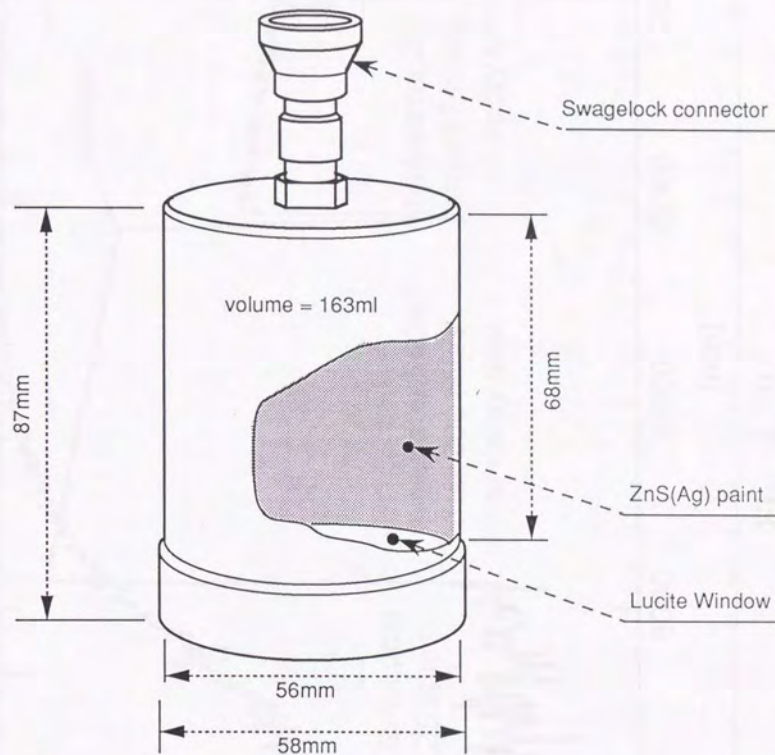


Fig. 4.27

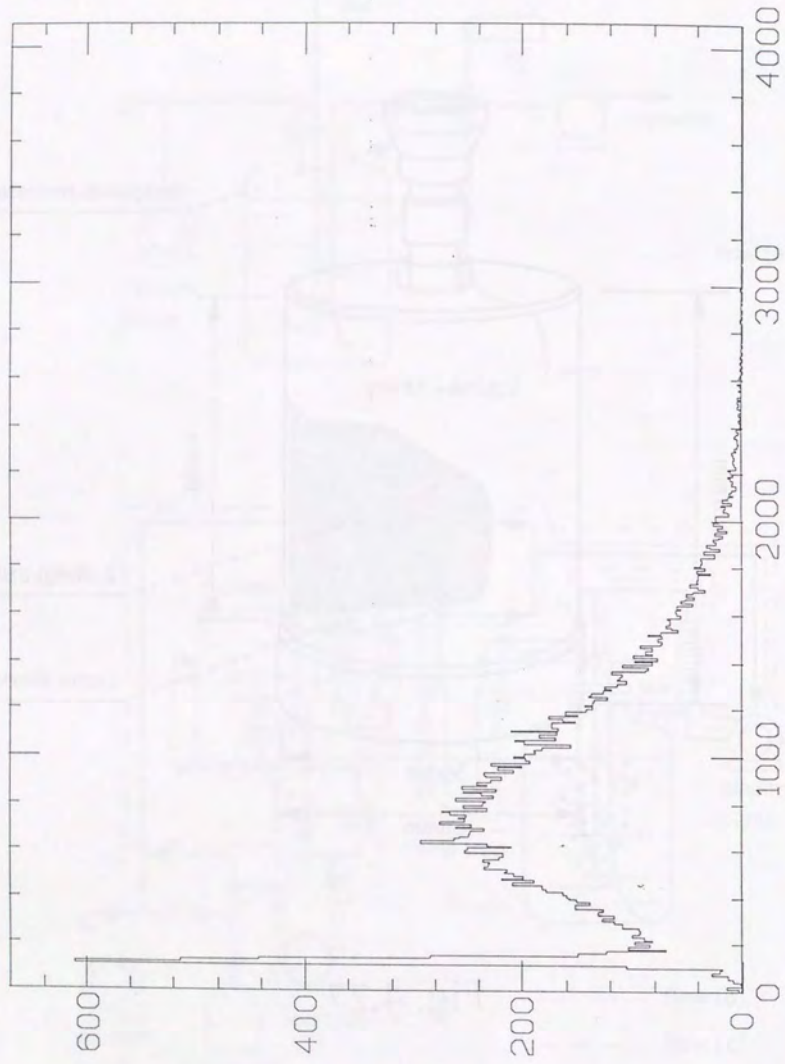


Fig. 4.28

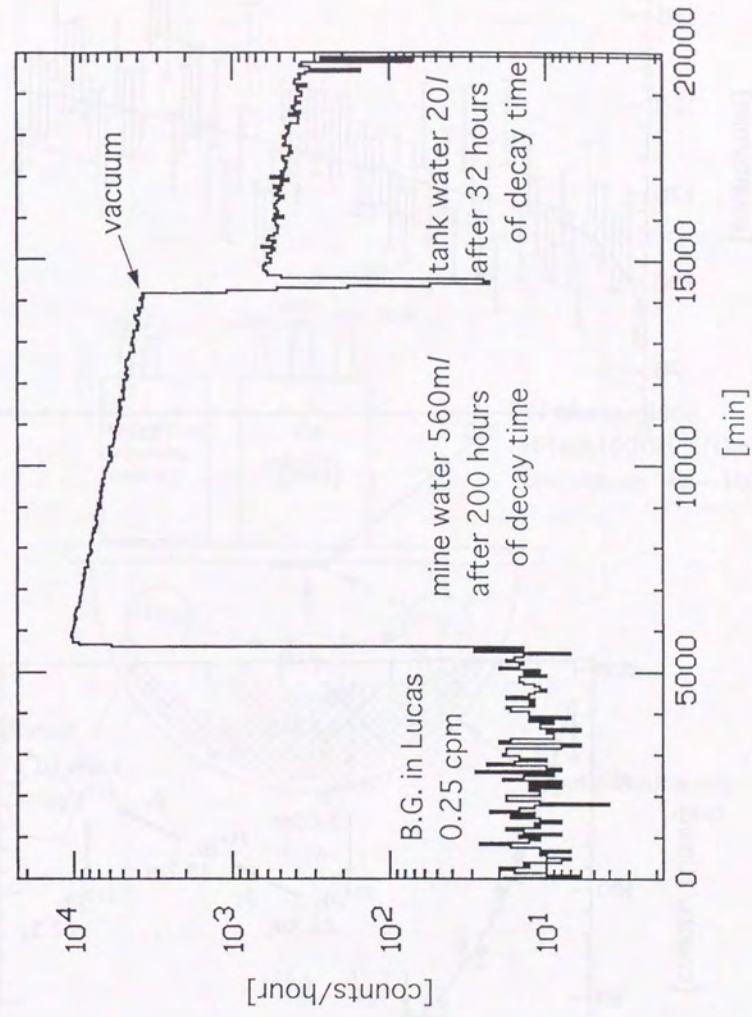


Fig. 4.29

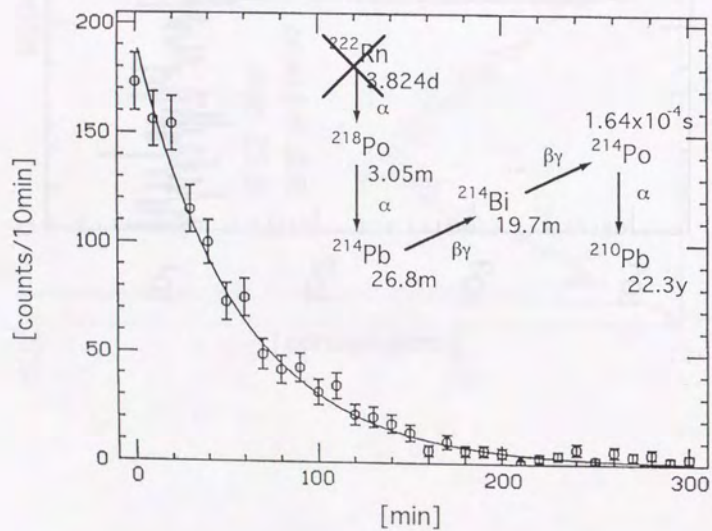
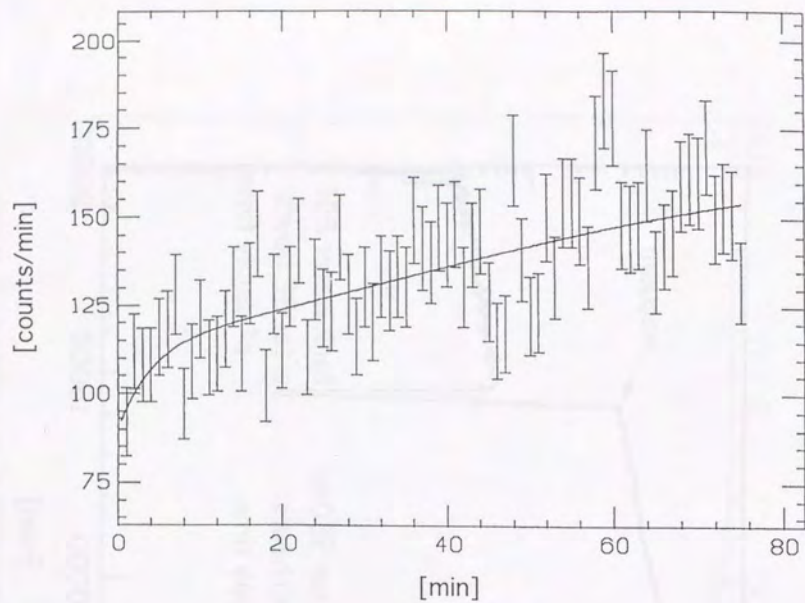


Fig. 4.30

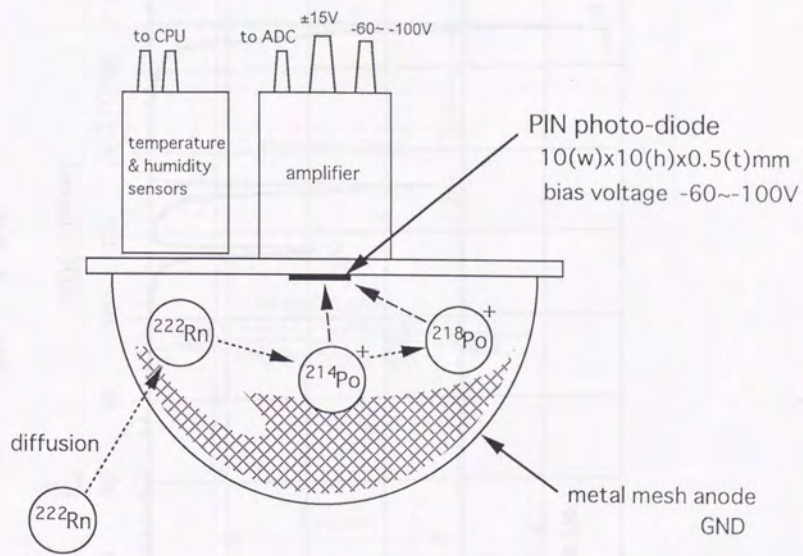


Fig. 4.31

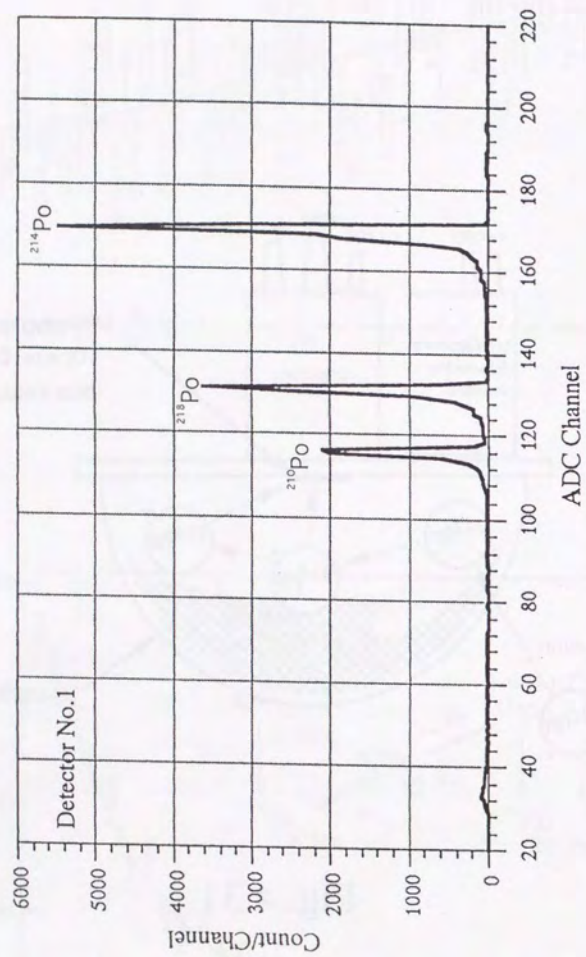


Fig. 4.32

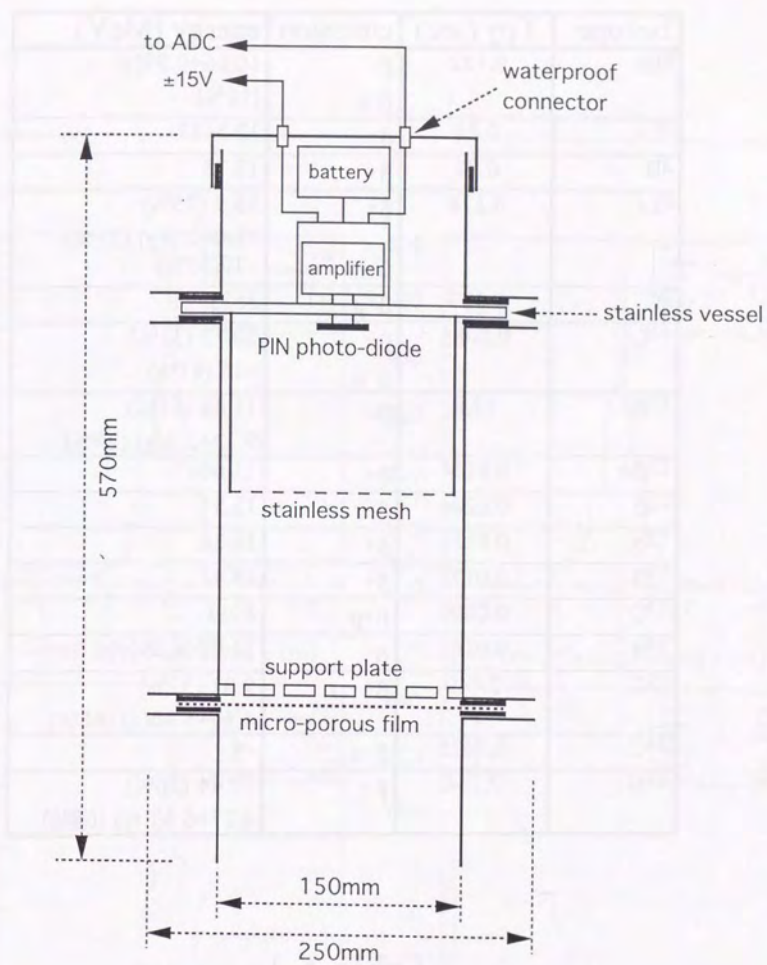


Fig. 4.33

Isotope	T <sub>1/2</sub> (sec)	emission	energy (MeV)
<sup>8</sup> He	0.122	β <sup>-</sup> β <sup>-</sup> n	10.66+0.99(γ) (11%)
<sup>8</sup> Li	0.84	β <sup>-</sup>	12.5-13
<sup>8</sup> B	0.77	β <sup>+</sup>	13.73
<sup>9</sup> Li	0.178	β <sup>-</sup> β <sup>-</sup> n	13.5 (75%) 11.0+2.5(γ) (25%) ~10(35%)
<sup>9</sup> C	0.127	β <sup>+</sup> p	3~13
<sup>11</sup> Li	0.0085	β <sup>-</sup> β <sup>-</sup> n	20.77 (31%) ~16 (61%)
<sup>11</sup> Be	13.8	β <sup>-</sup>	11.48 (61%) 9.32+2.1(γ) (29%)
<sup>12</sup> Be	0.0114	β <sup>-</sup>	11.66
<sup>12</sup> B	0.0204	β <sup>-</sup>	13.37
<sup>12</sup> N	0.0110	β <sup>+</sup>	16.38
<sup>13</sup> B	0.0173	β <sup>-</sup>	13.42
<sup>13</sup> O	0.0090	β <sup>+</sup> p	8~14
<sup>14</sup> B	0.0161	β <sup>-</sup>	14.07+6.09(γ)
<sup>15</sup> C	2.449	β <sup>-</sup>	9.82 (32%) 4.51+5.30(γ) (68%)
<sup>16</sup> C	0.7478	β <sup>-</sup> n	~4
<sup>16</sup> N	7.134	β <sup>-</sup>	10.44 (26%) 4.27+6.13 (γ) (68%)

Table 5.1

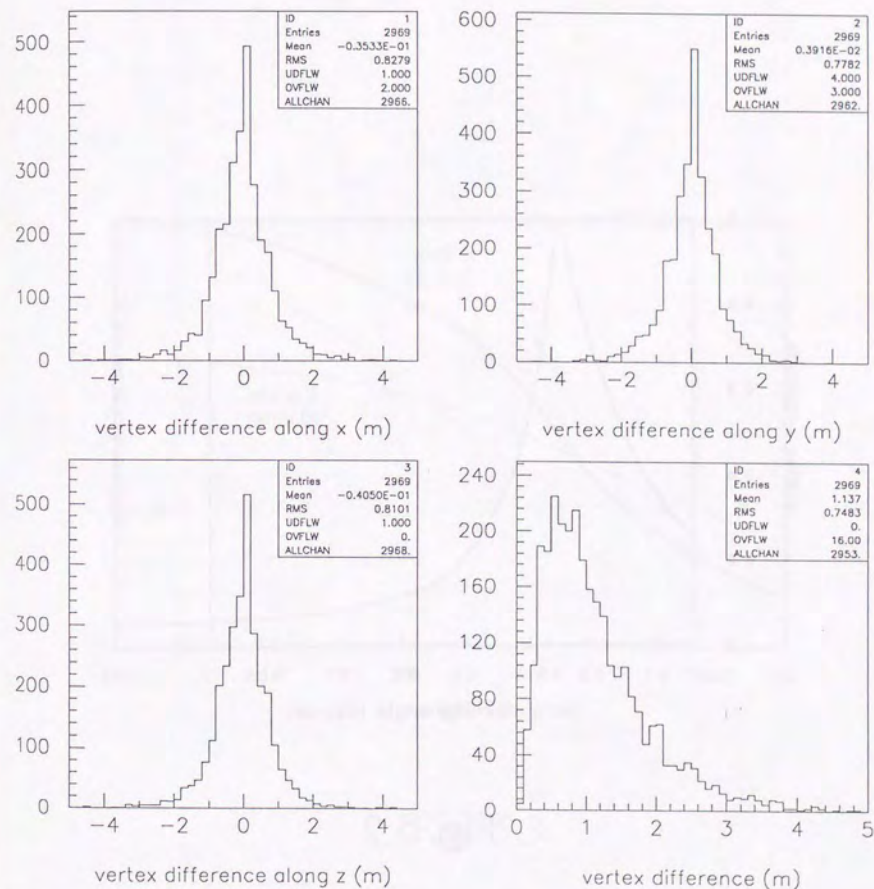


Fig. 5.1

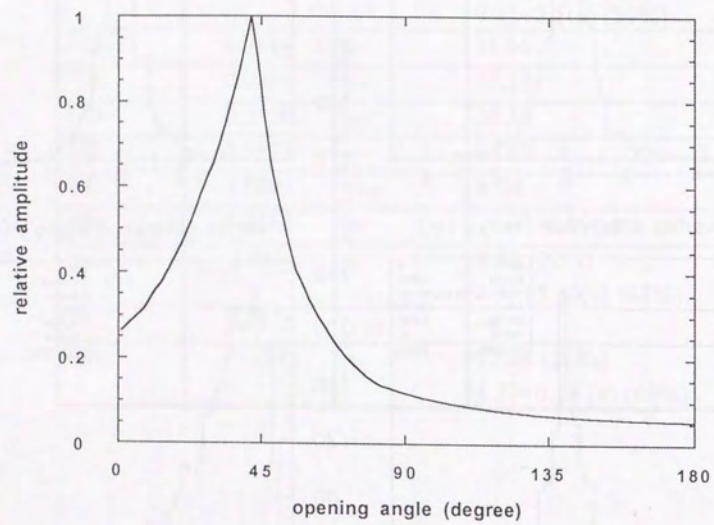


Fig. 5.2

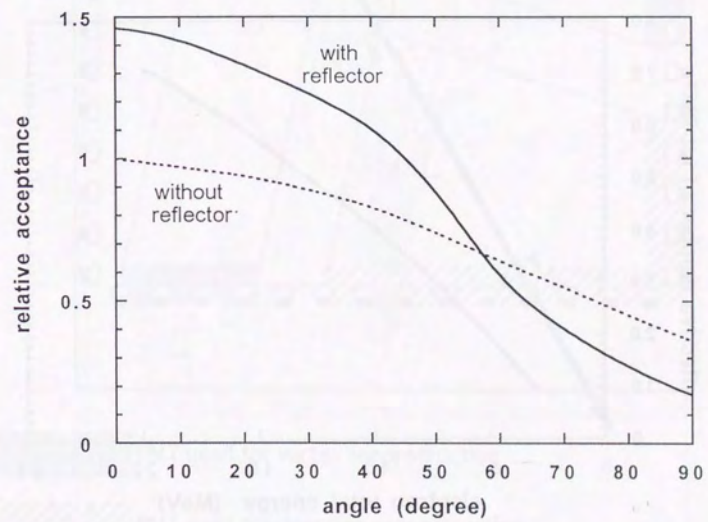


Fig. 5.3

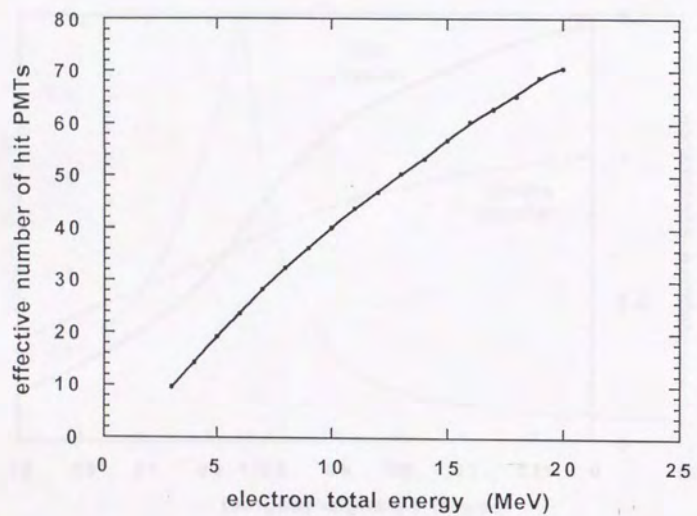


Fig. 5.4

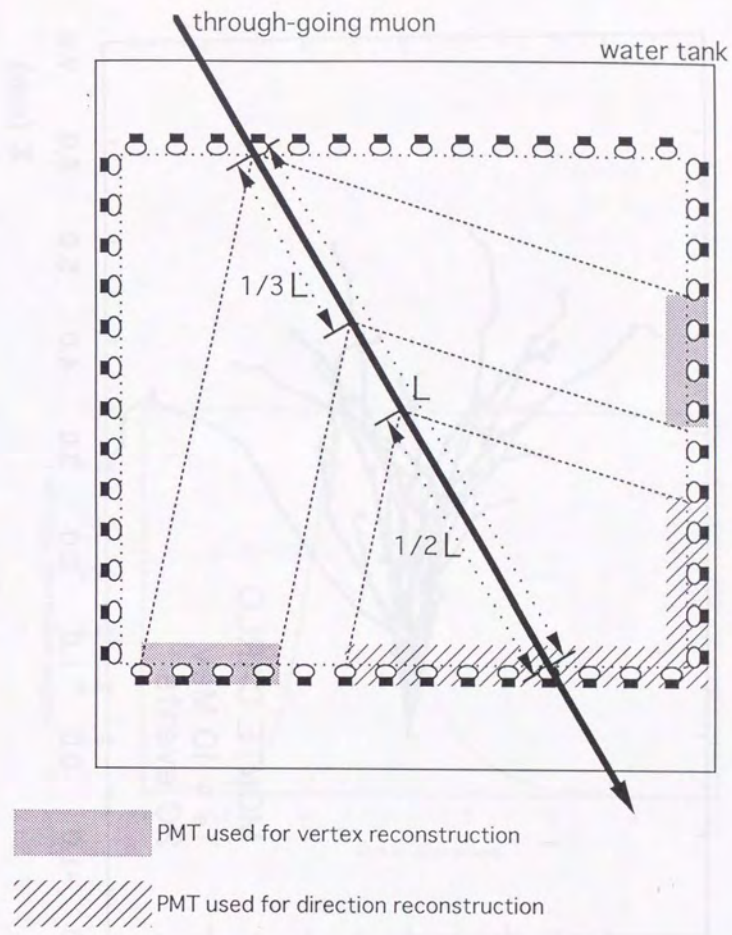


Fig. 5.5

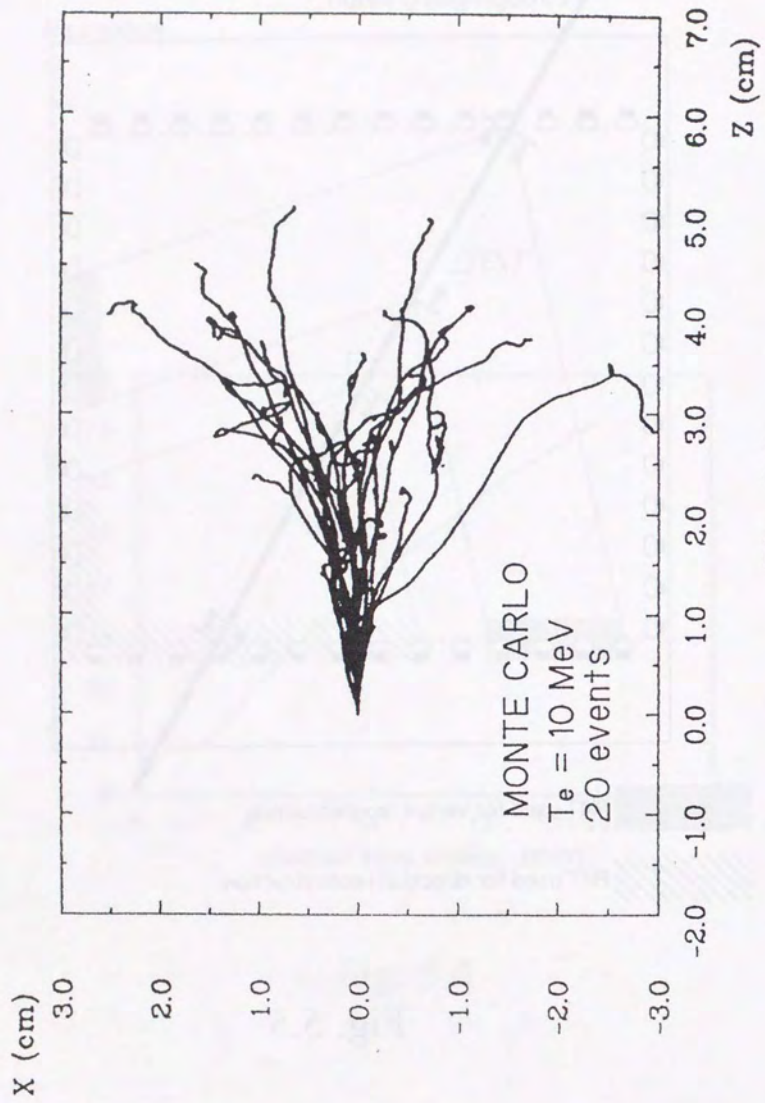


Fig. 5.6

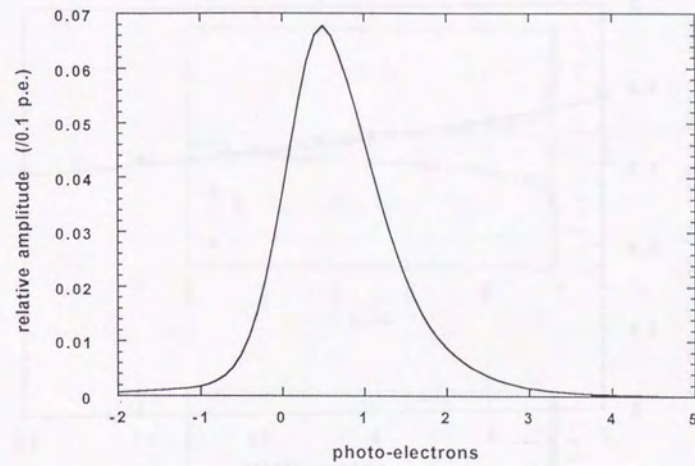


Fig. 5.7



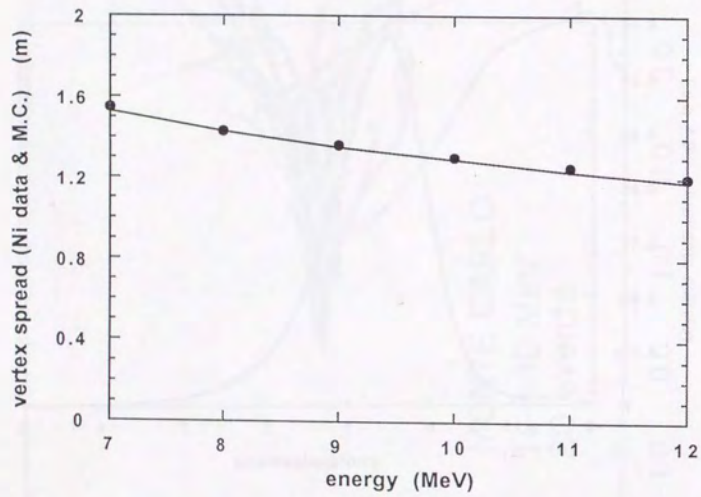


Fig. 5.8

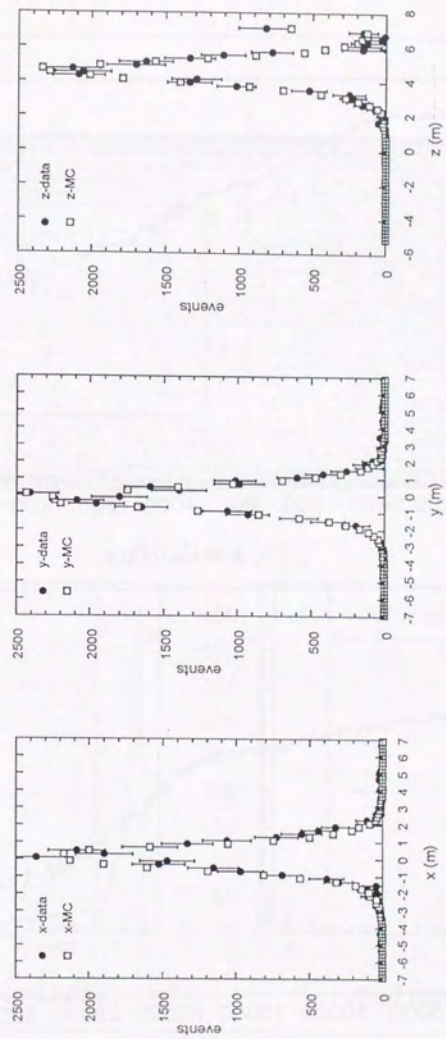


Fig. 5.9

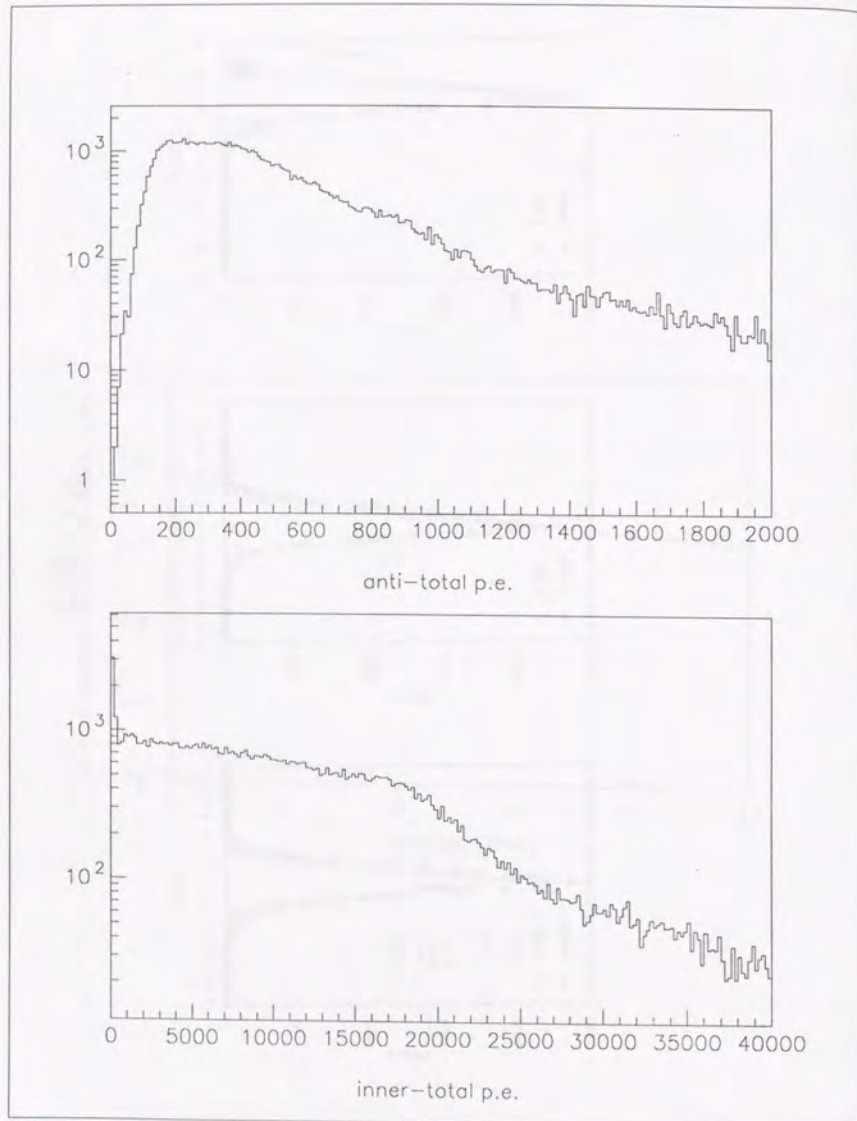


Fig. 5.10

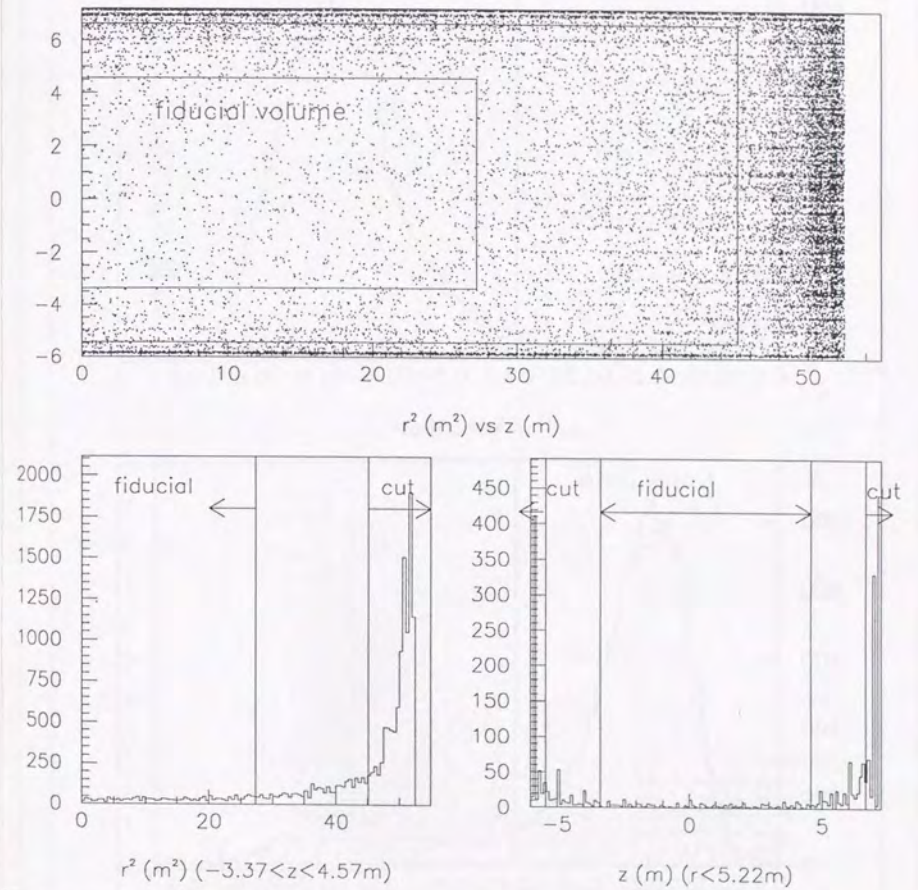


Fig. 5.11

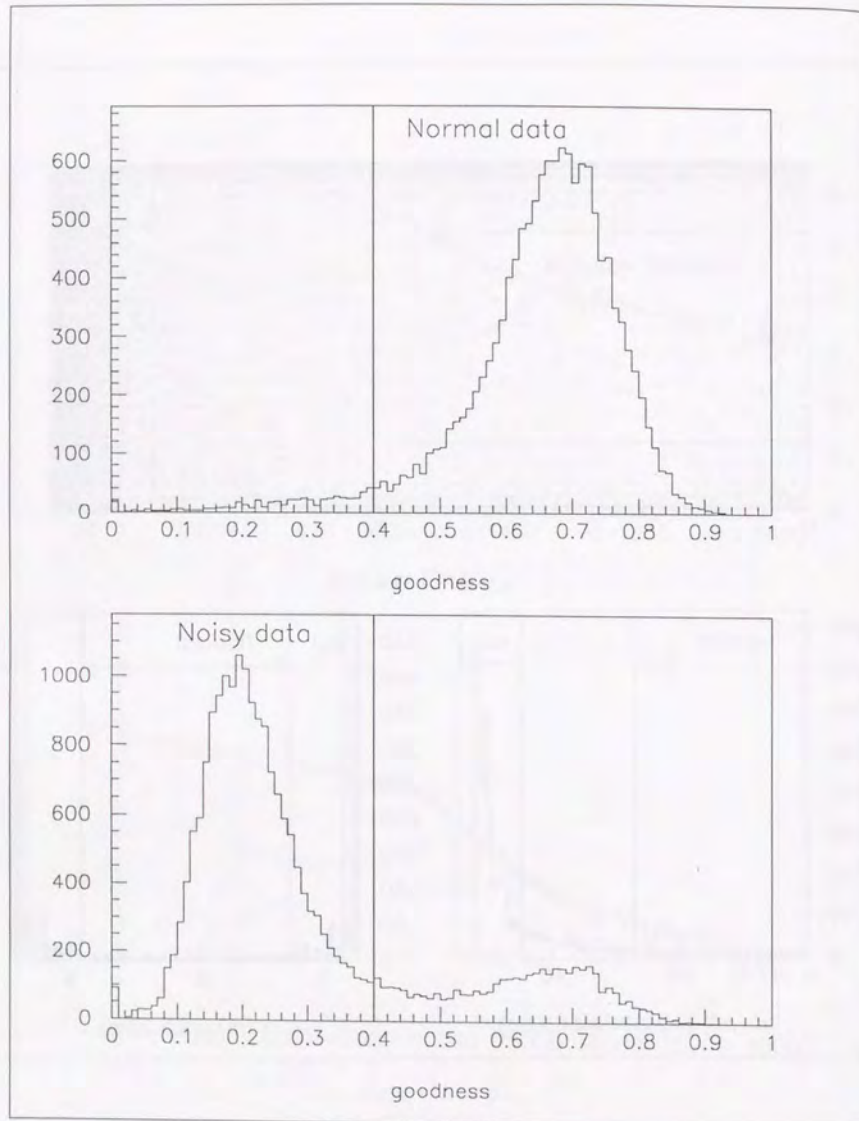


Fig. 5.12

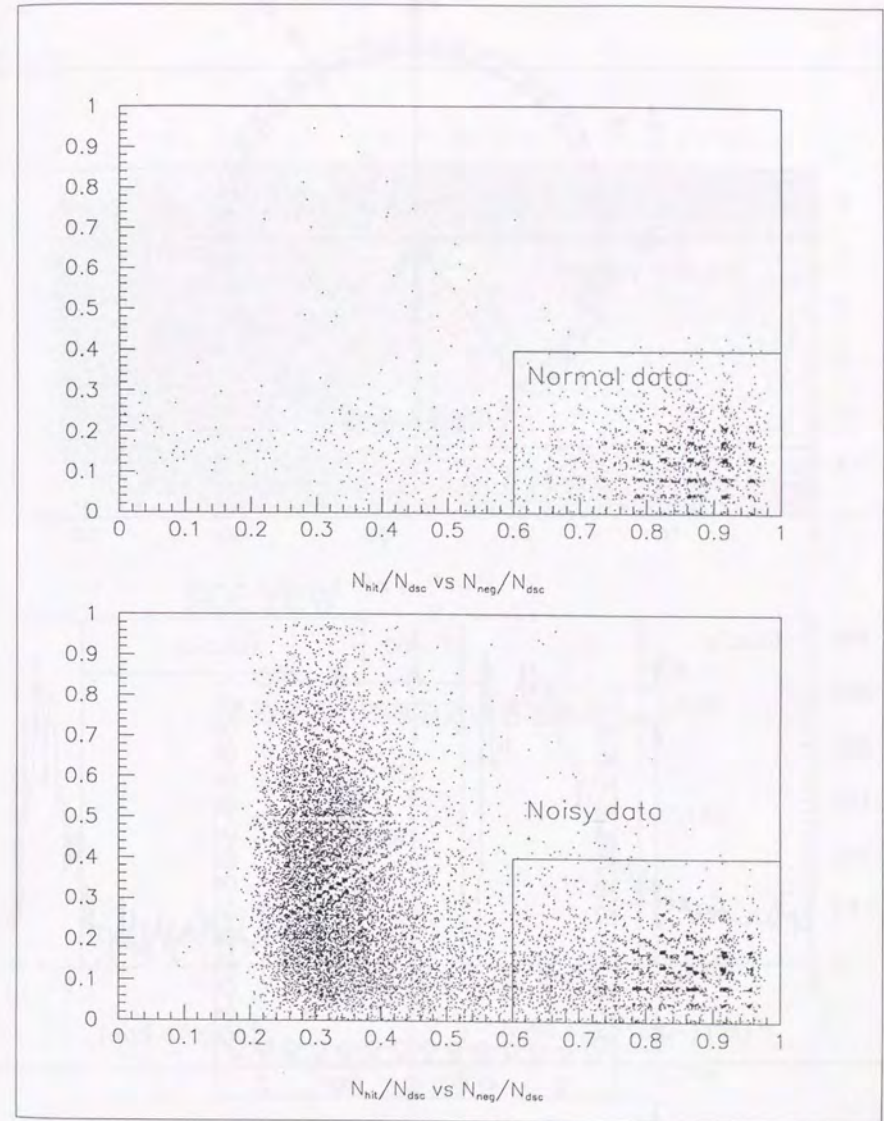


Fig. 5.13

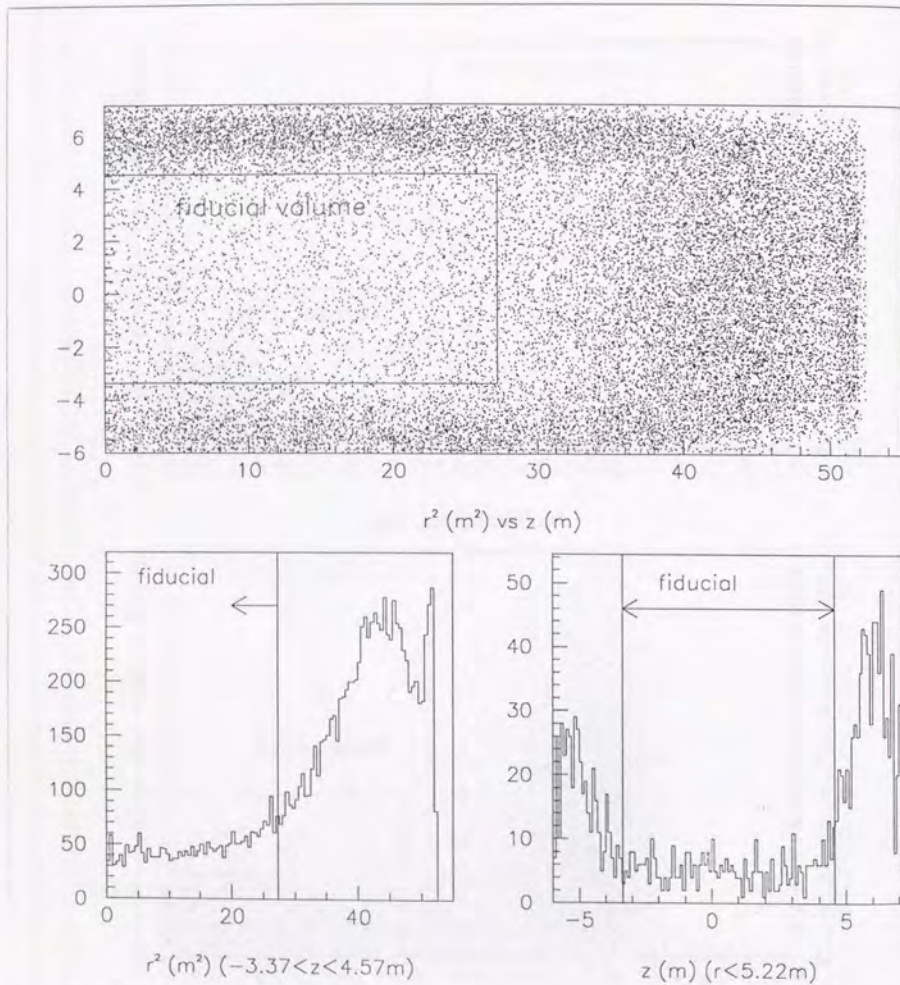
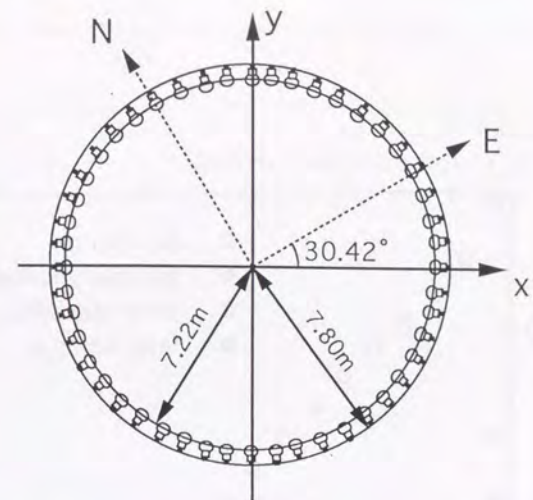


Fig. 5.14

TOP VIEW



SIDE VIEW

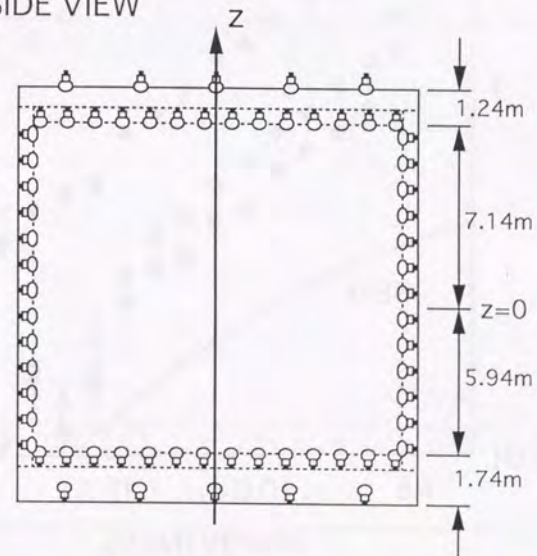


Fig. 5.15

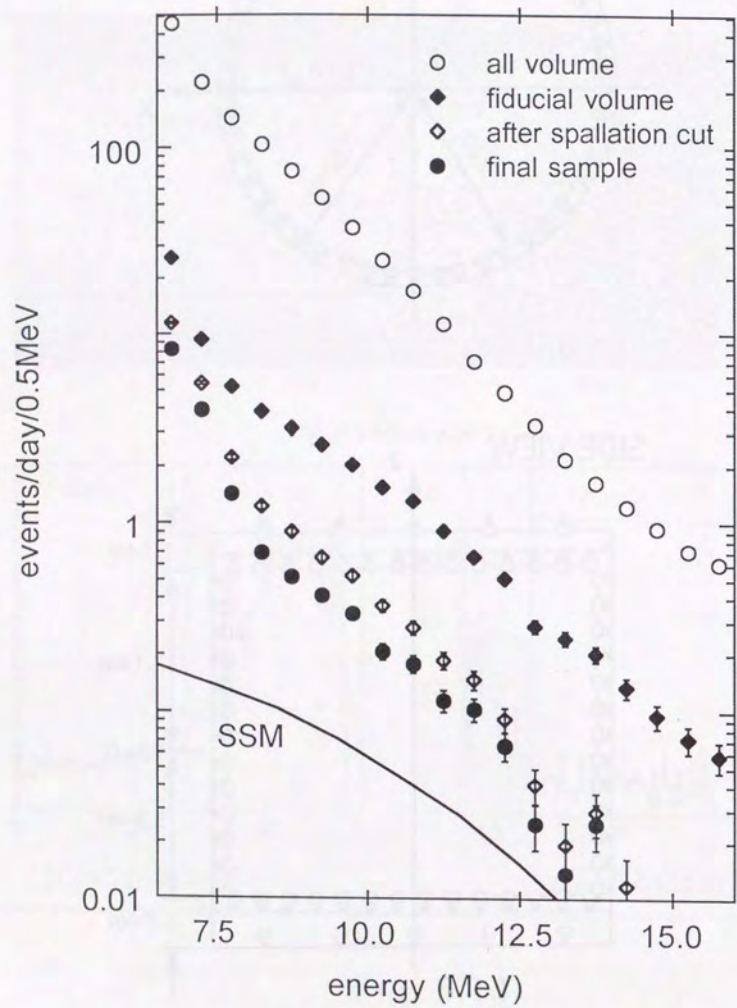


Fig. 5.16

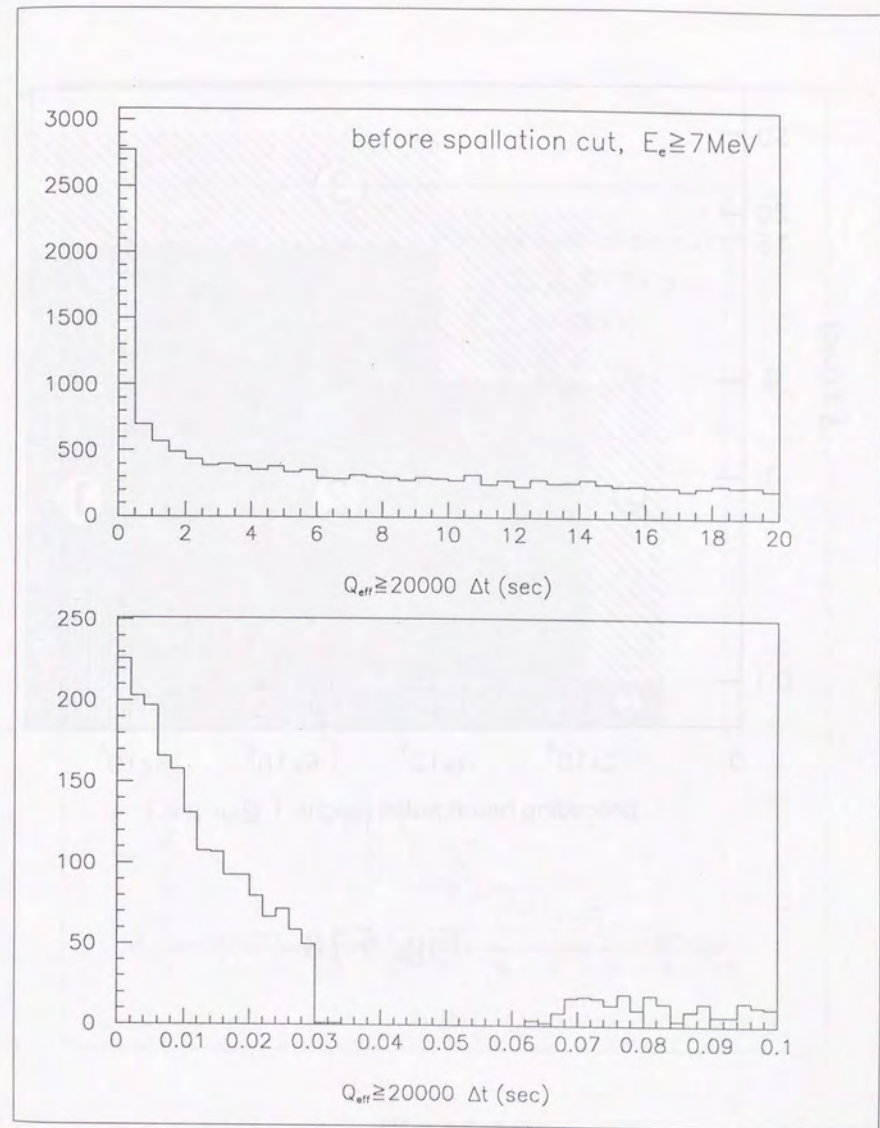


Fig. 5.17

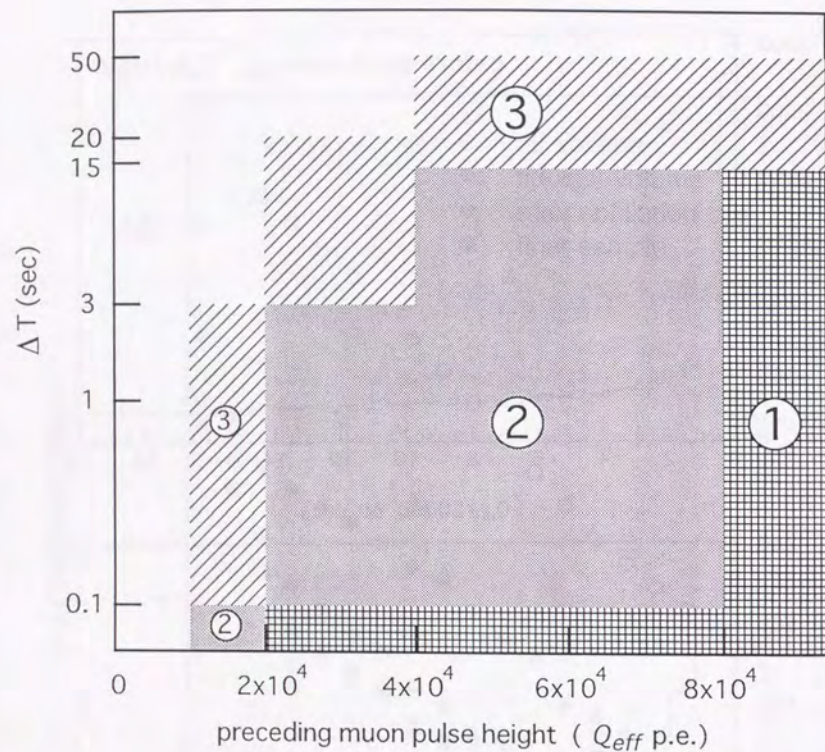


Fig. 5.18

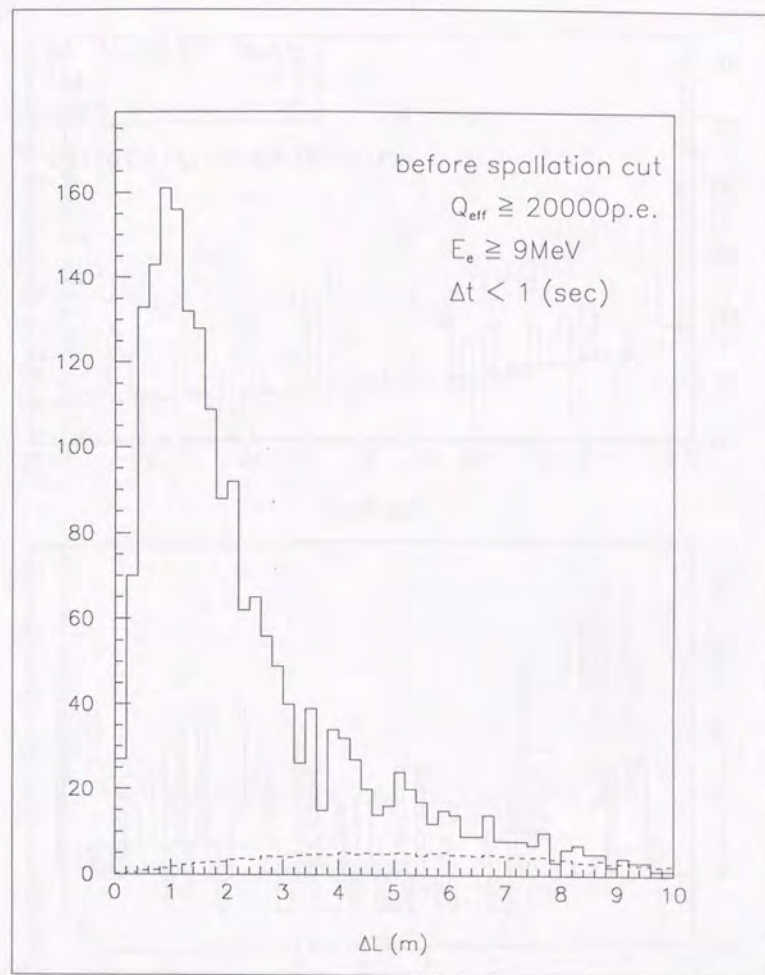


Fig. 5.19

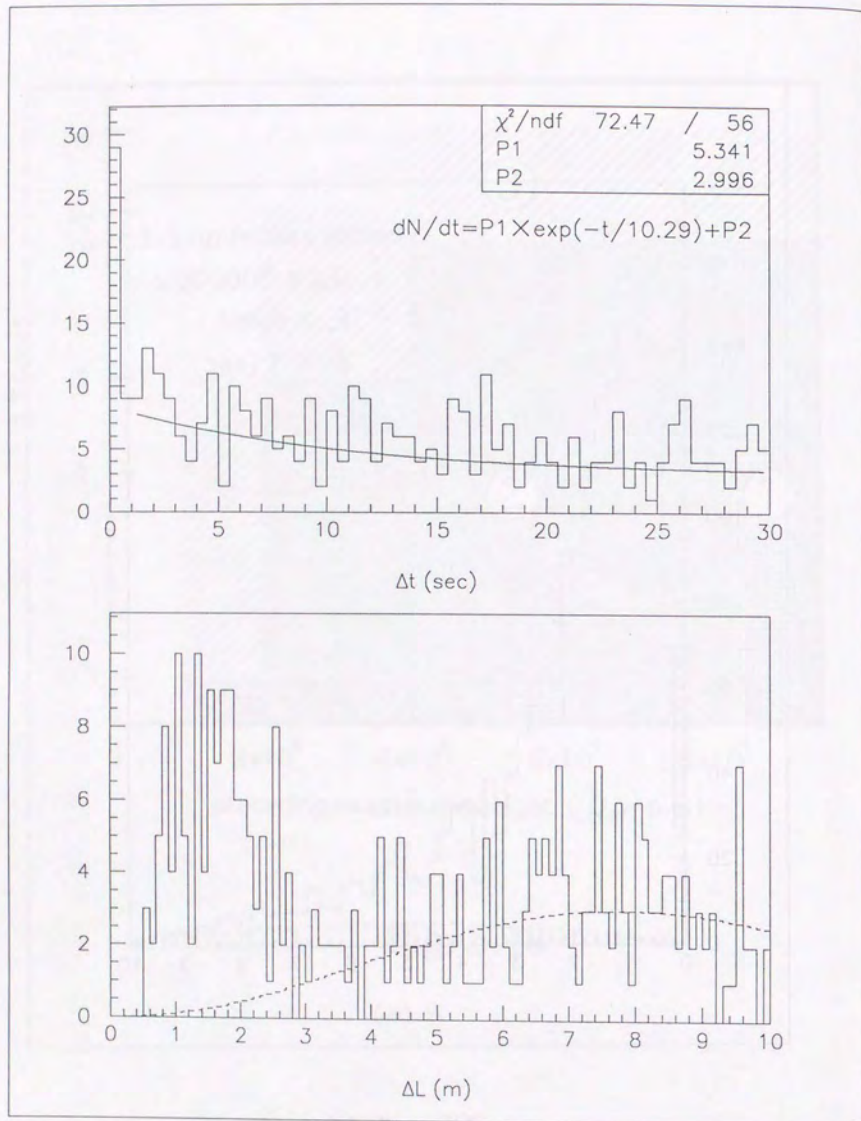


Fig. 5.20

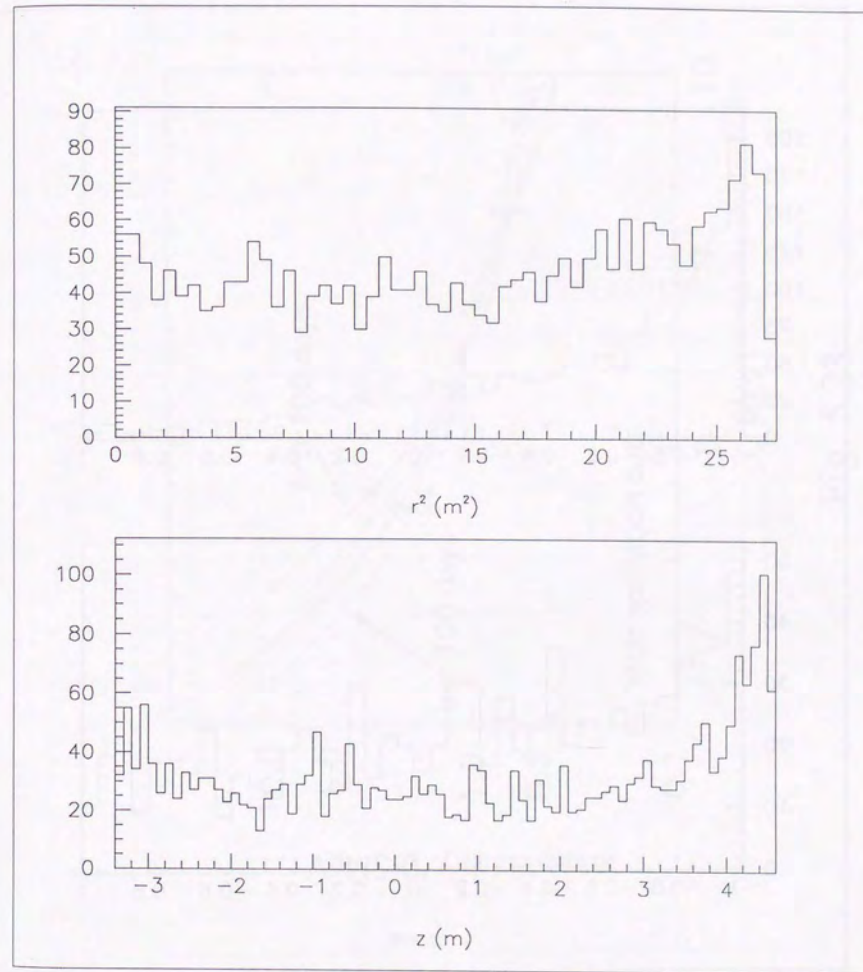


Fig. 5.21

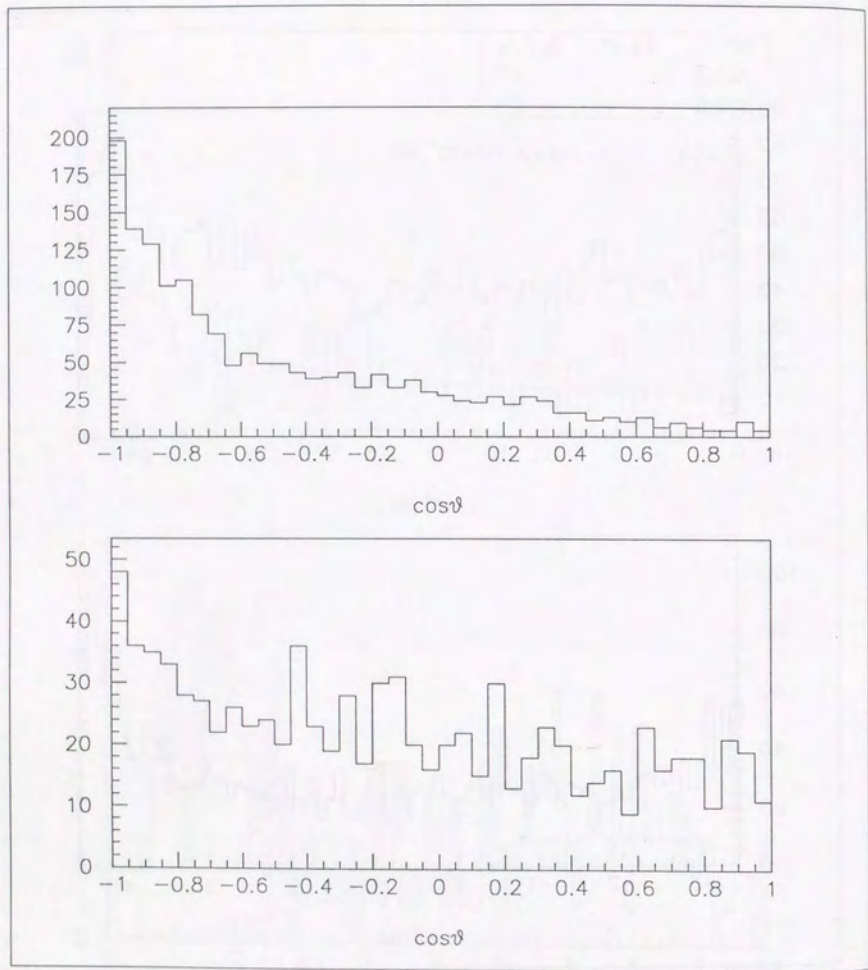


Fig. 5.22

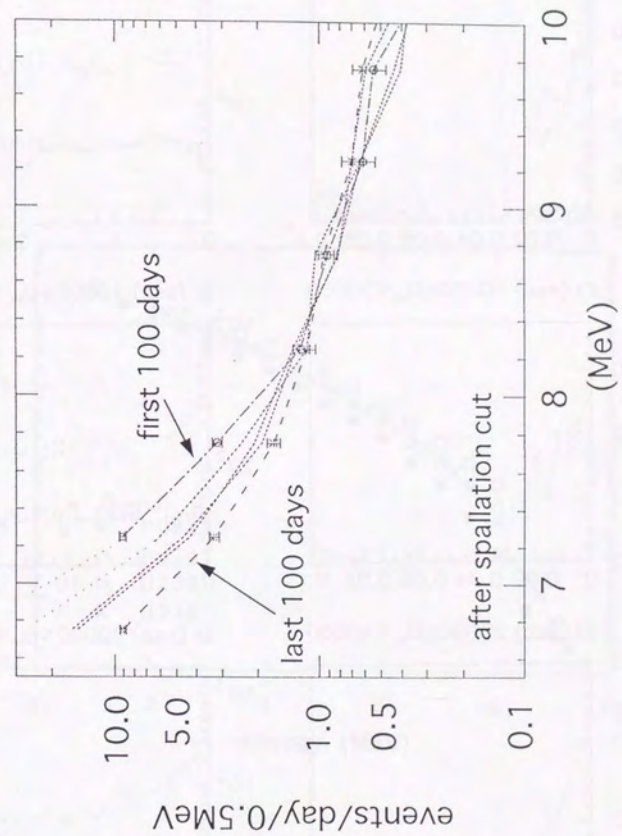


Fig. 5.23



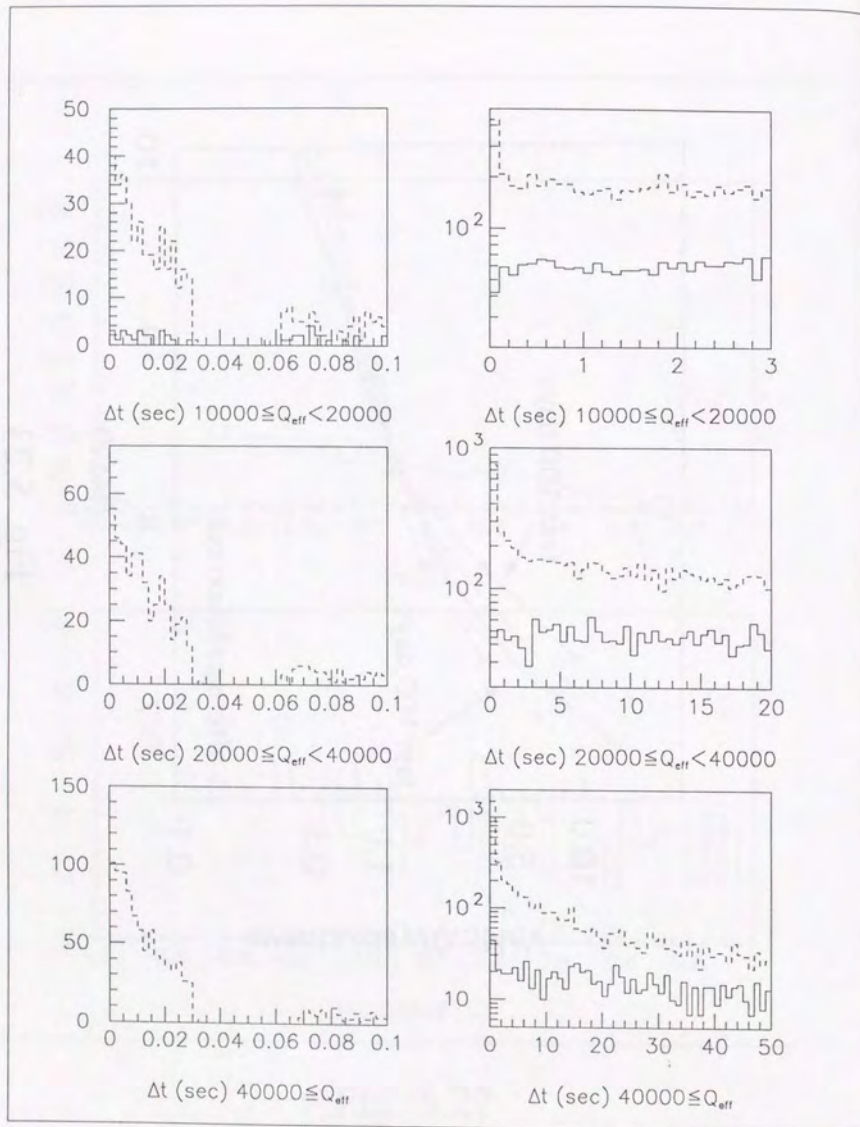


Fig. 5.24

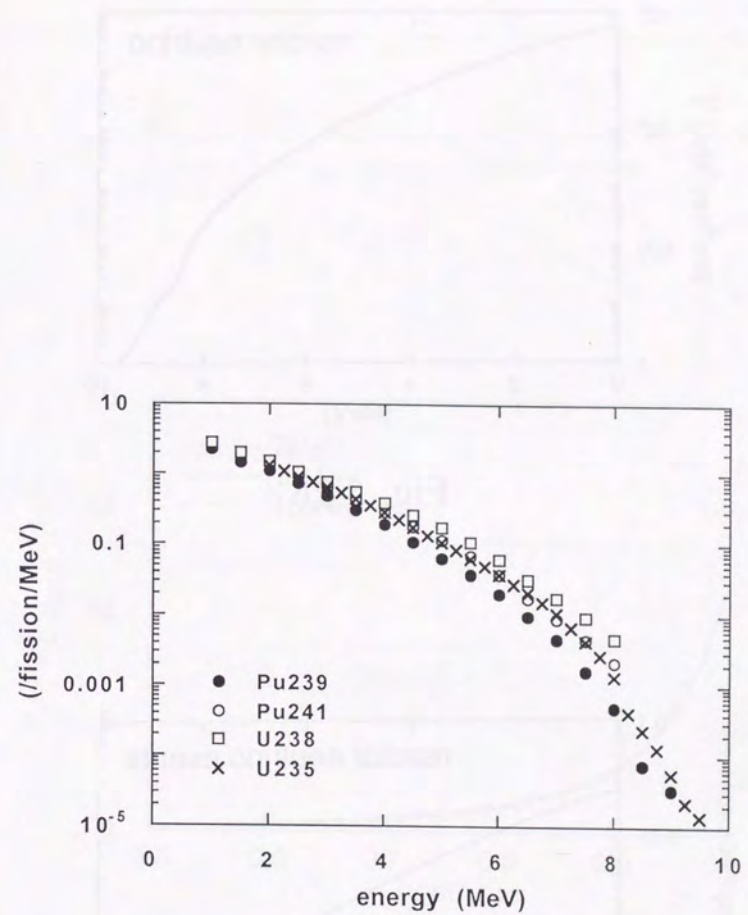


Fig. 5.25

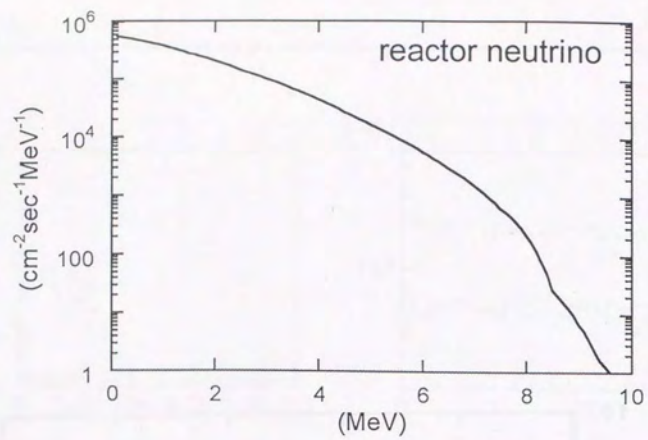


Fig. 5.26

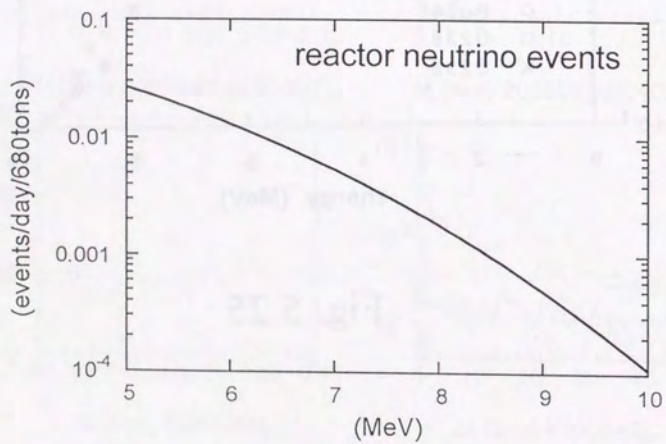


Fig. 5.27

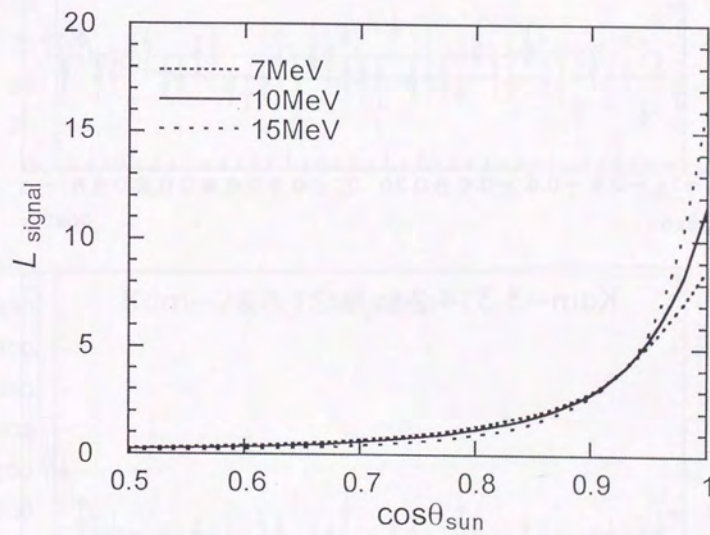


Fig. 6.1

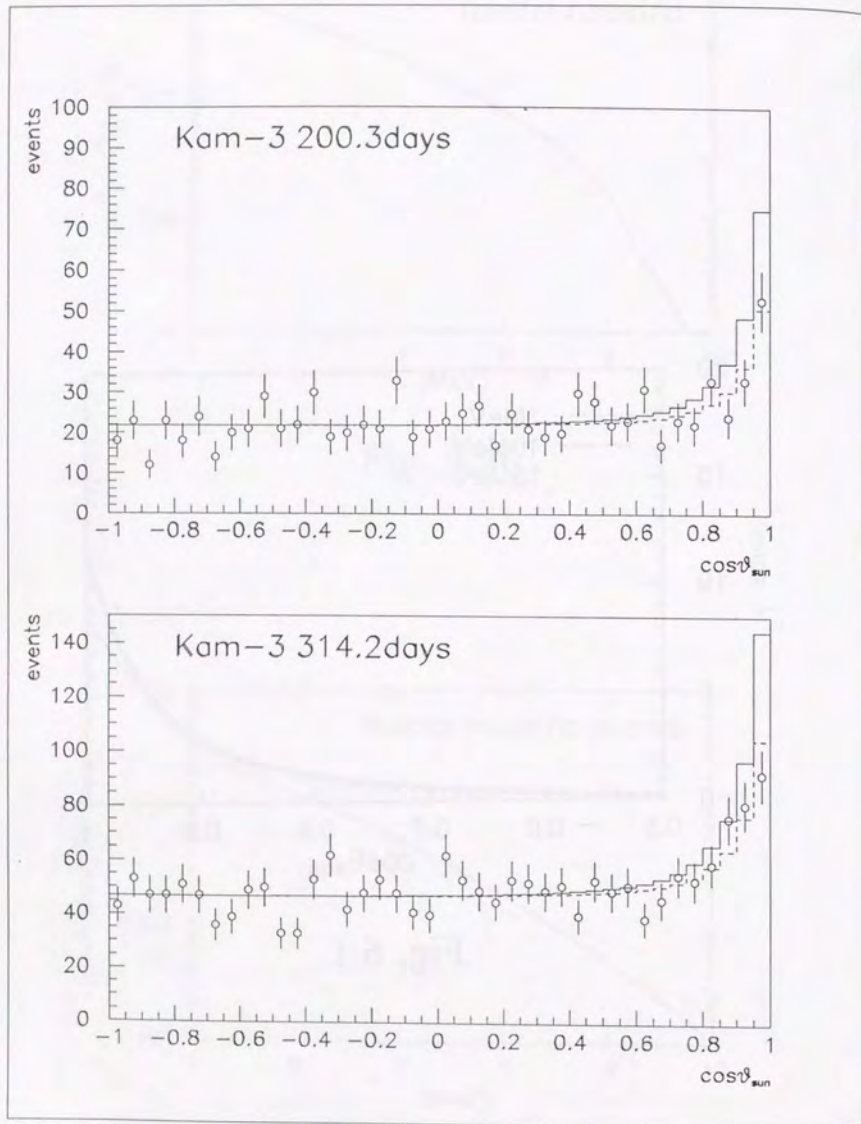


Fig. 6.2 (a)

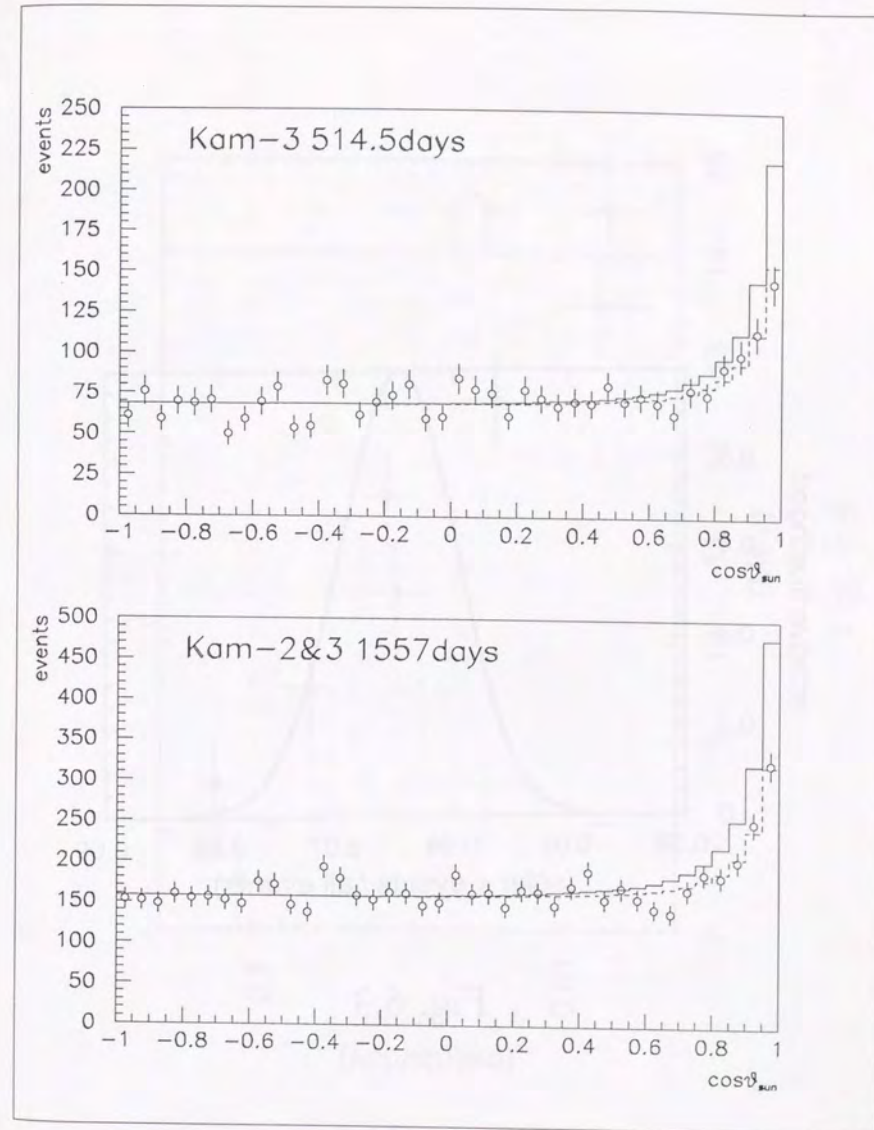


Fig. 6.2 (b)

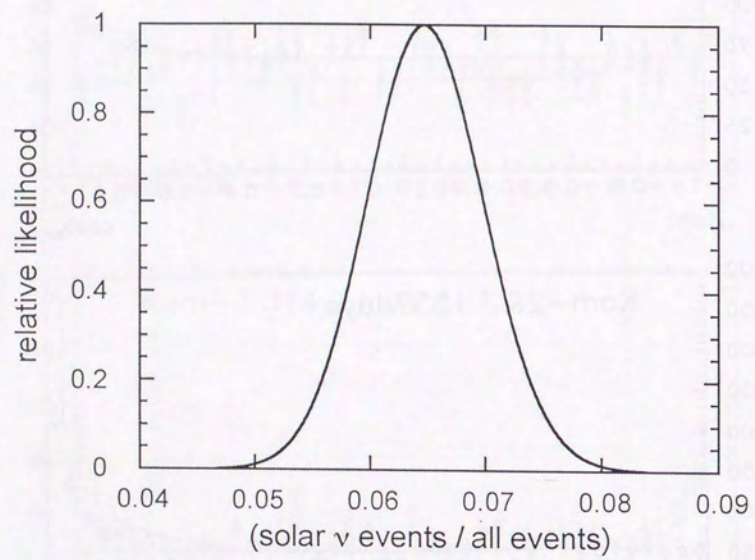


Fig. 6.3

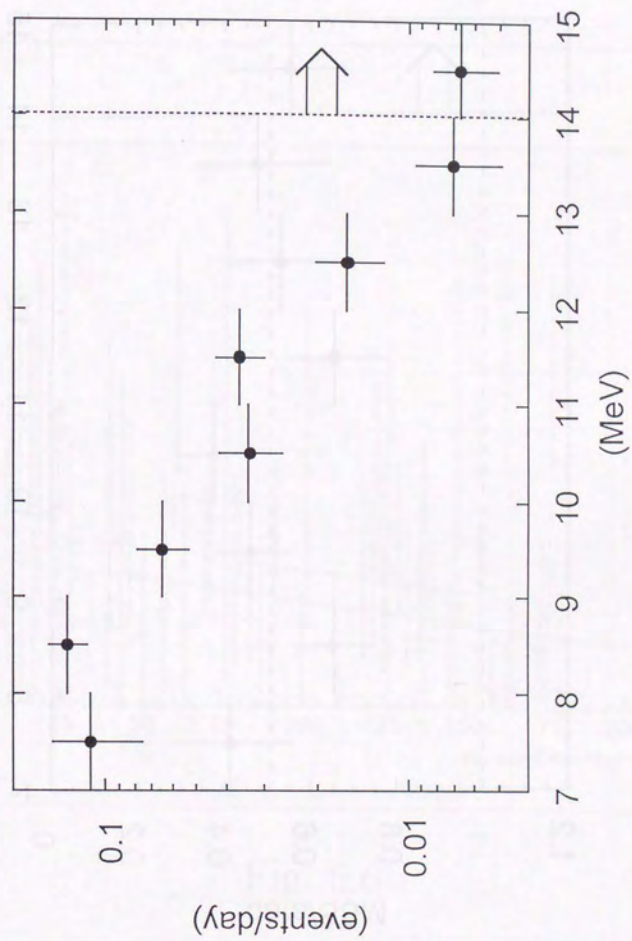


Fig. 6.4

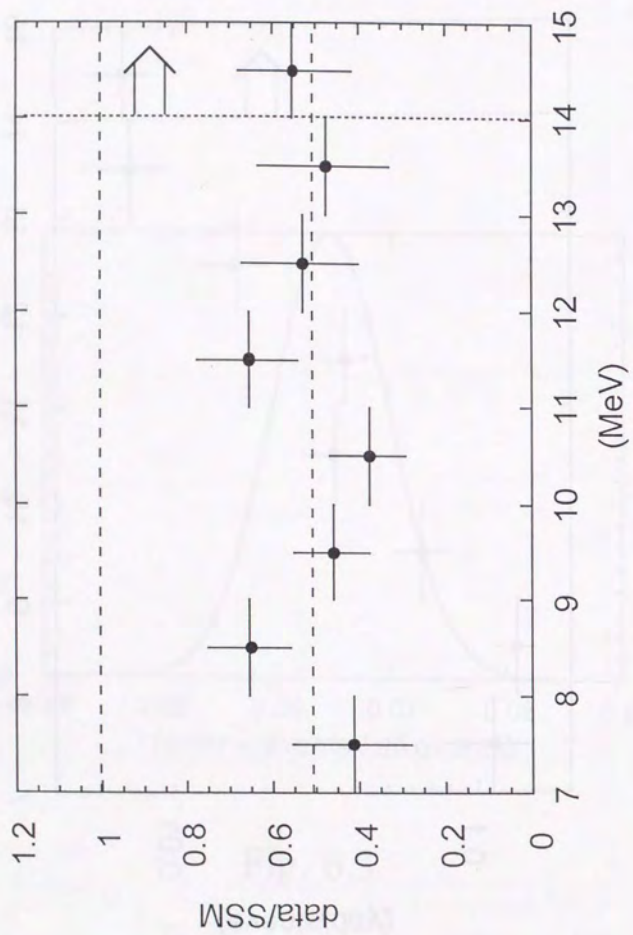


Fig. 6.5

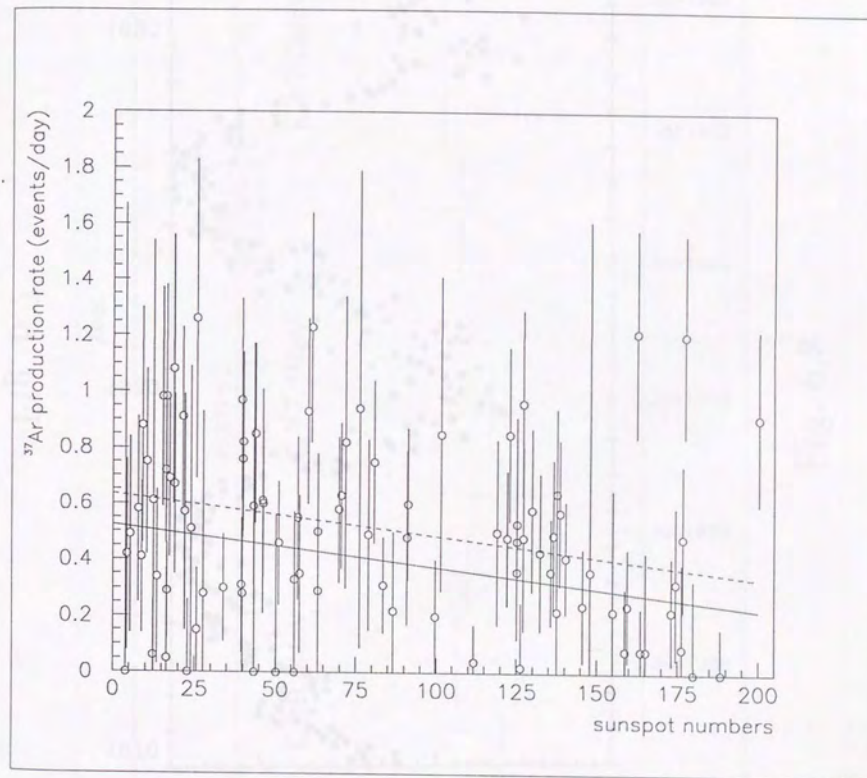


Fig. 6.6

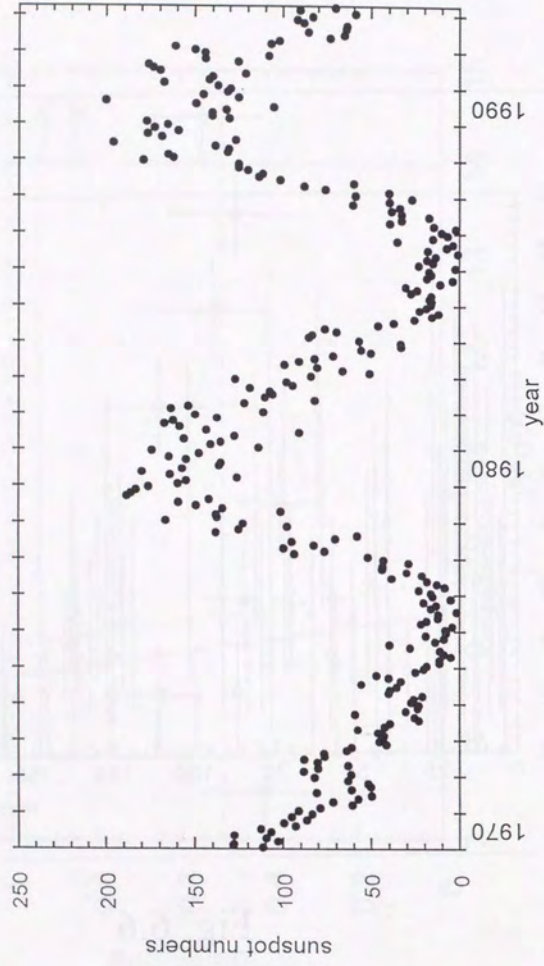


Fig. 6.7

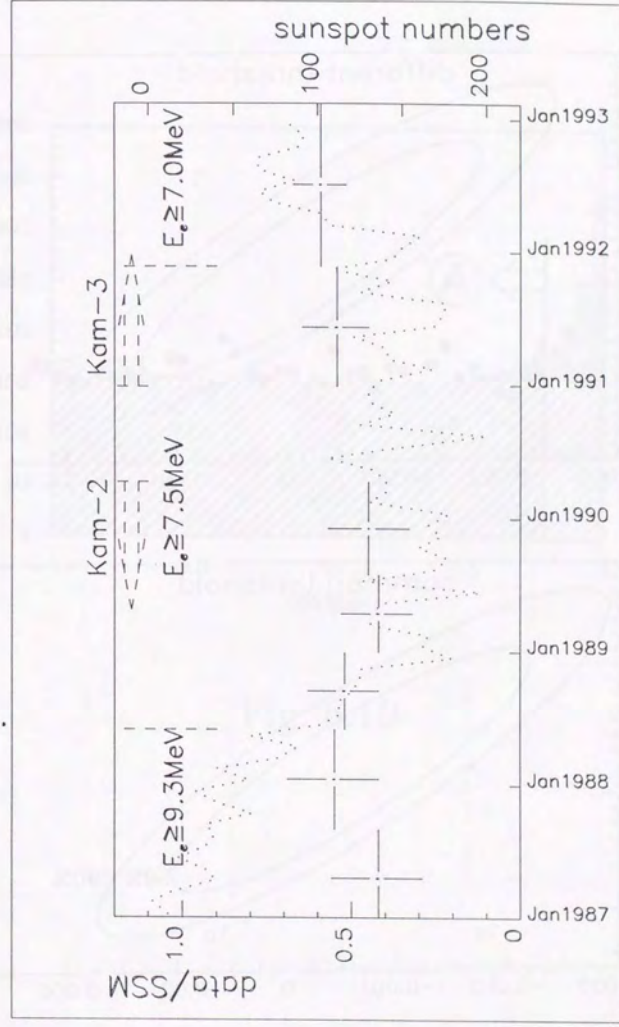


Fig. 6.8

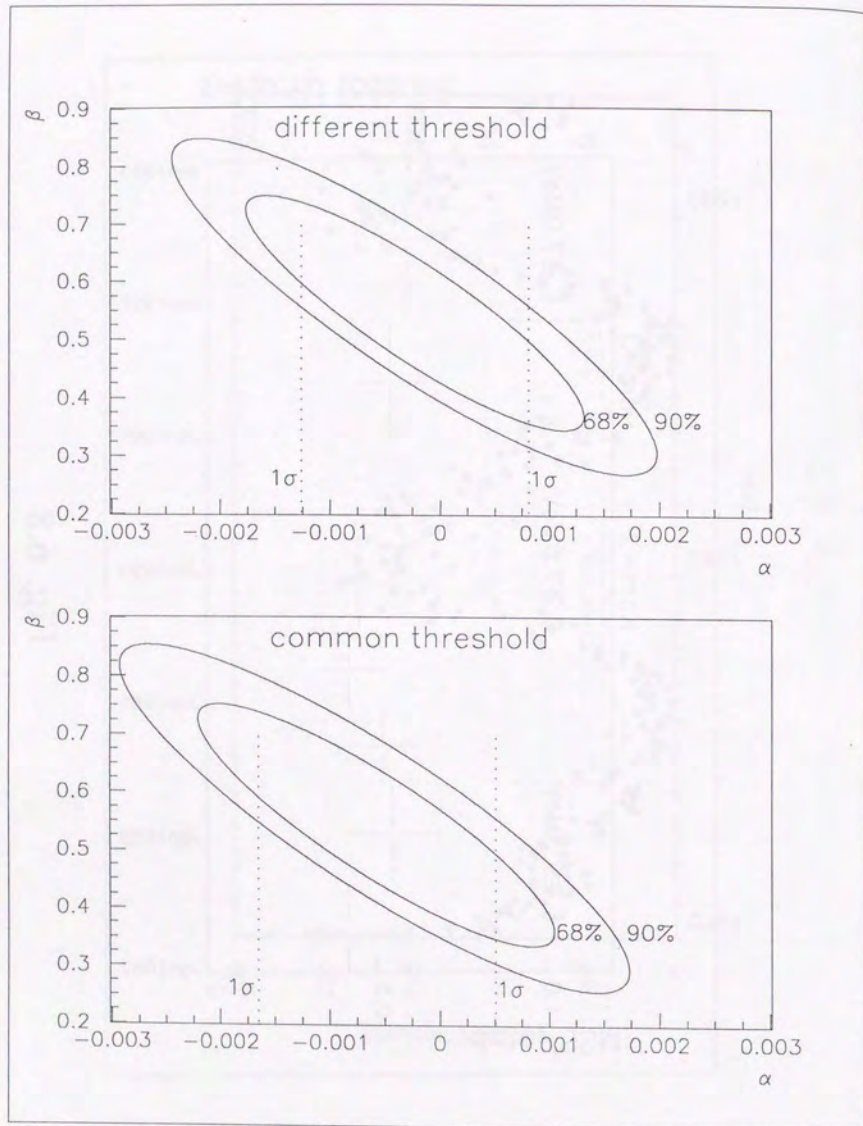


Fig. 6.9

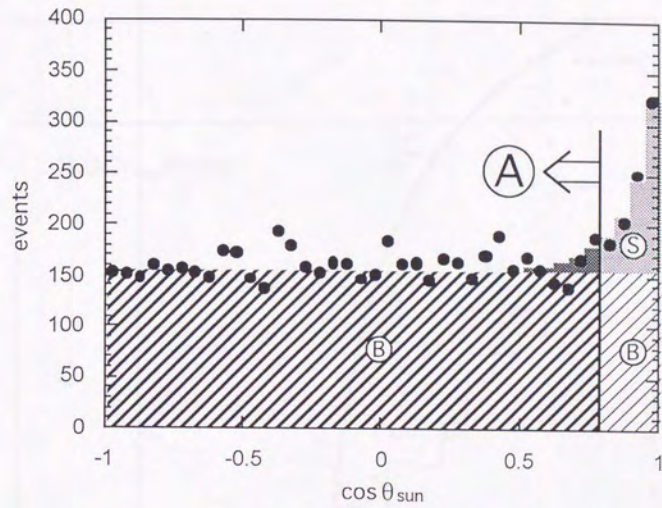


Fig. 6.10

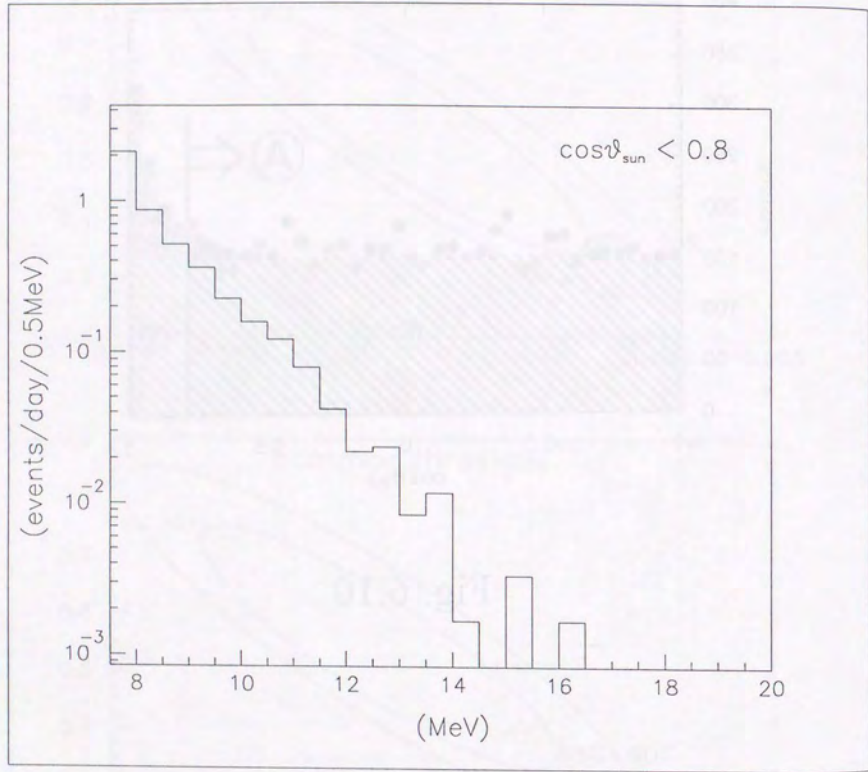


Fig. 6.11

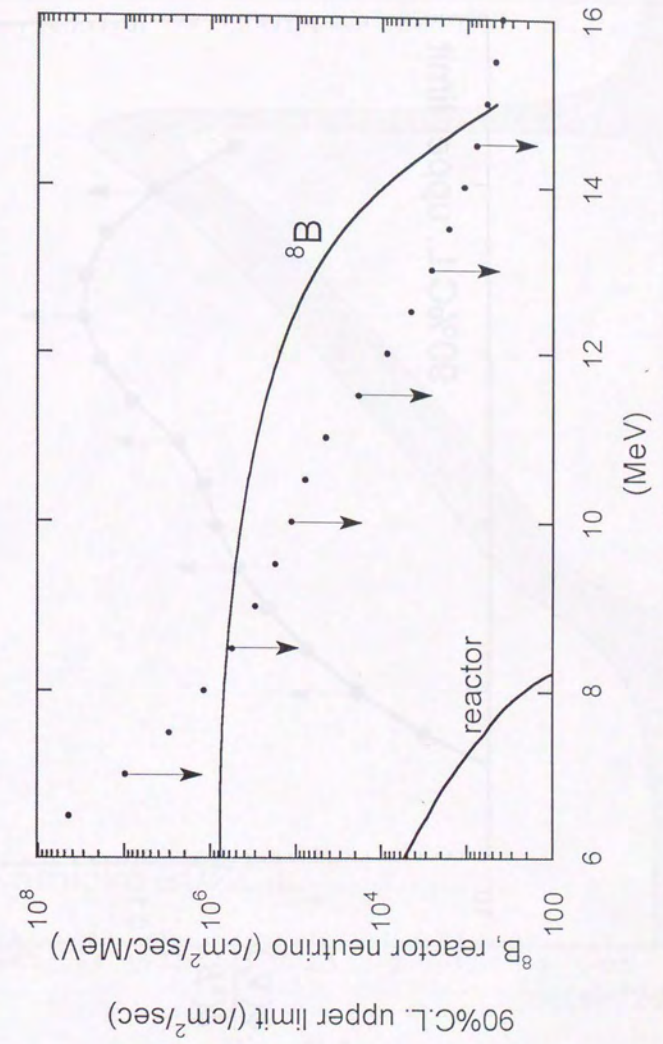


Fig. 6.12



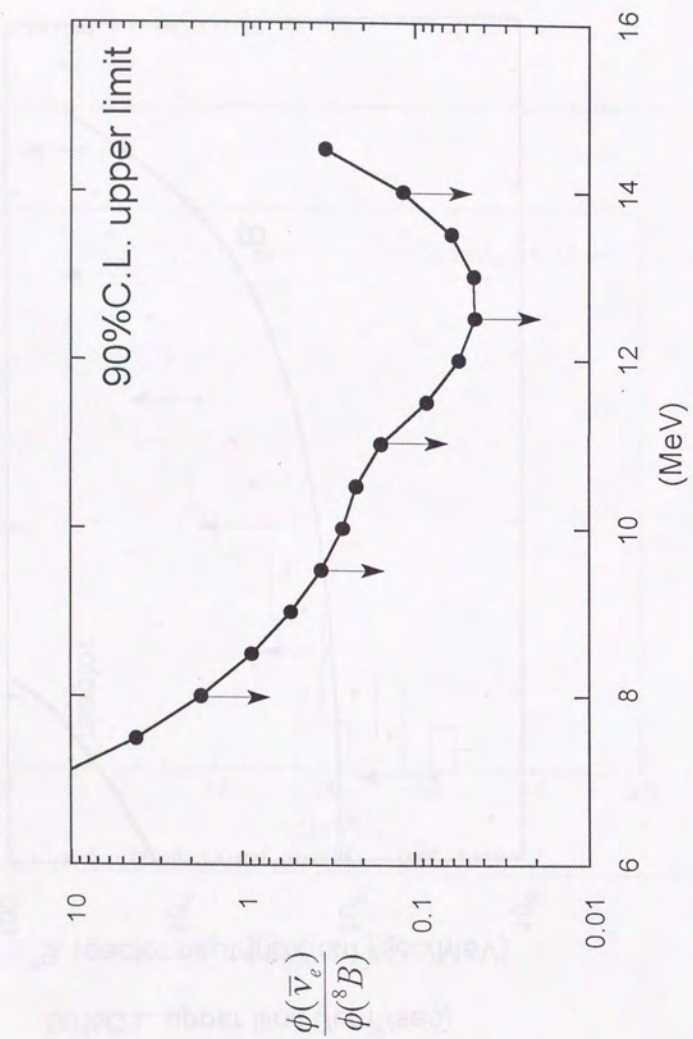


Fig. 6.13

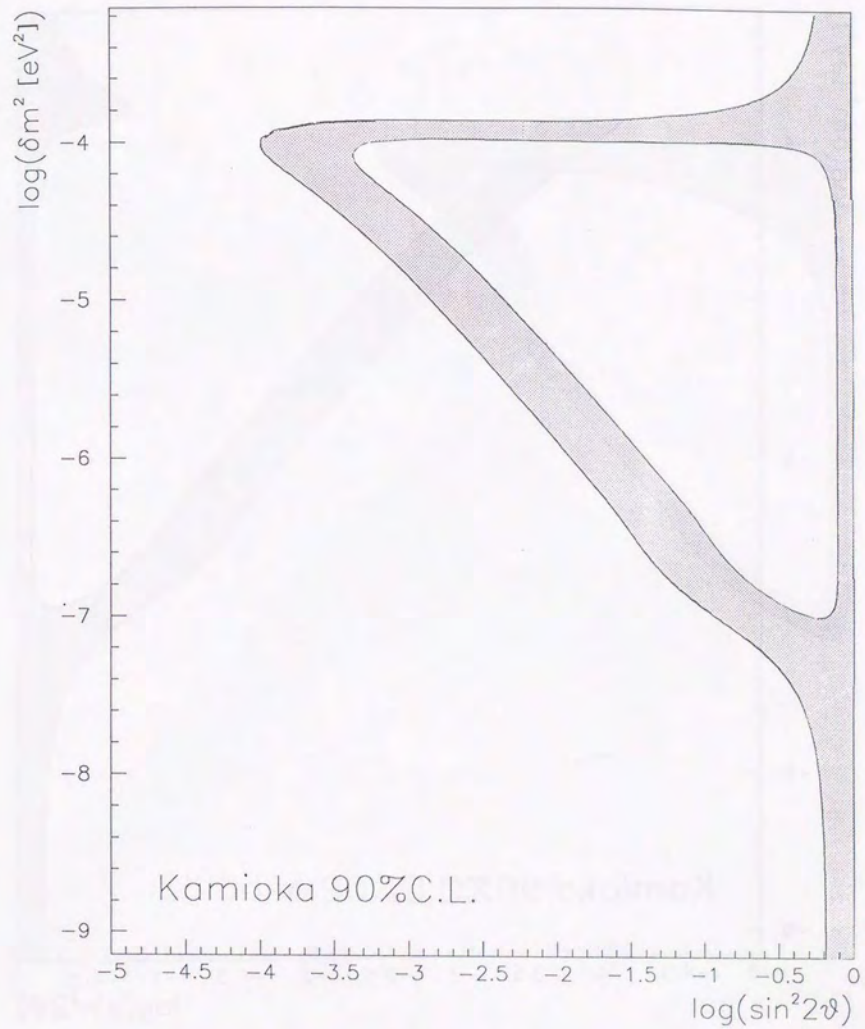


Fig. 7.1

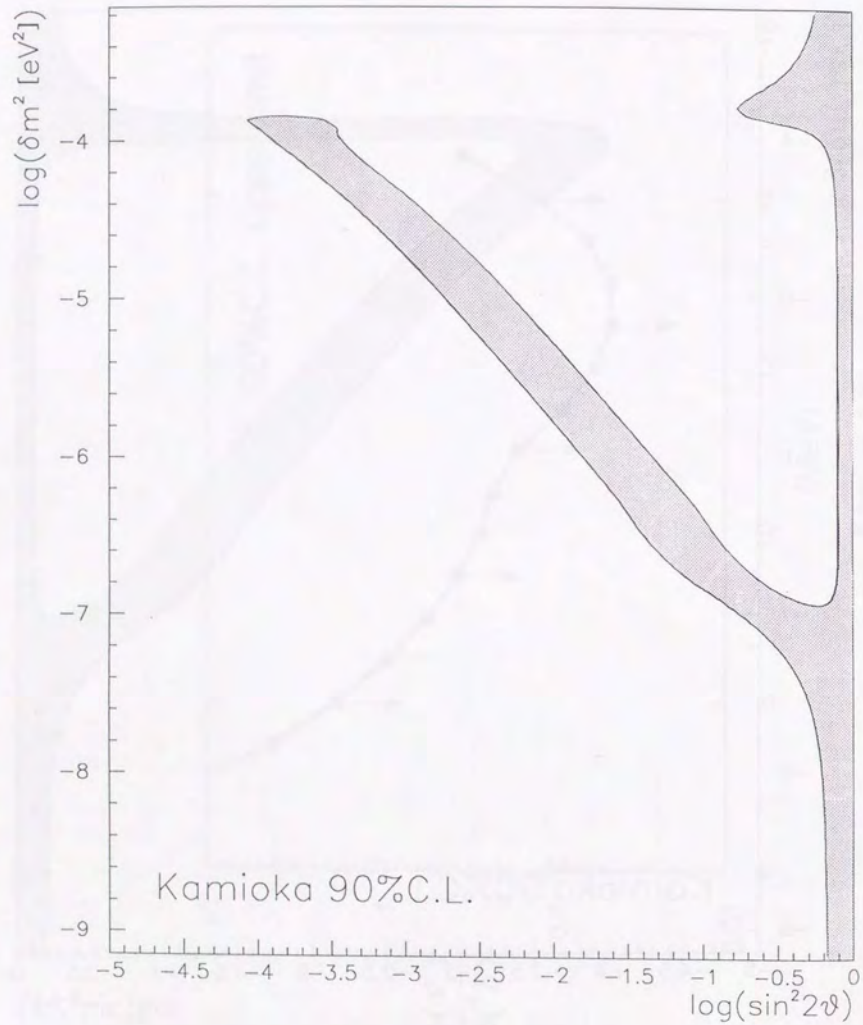


Fig. 7.2

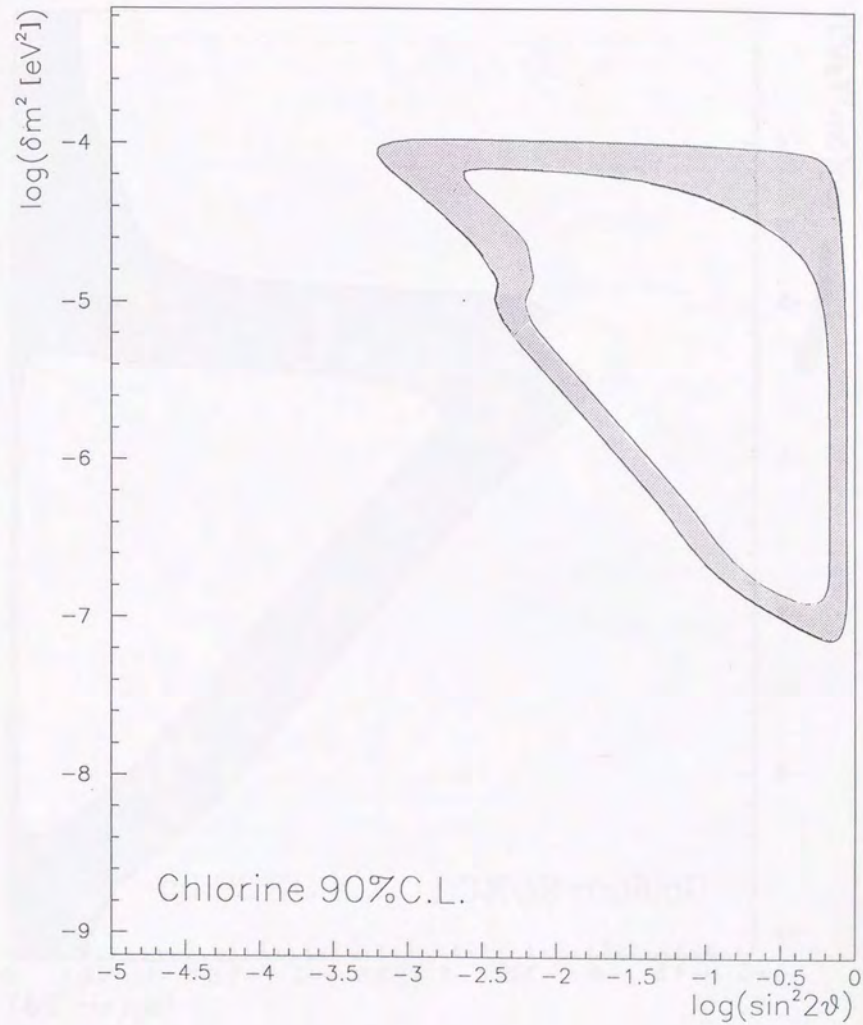


Fig. 7.3

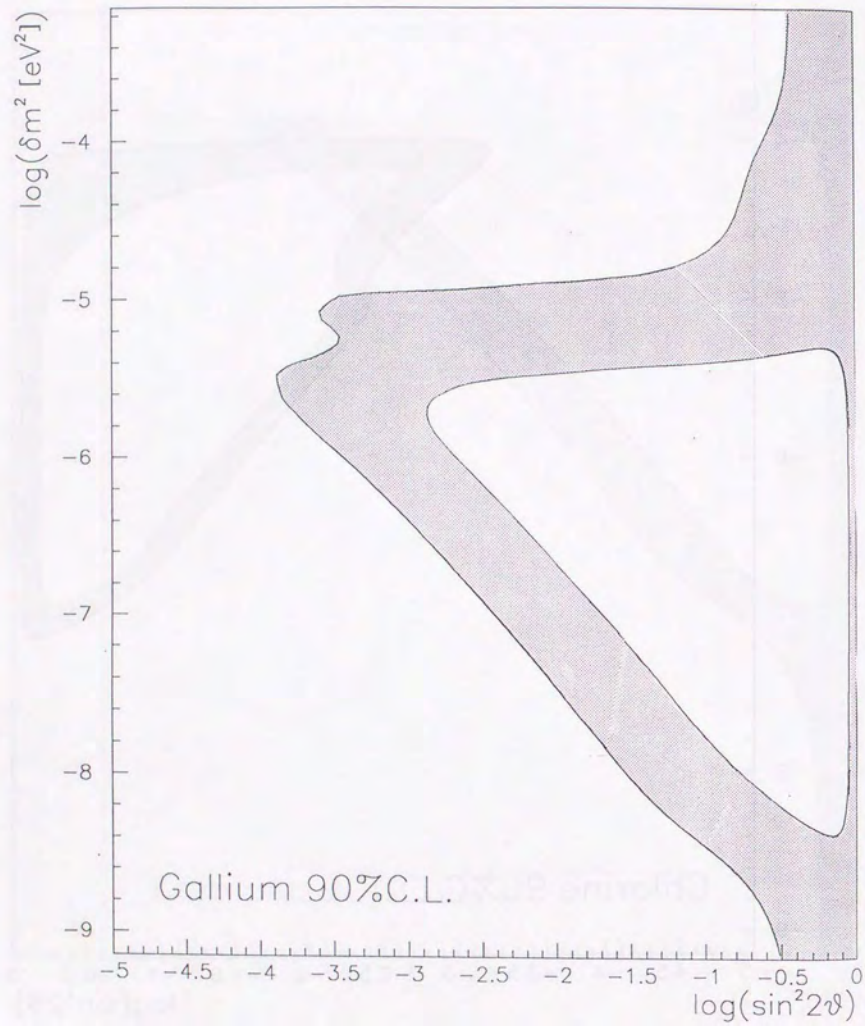


Fig. 7.4

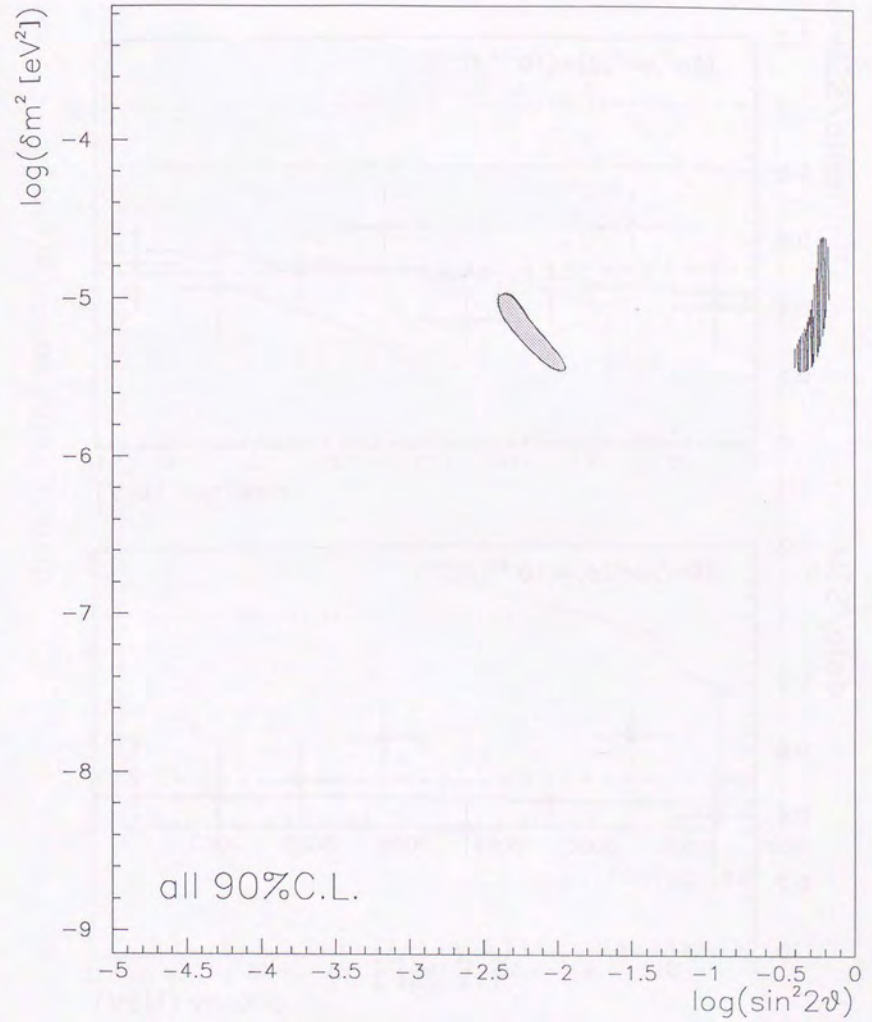


Fig. 7.5

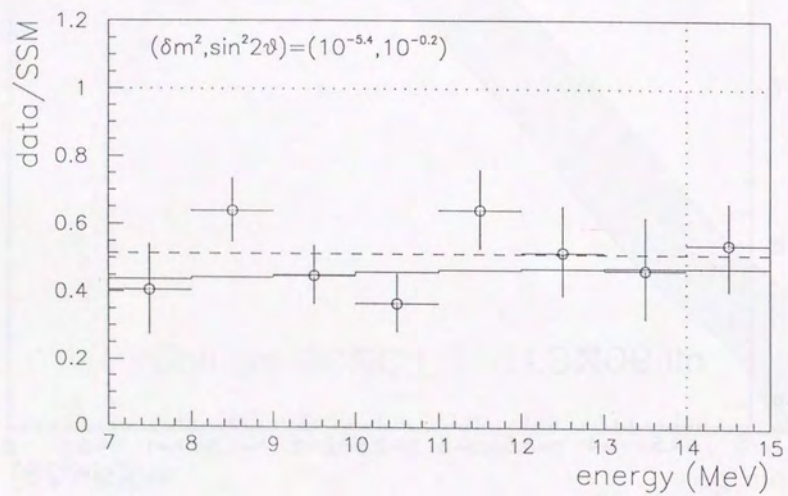
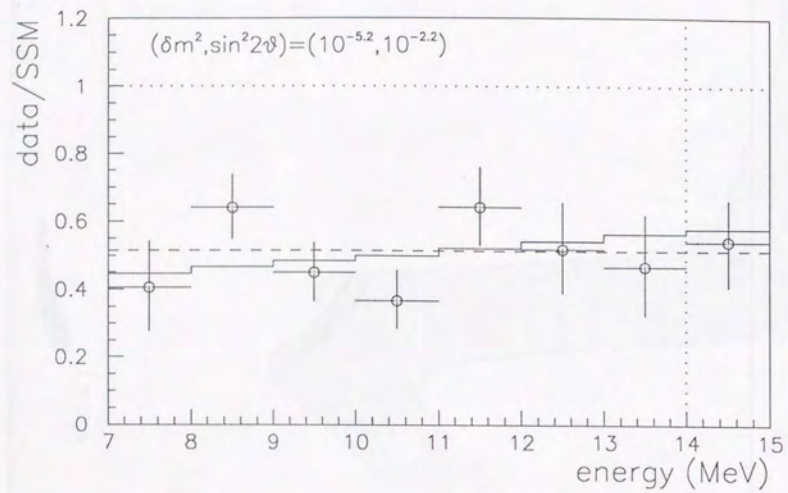


Fig. 7.6

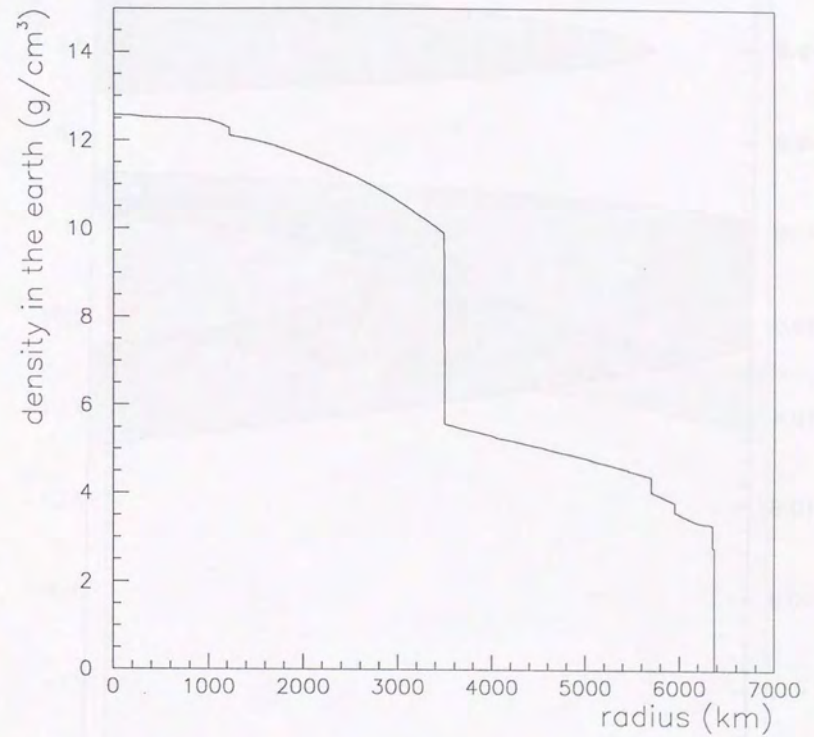


Fig. 7.7

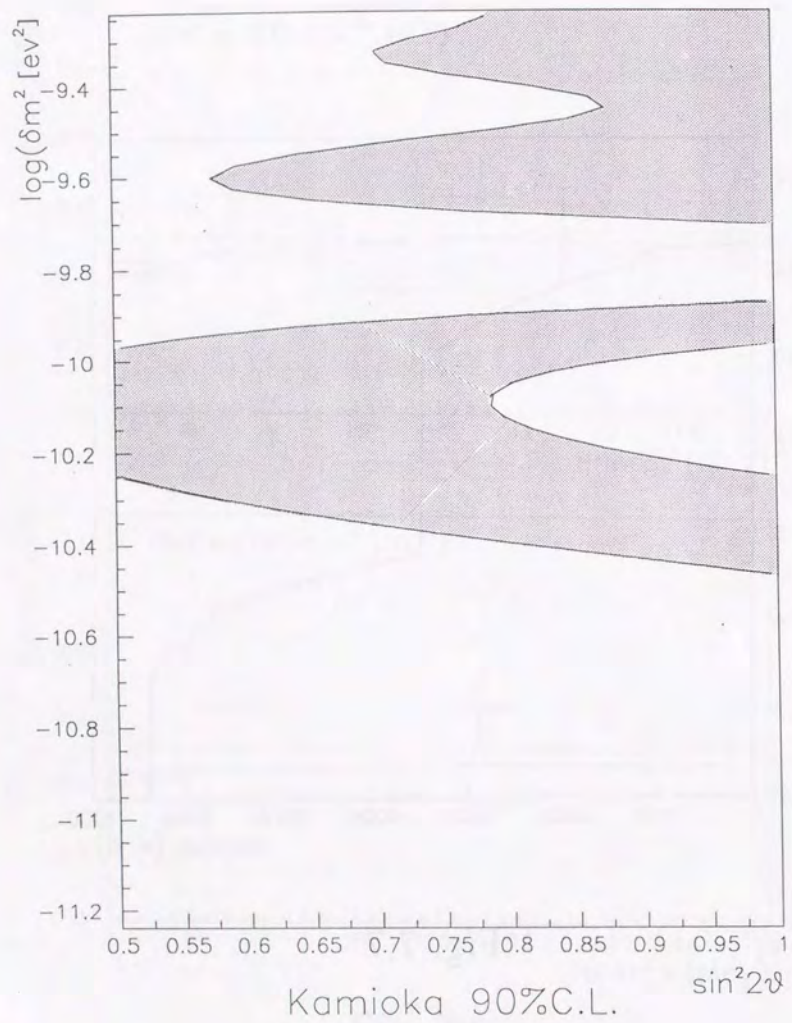


Fig. 7.8

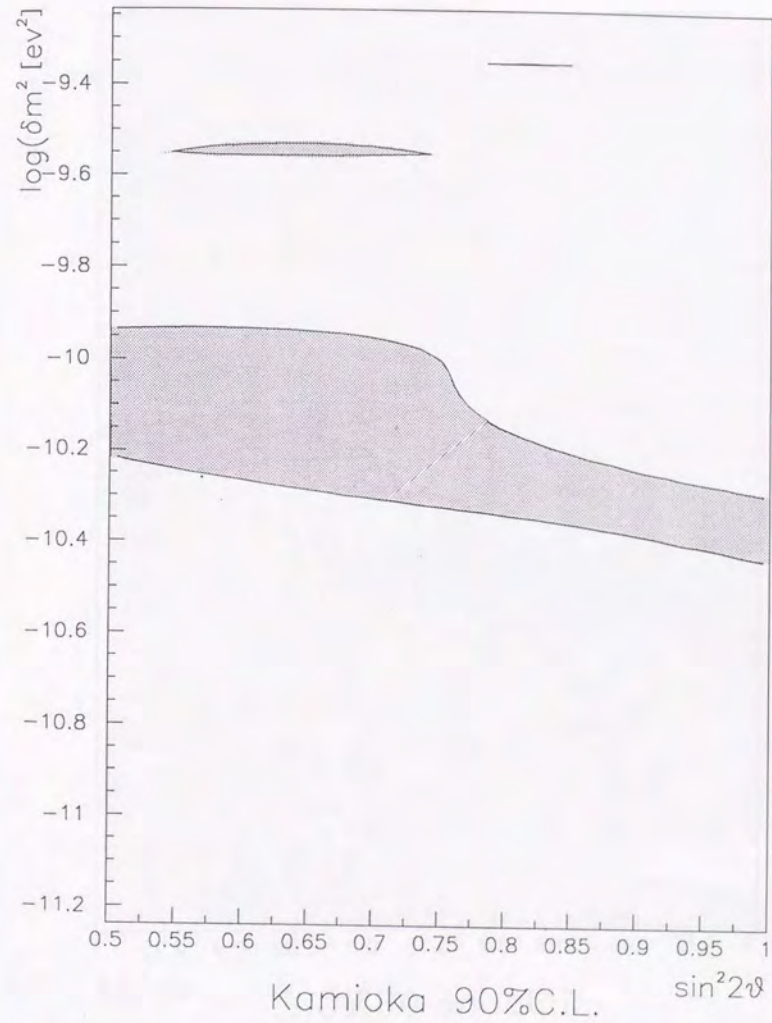


Fig. 7.9

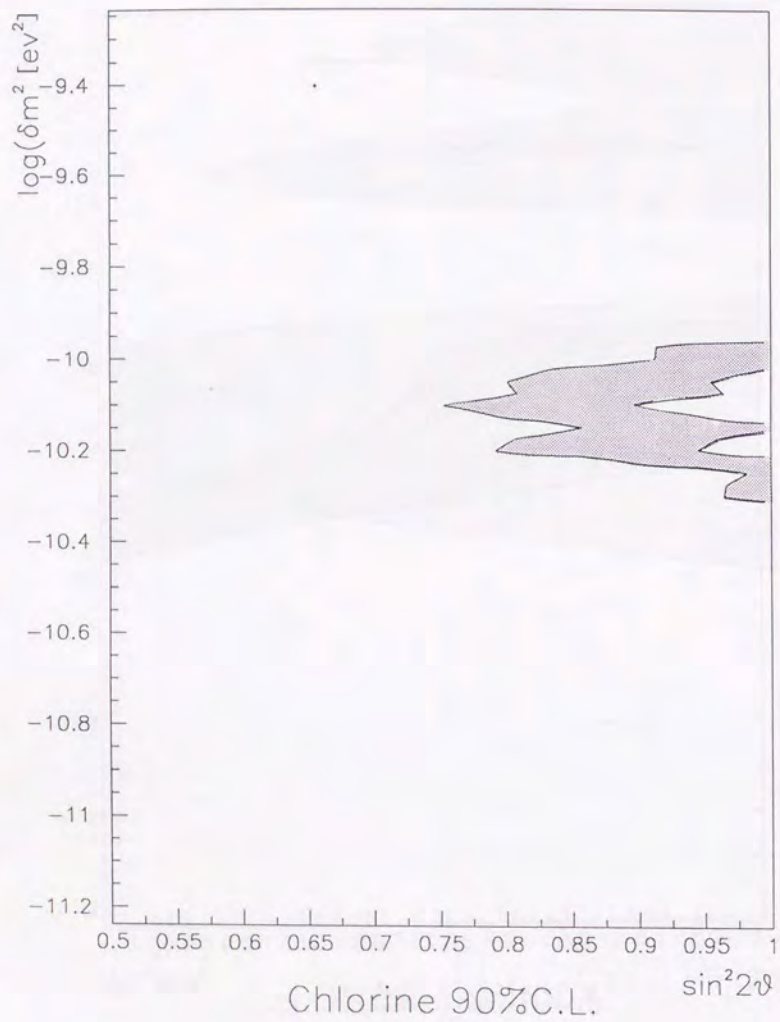


Fig. 7.10

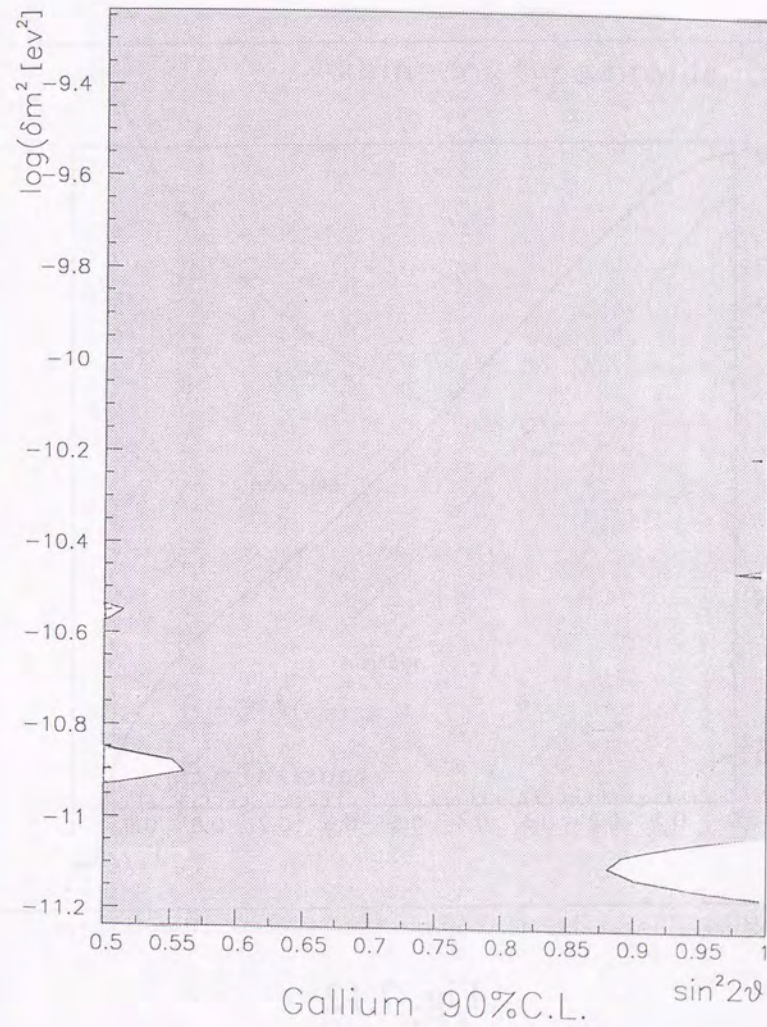


Fig. 7.11

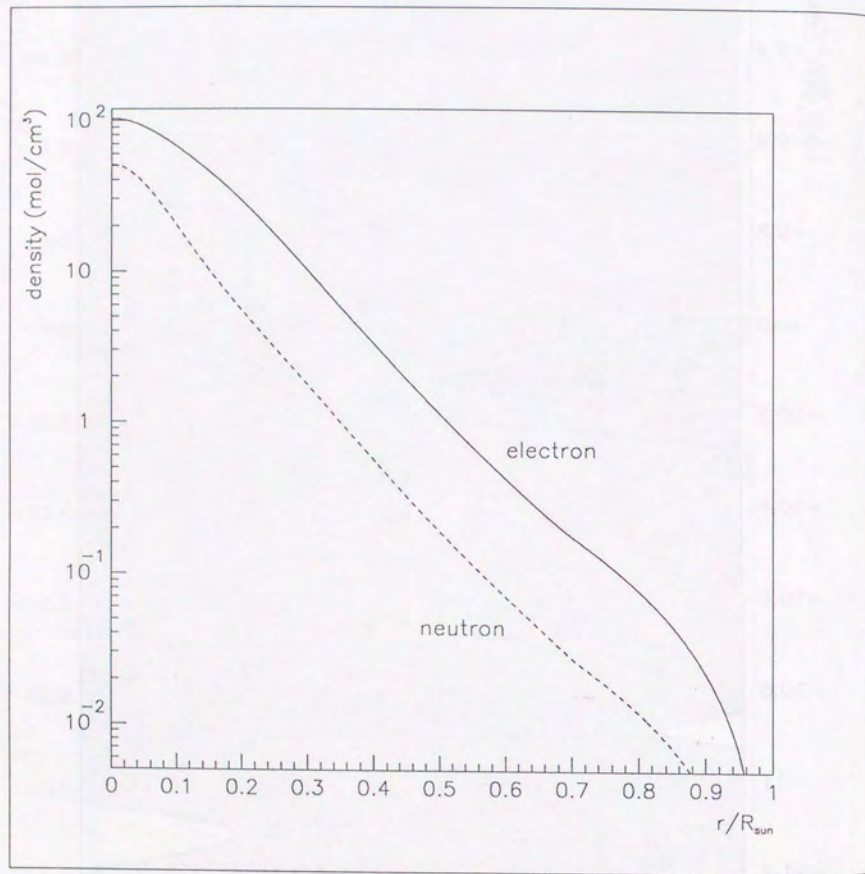


Fig. 7.12

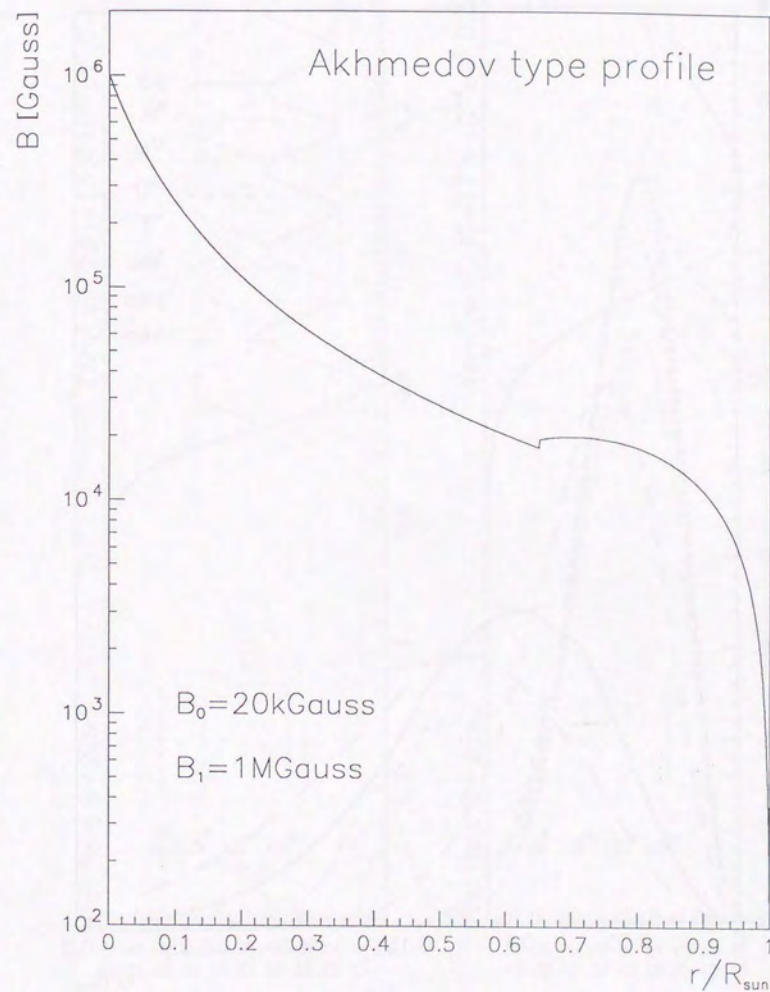


Fig. 7.13

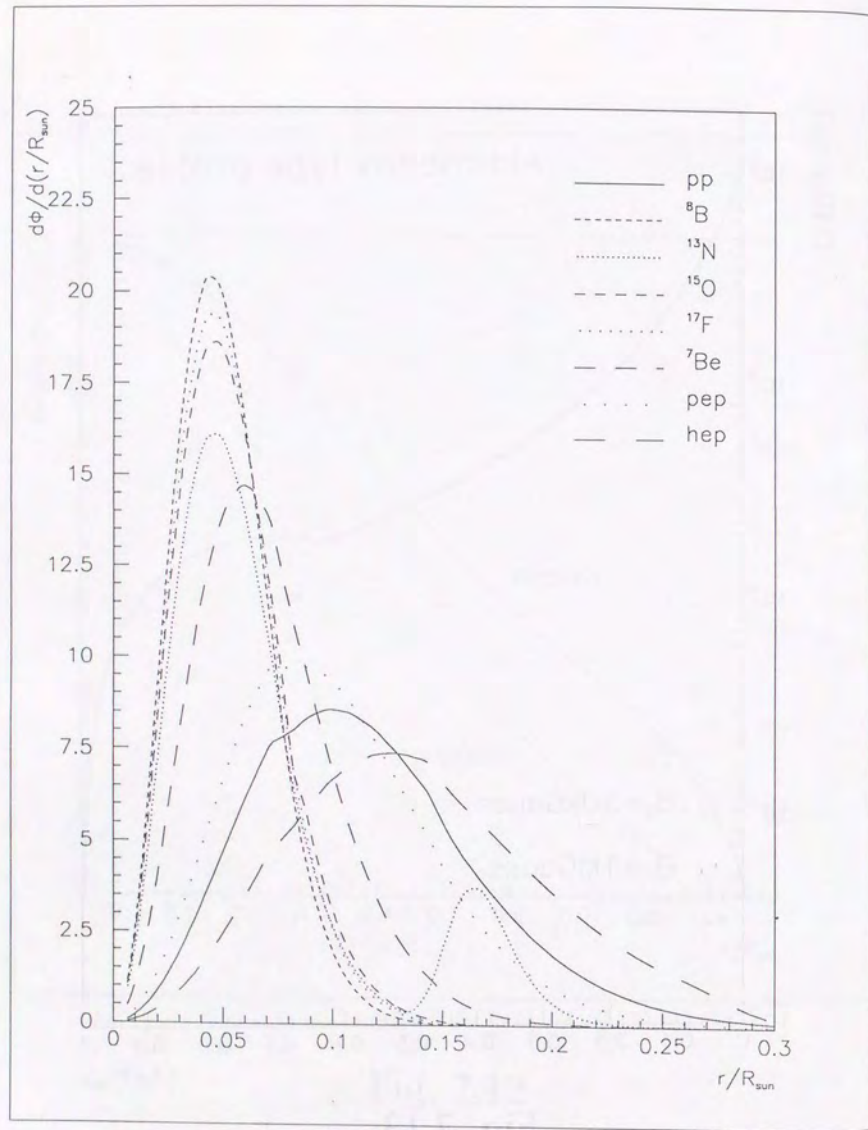


Fig. 7.14

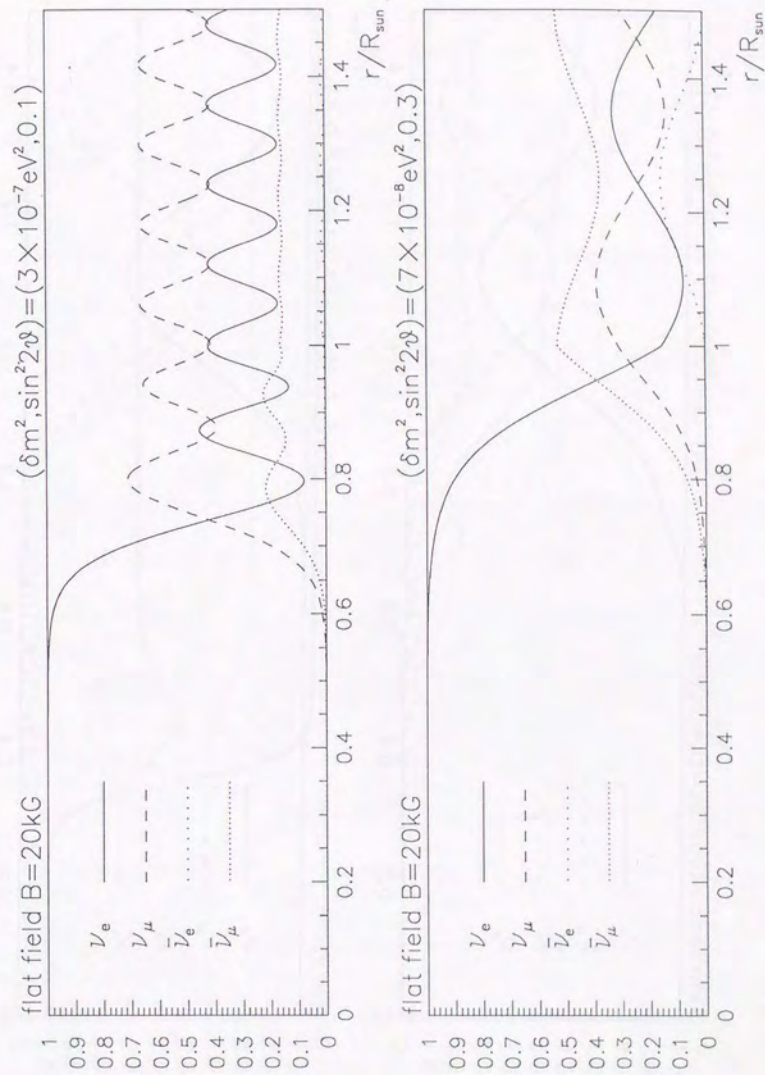


Fig. 7.15



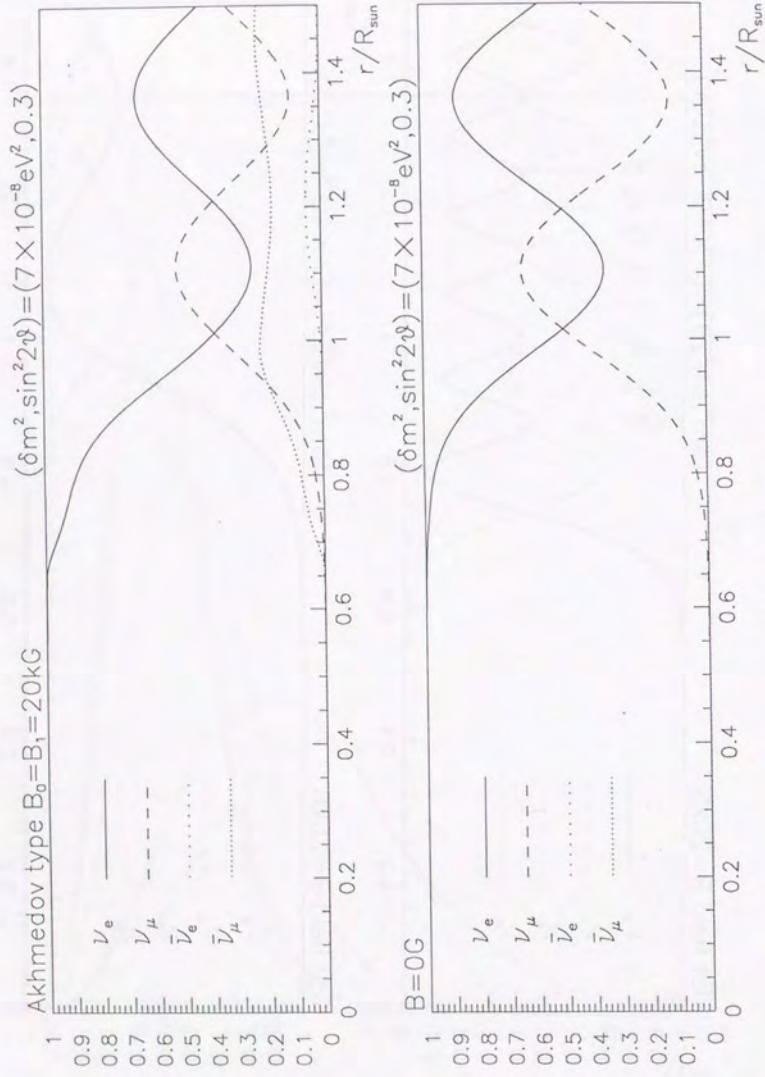


Fig. 7.15 cont.

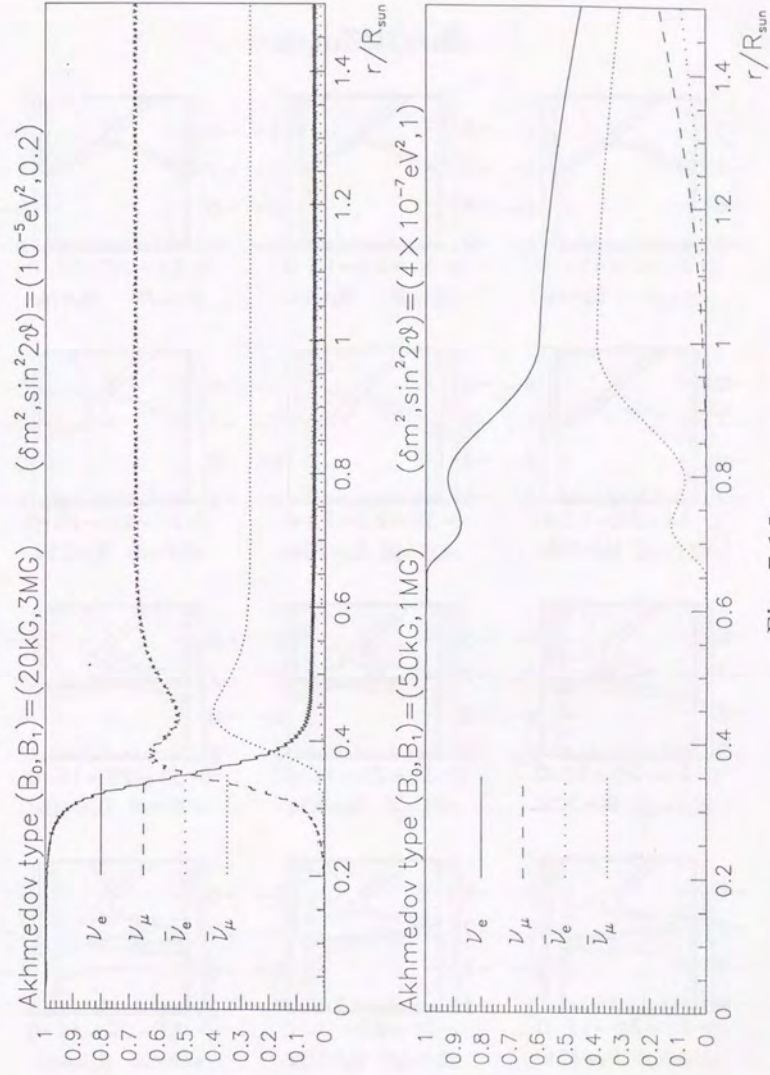


Fig. 7.15 cont.

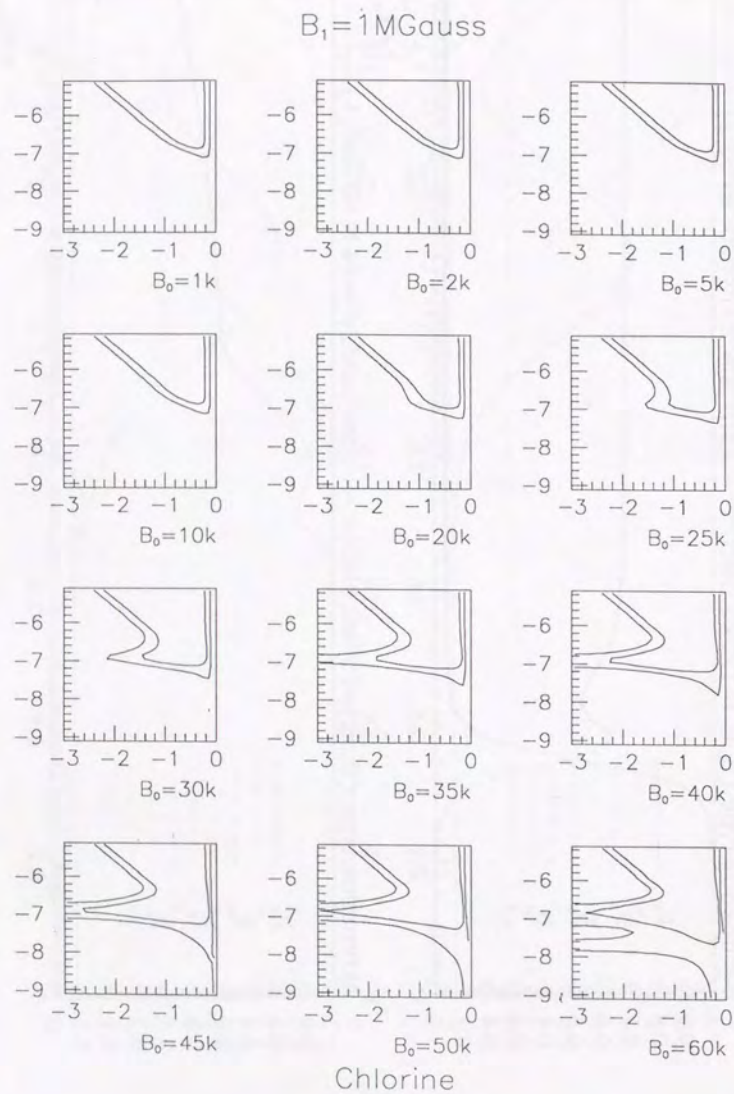


Fig. 7.16

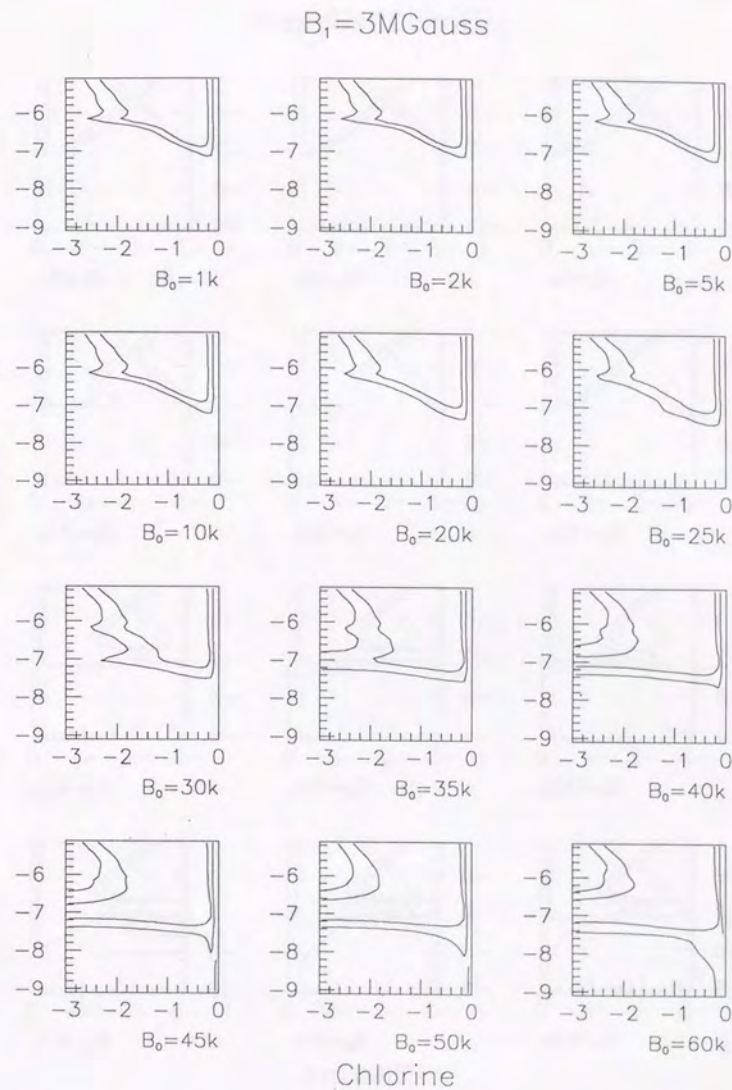
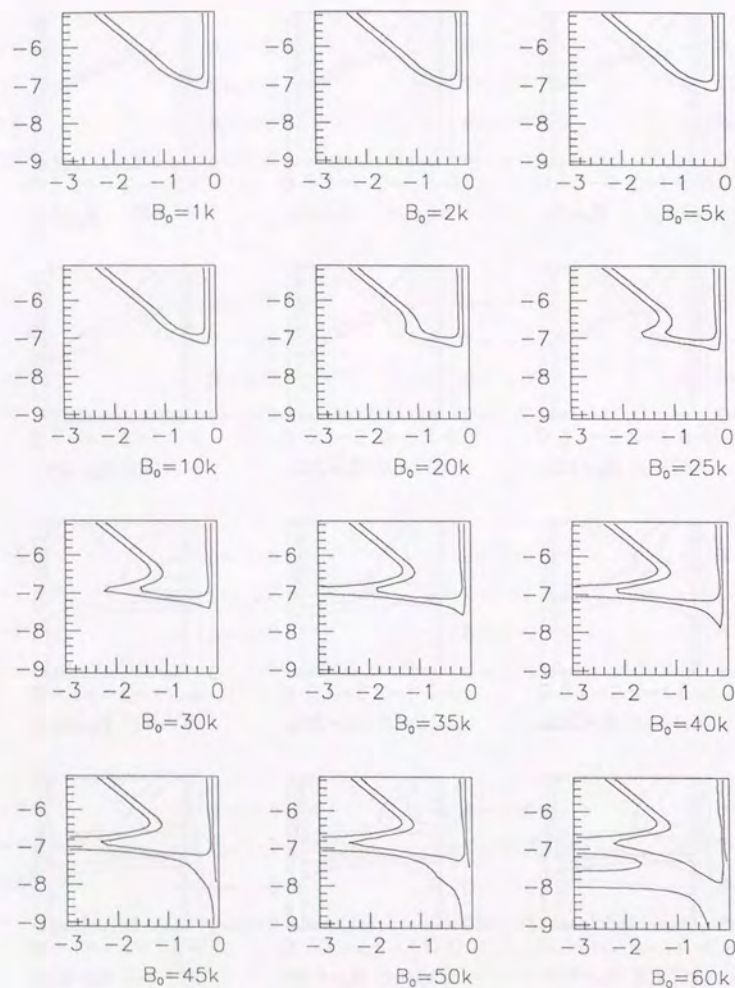


Fig. 7.16 cont.

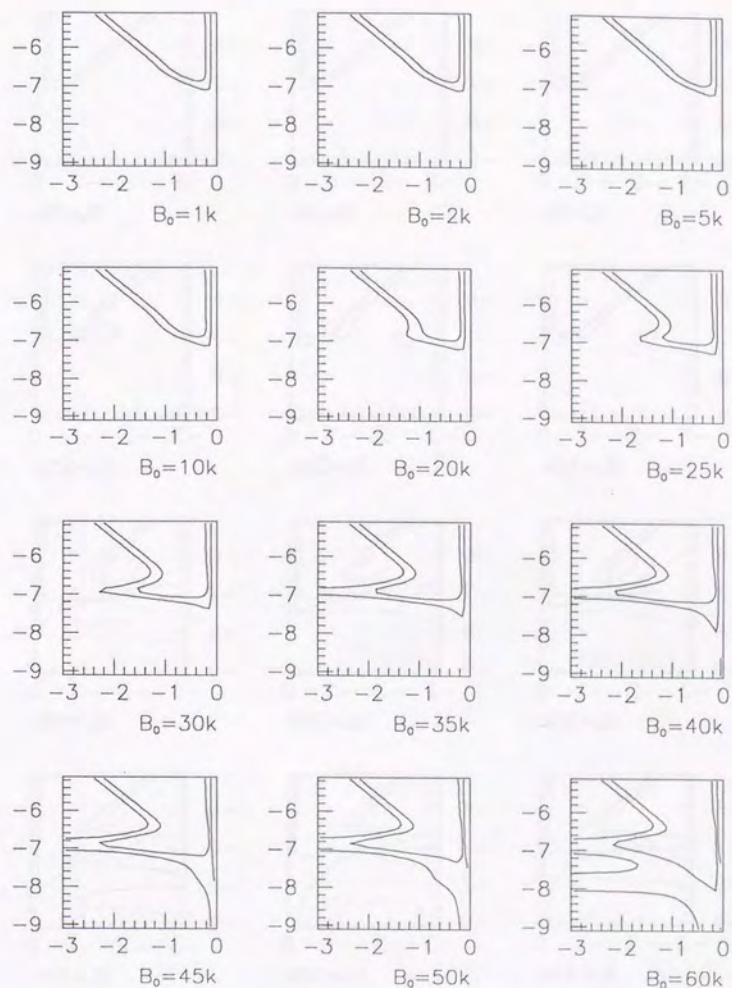
$B_1=300\text{kGauss}$



Chlorine

Fig. 7.16 cont.

$B_1=100\text{kGauss}$



Chlorine

Fig. 7.16 cont.

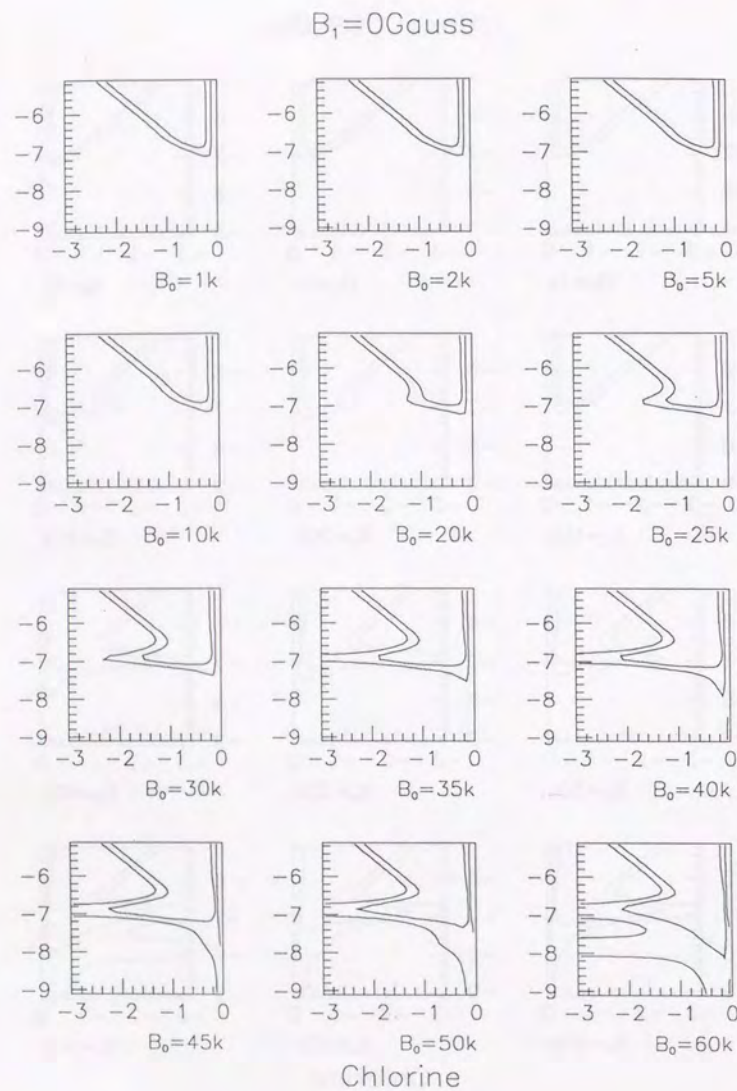


Fig. 7.16 cont.

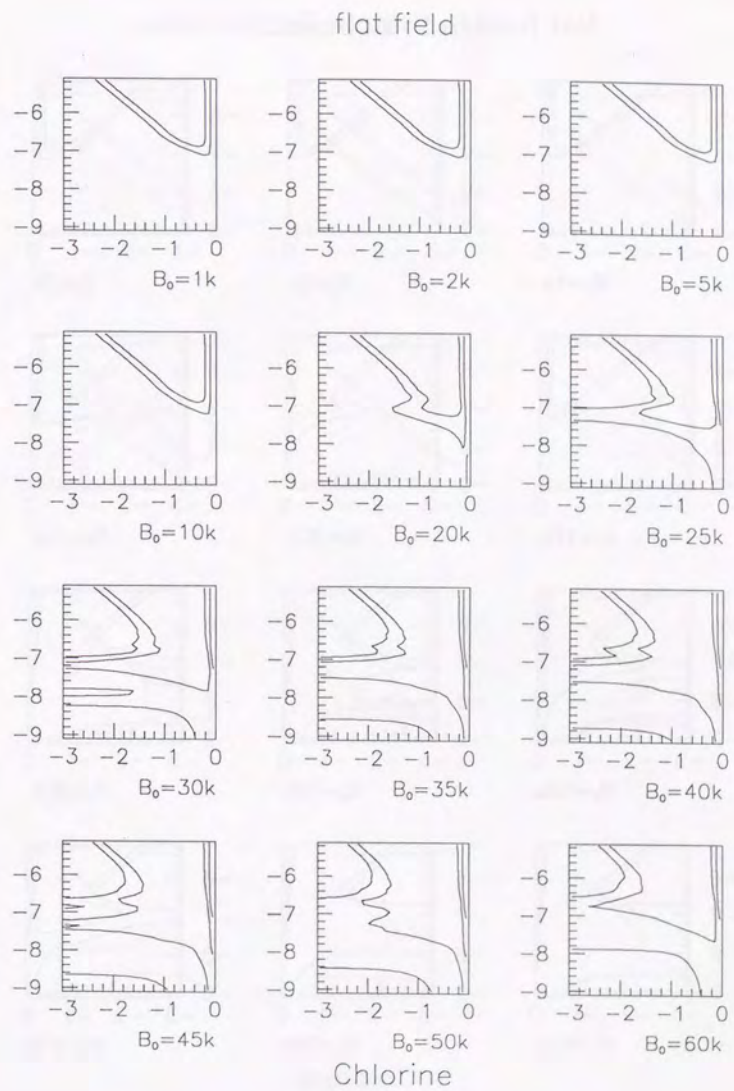


Fig. 7.16 cont.

flat field in the convection zone

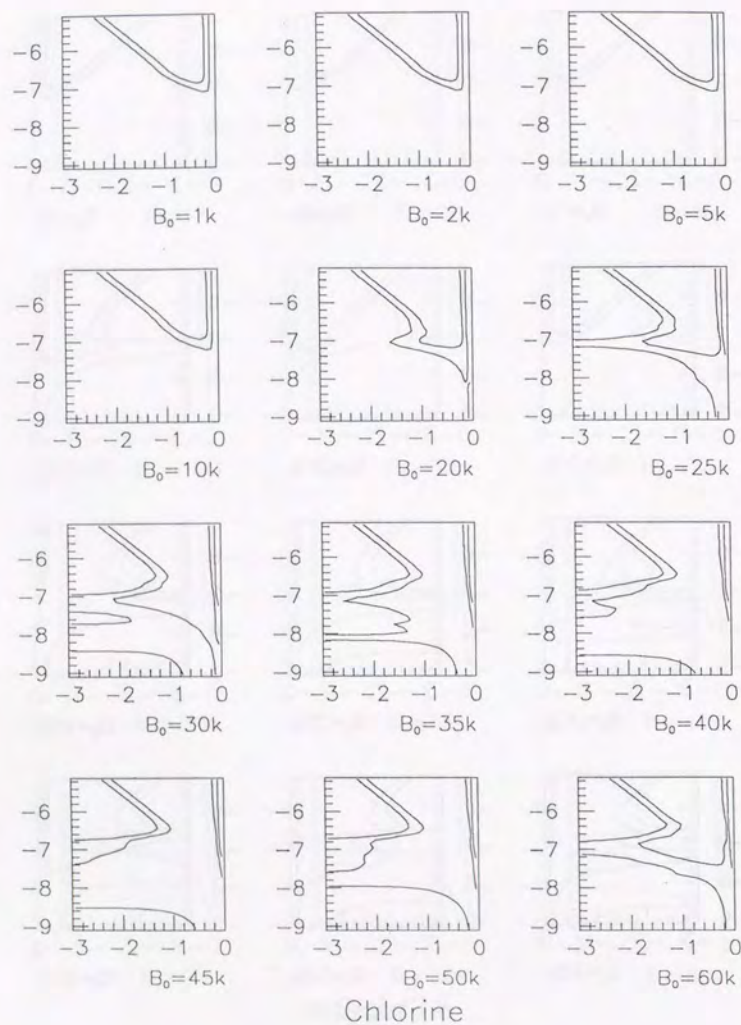


Fig. 7.16 cont.

$B_1 = 1\text{MGauss}$

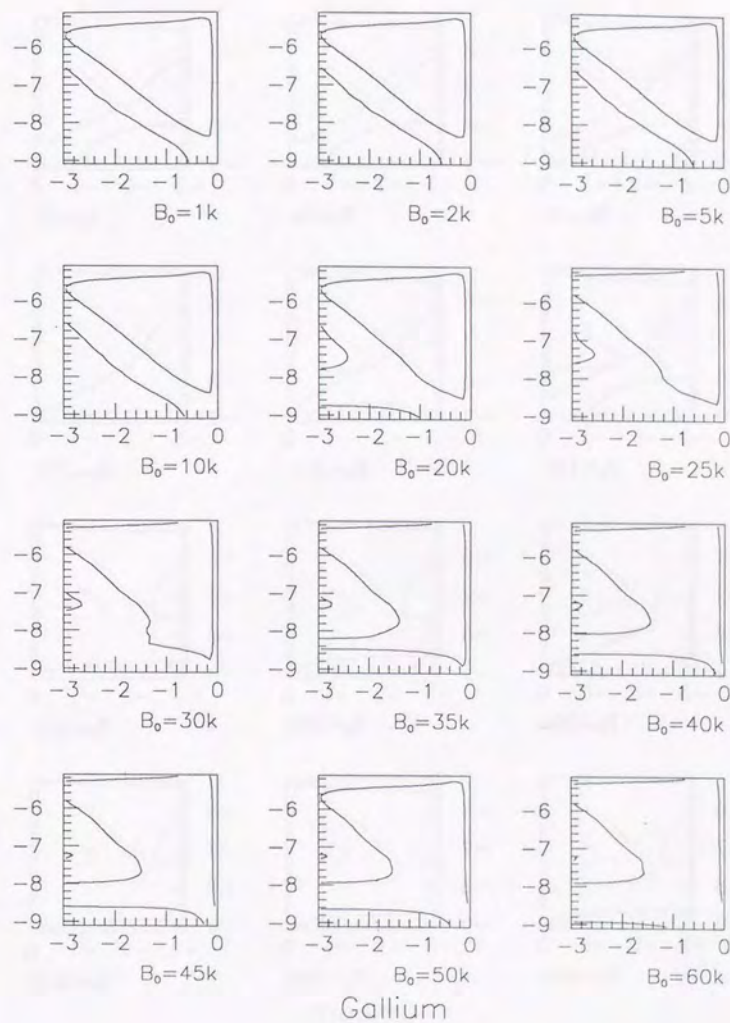
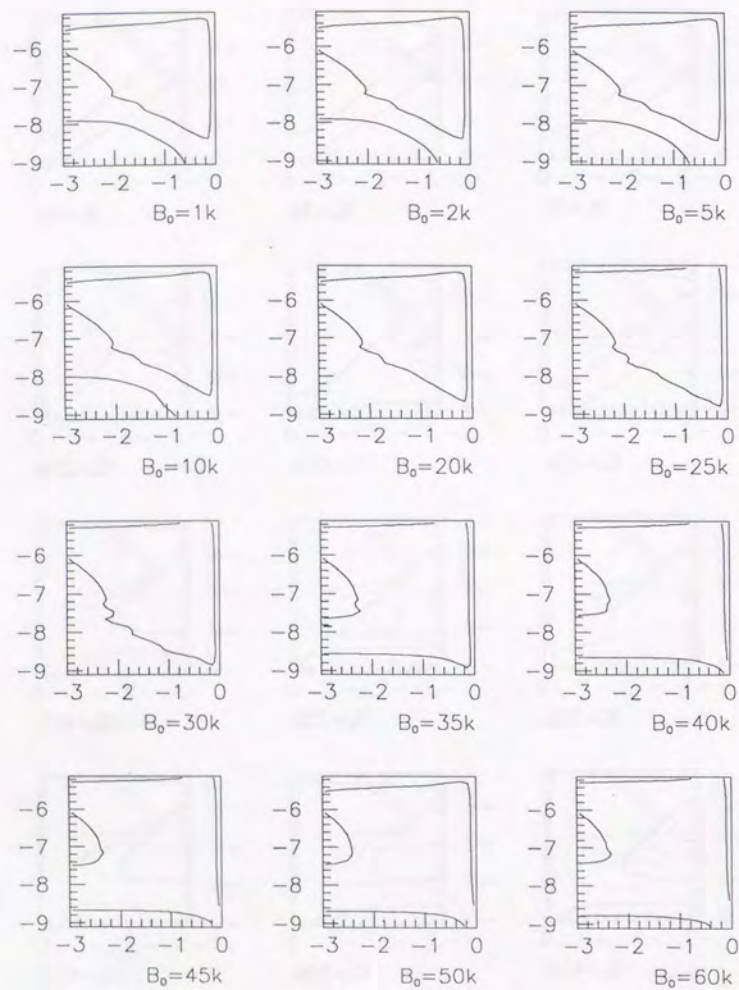


Fig. 7.17

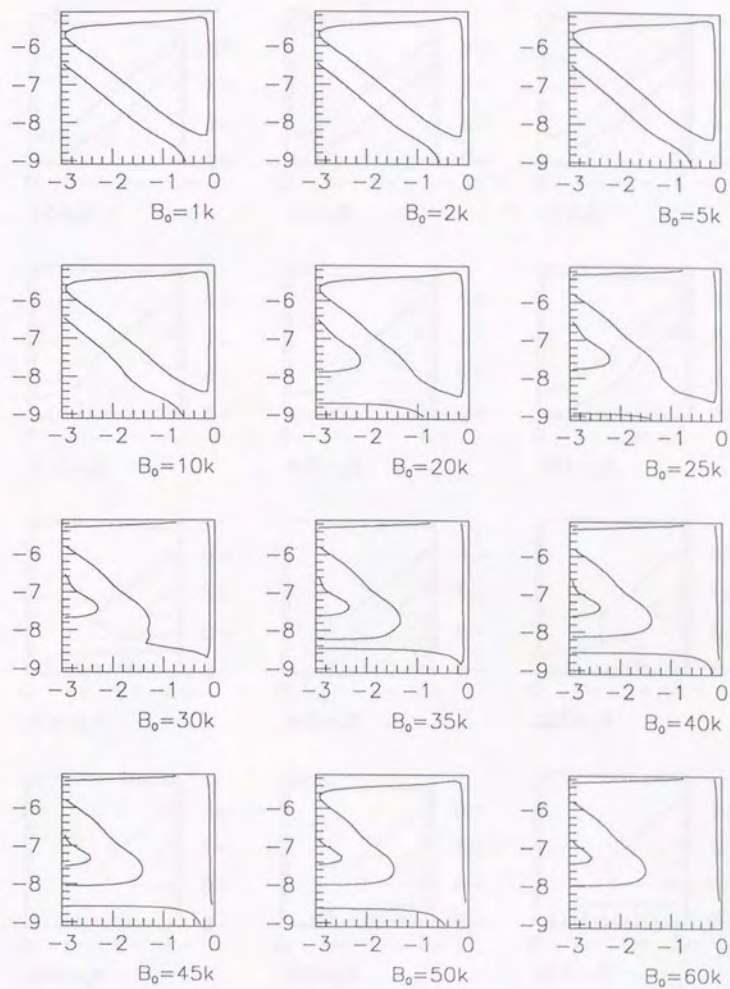
$B_1 = 3\text{MGauss}$



Gallium

Fig. 7.17 cont.

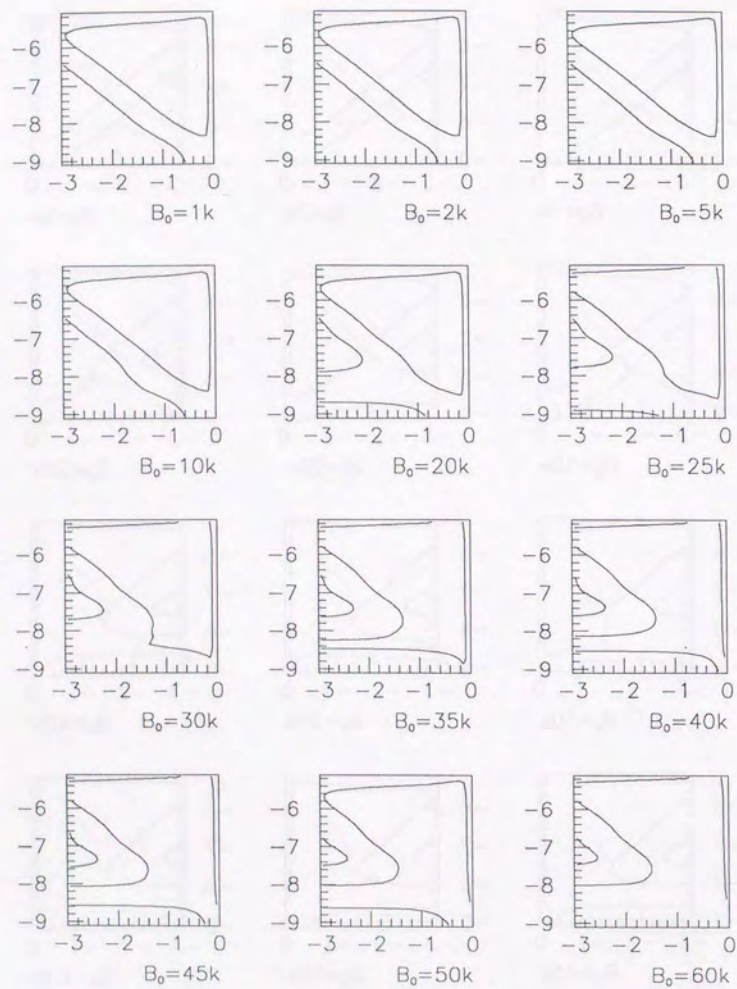
$B_1 = 300\text{kGauss}$



Gallium

Fig. 7.17 cont.

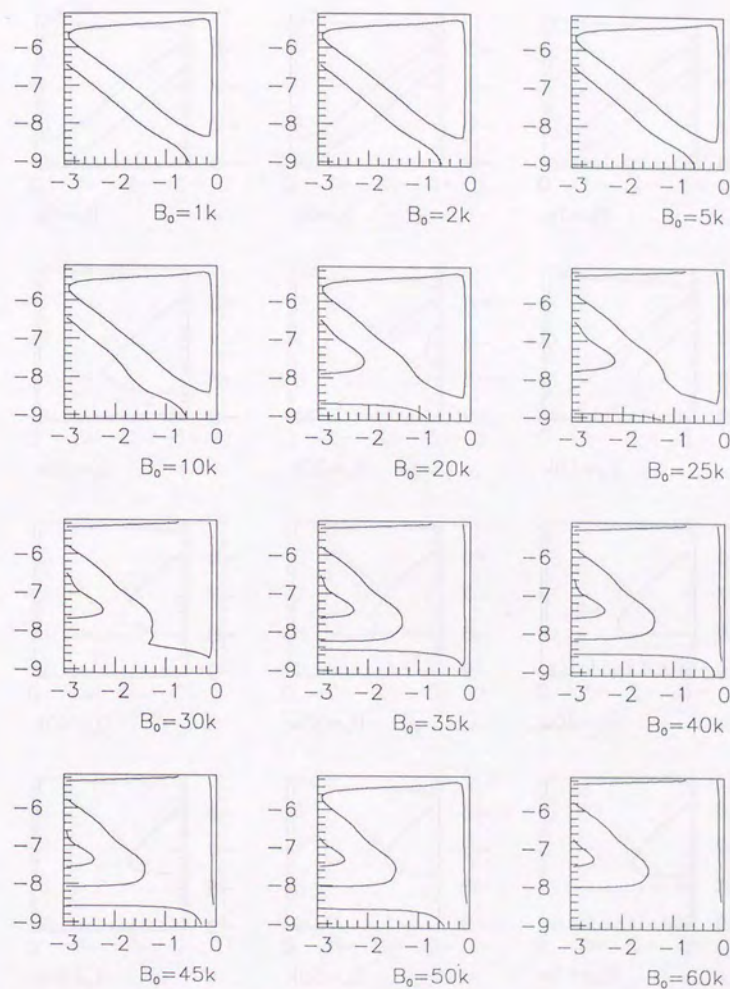
$B_1 = 100\text{kGauss}$



Gallium

Fig. 7.17 cont.

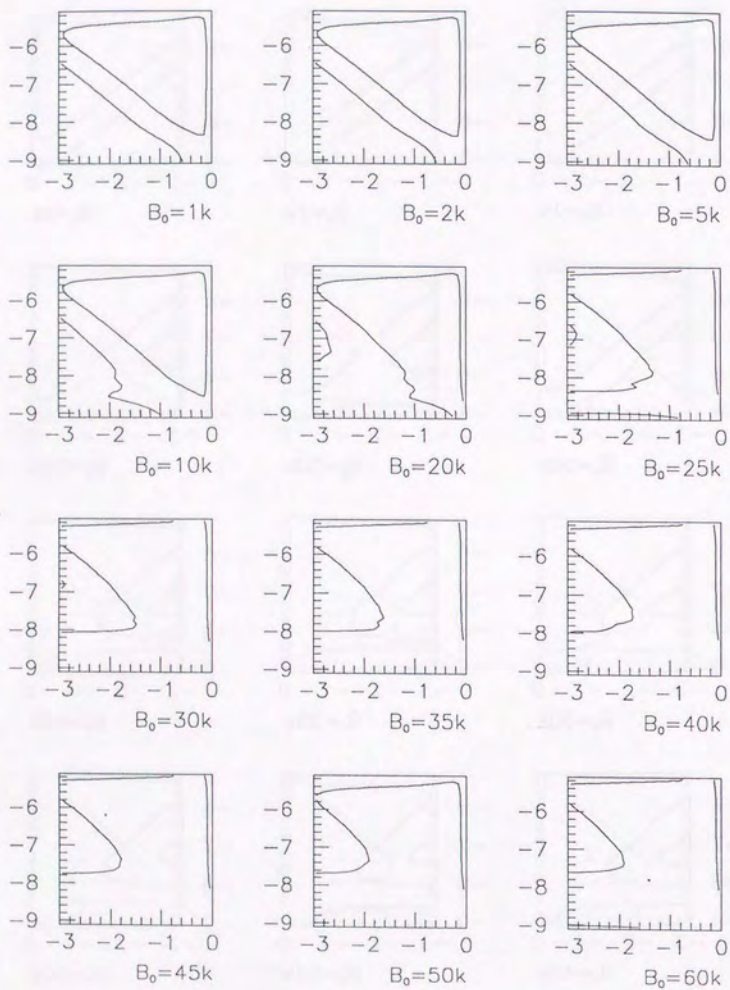
$B_1 = 0\text{Gauss}$



Gallium

Fig. 7.17 cont.

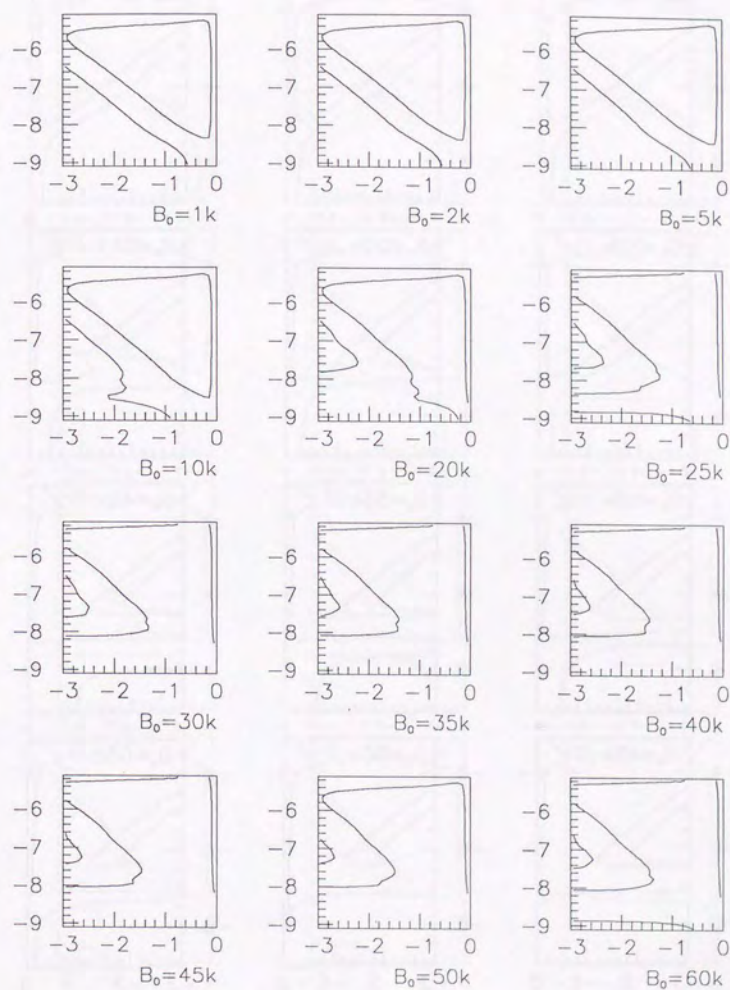
flat field



Gallium

Fig. 7.17 cont.

flat field in the convection zone



Gallium

Fig. 7.17 cont.



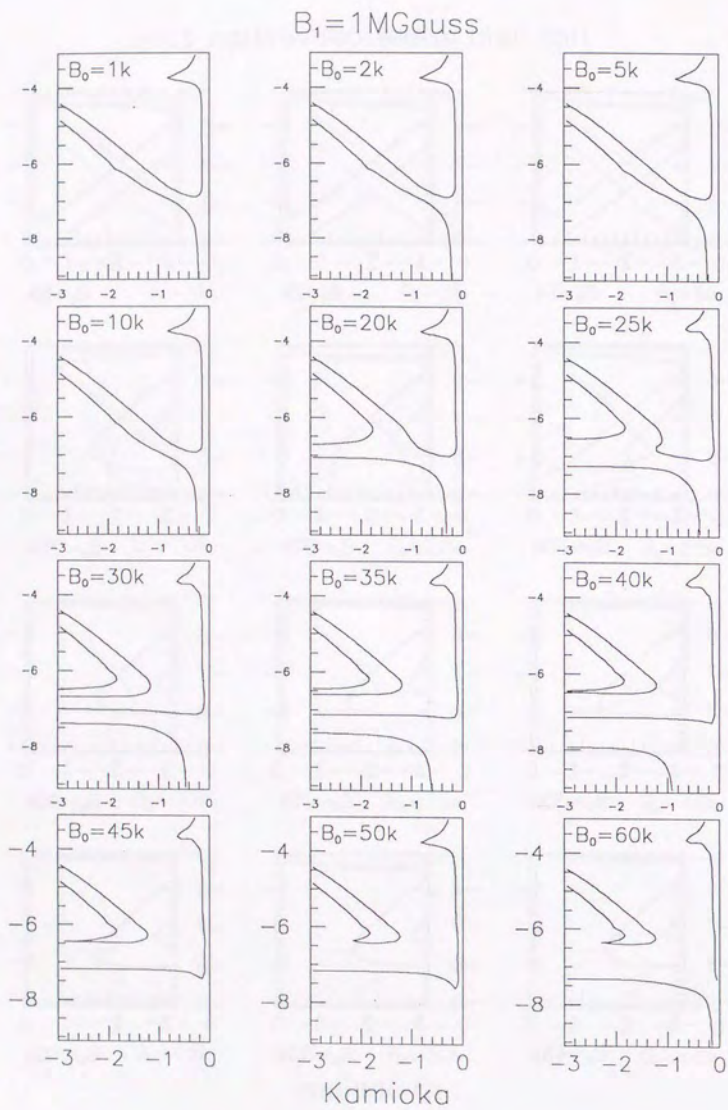


Fig. 7.18

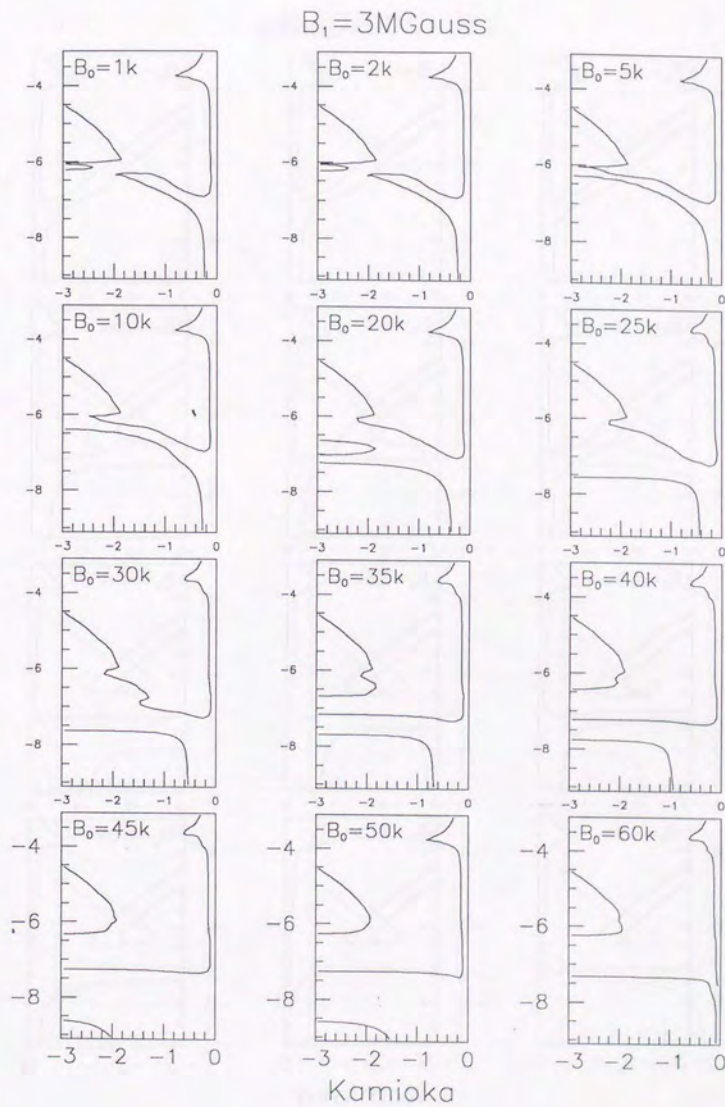


Fig. 7.18 cont.

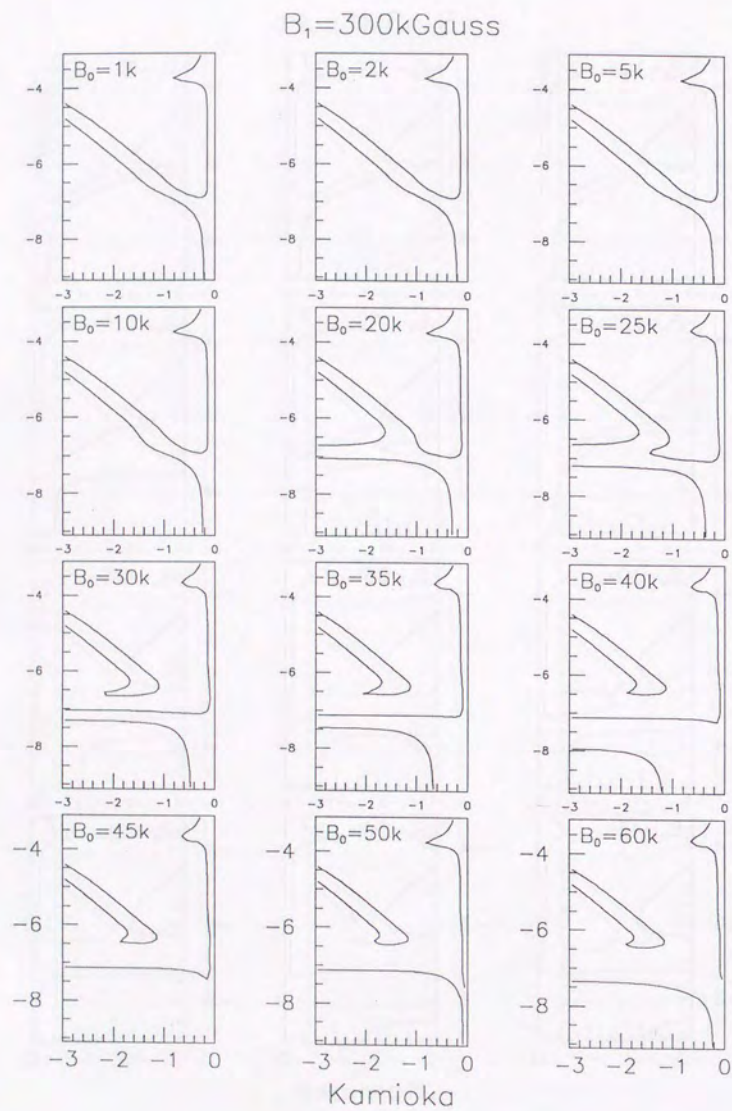


Fig. 7.18 cont.

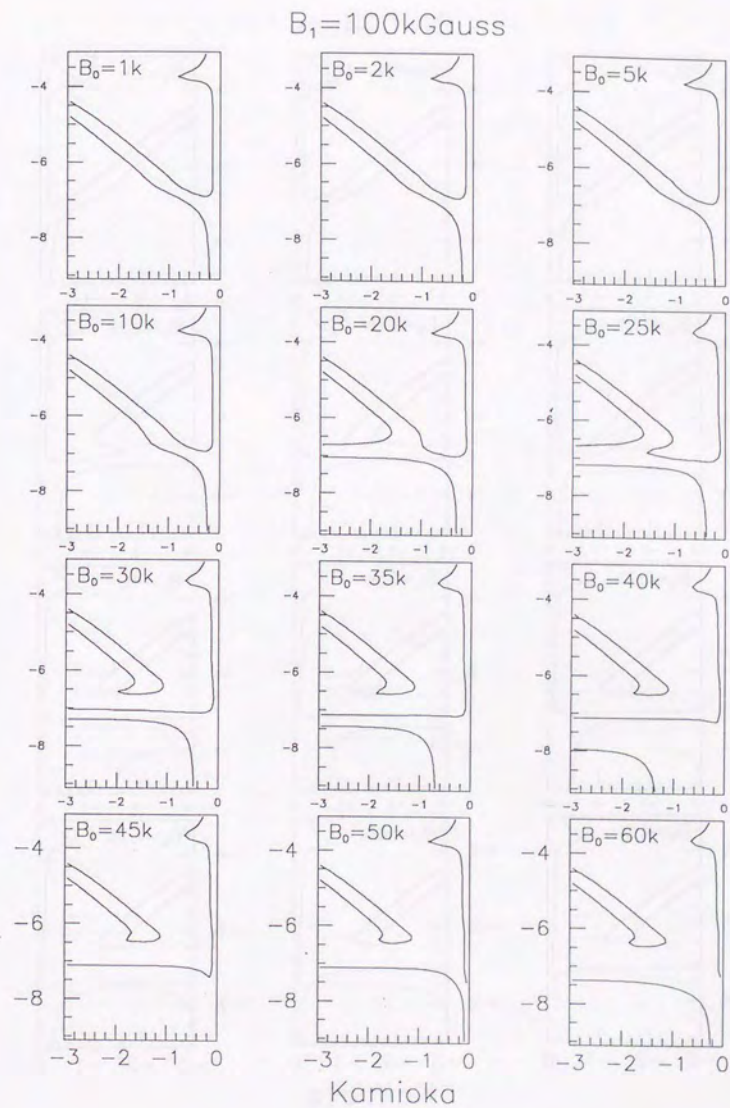


Fig. 7.18 cont.

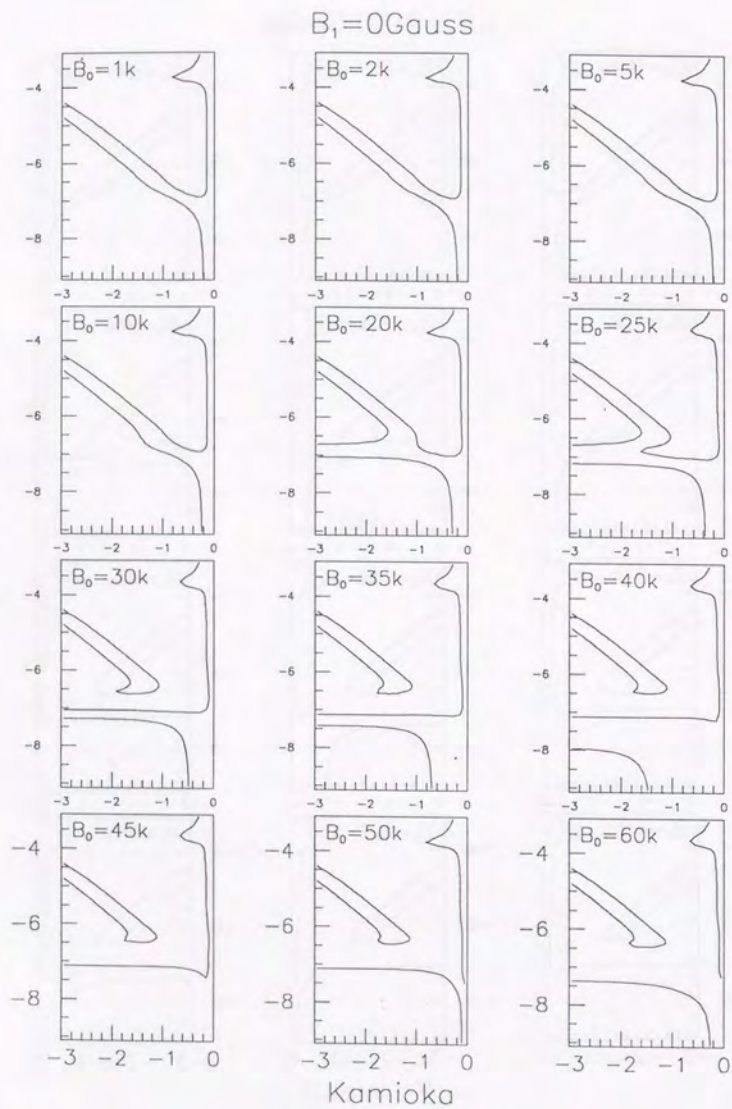


Fig. 7.18 cont.

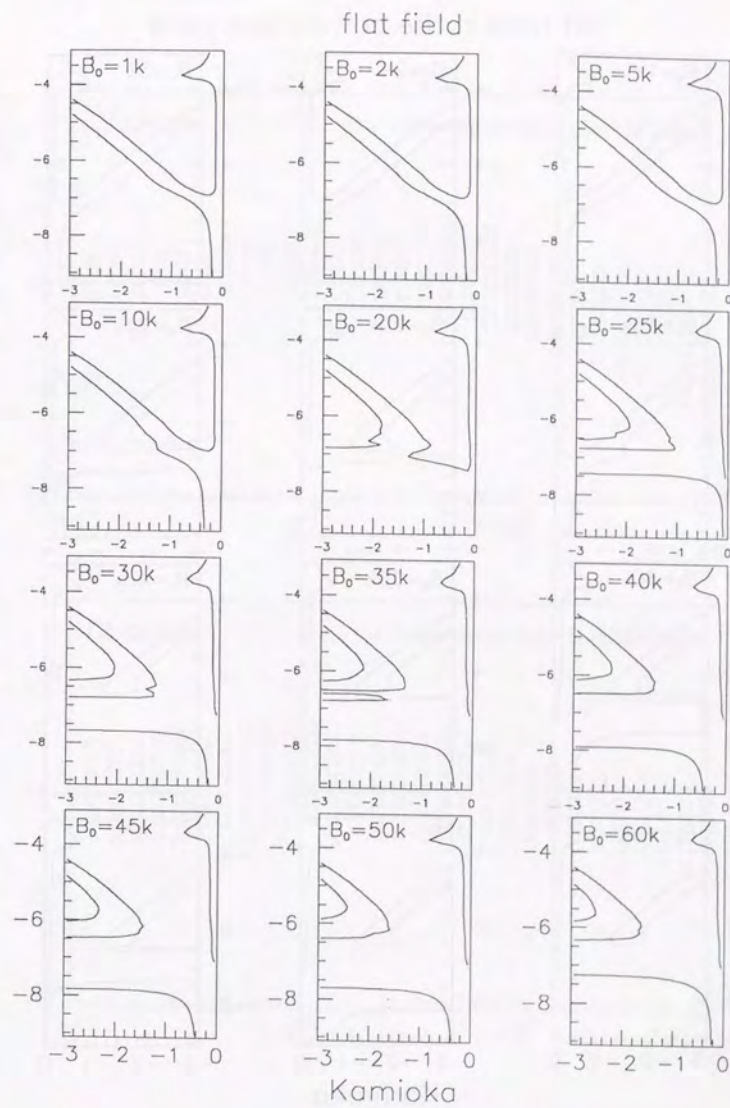
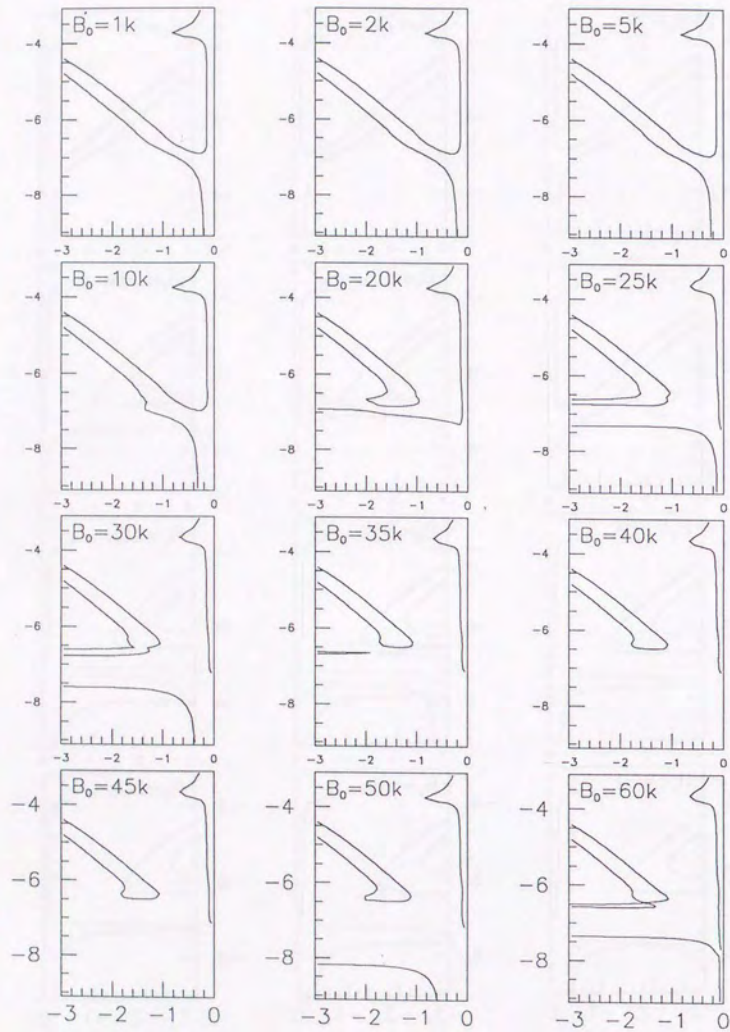


Fig. 7.18 cont.

flat field in the convection zone



Kamioka

Fig. 7.18 cont.

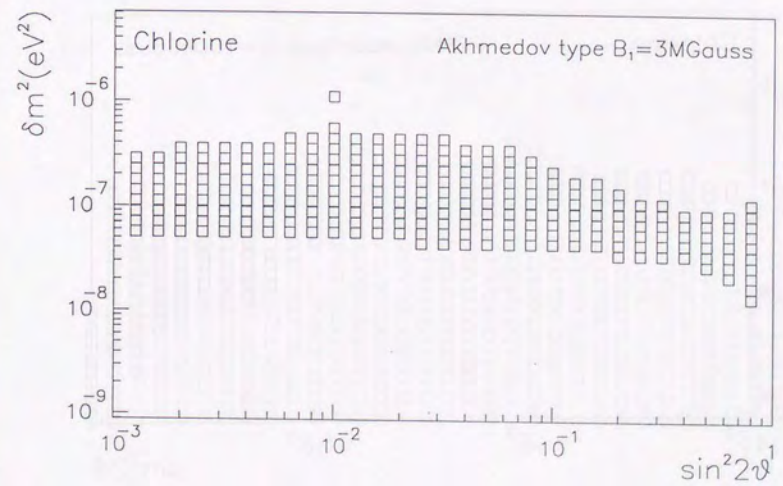
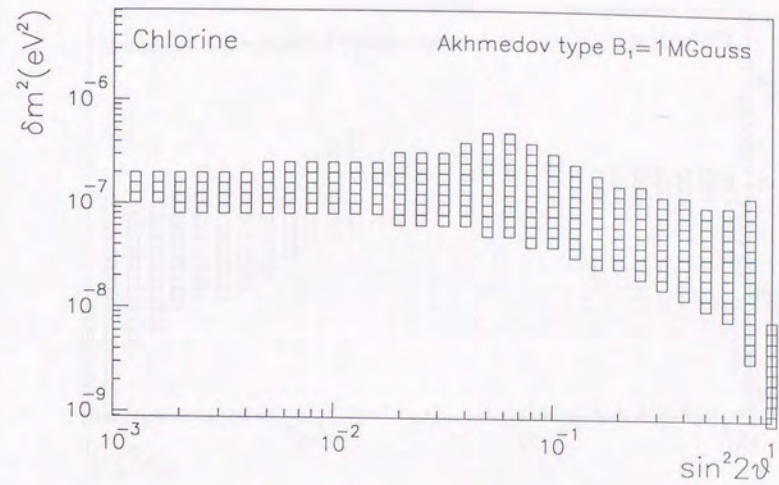


Fig. 7.19

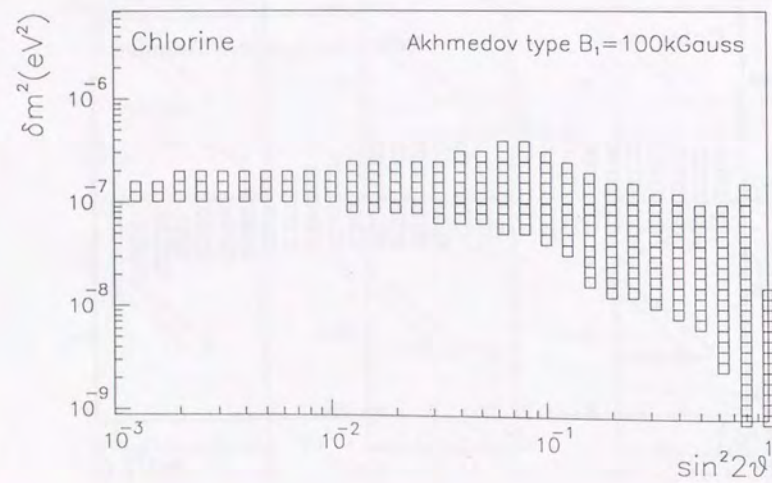
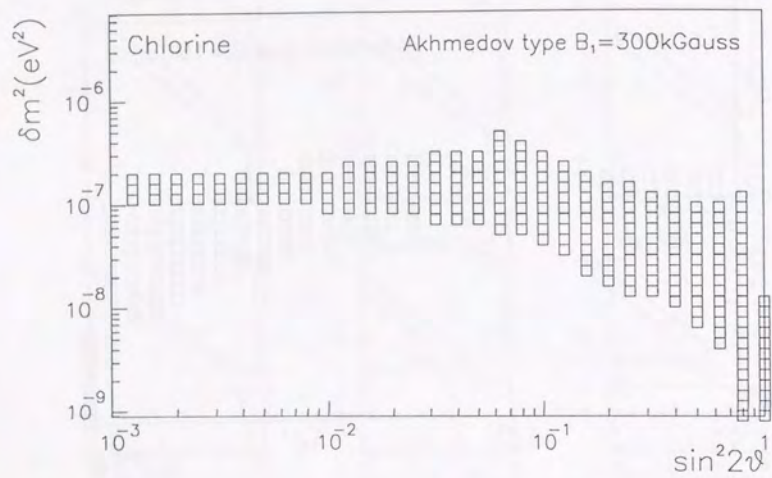


Fig. 7.19 cont.

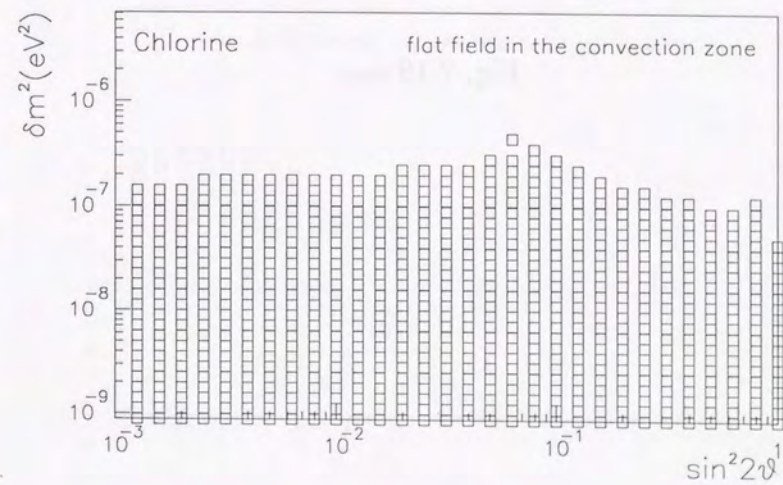
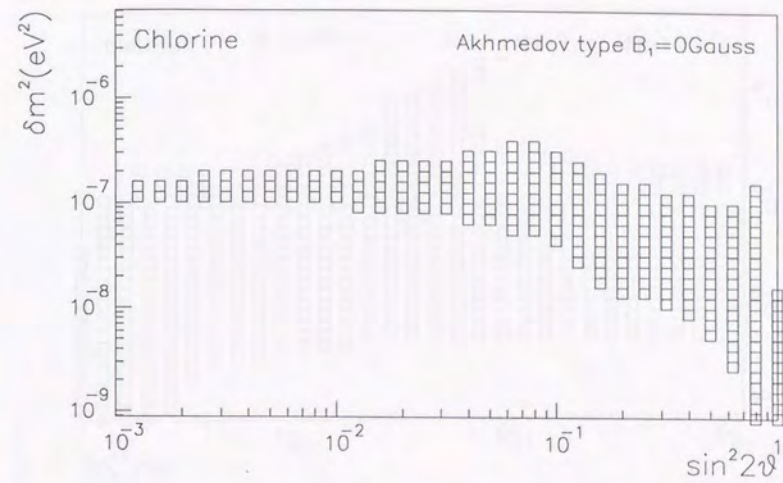


Fig. 7.19 cont.

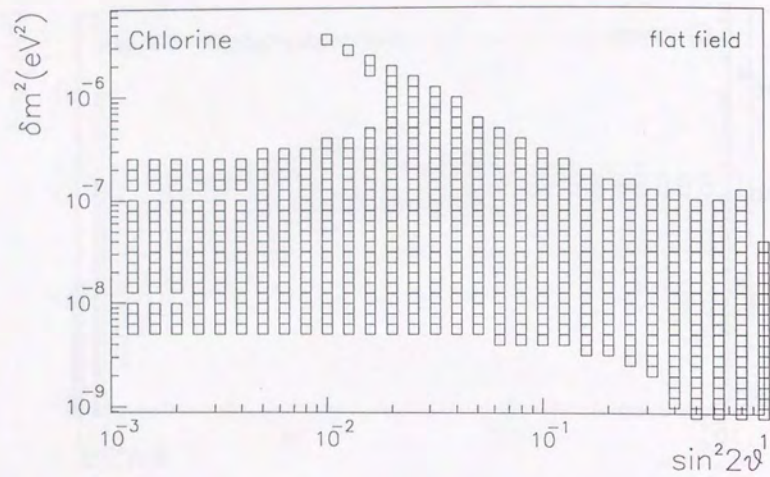


Fig. 7.19 cont.

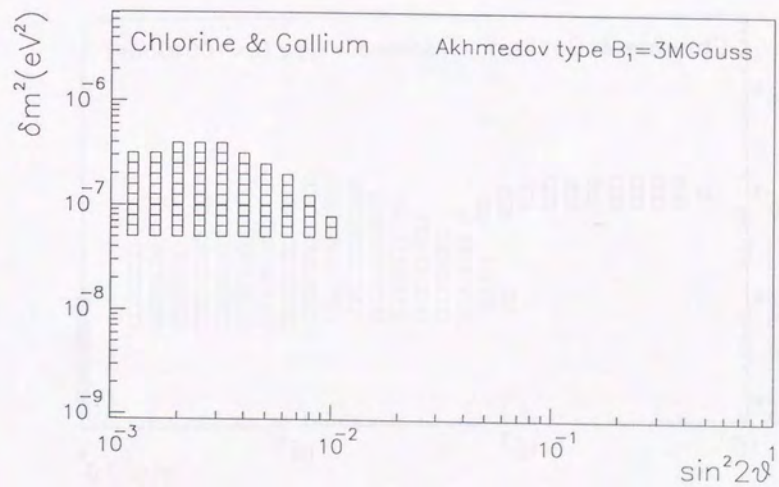
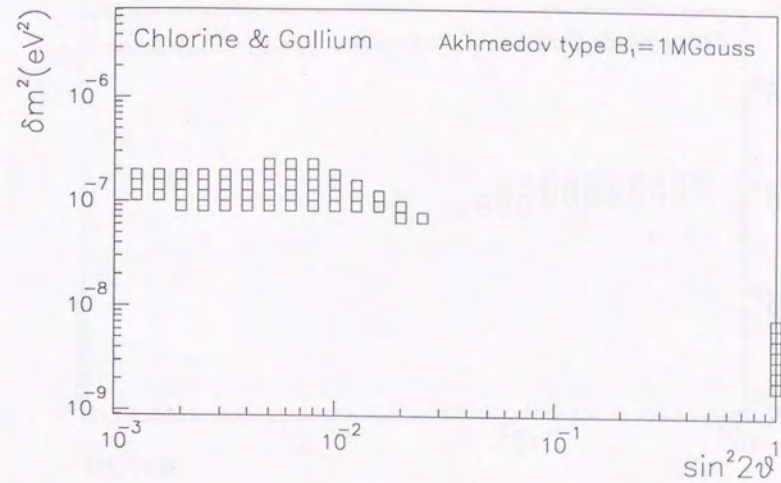


Fig. 7.20

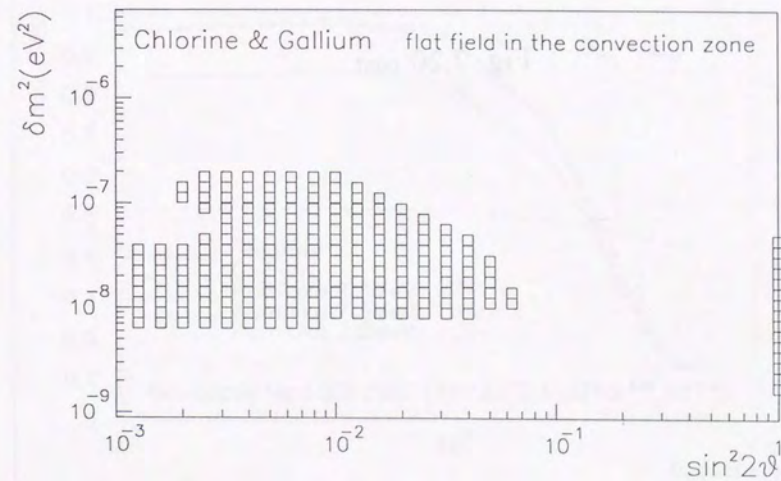
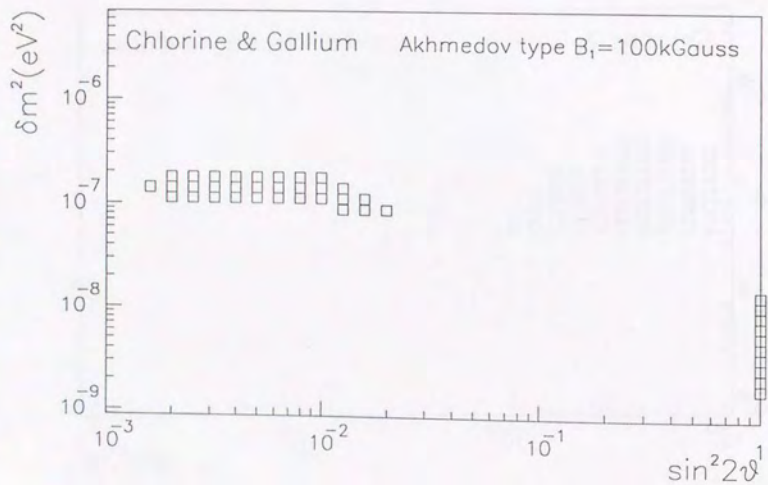
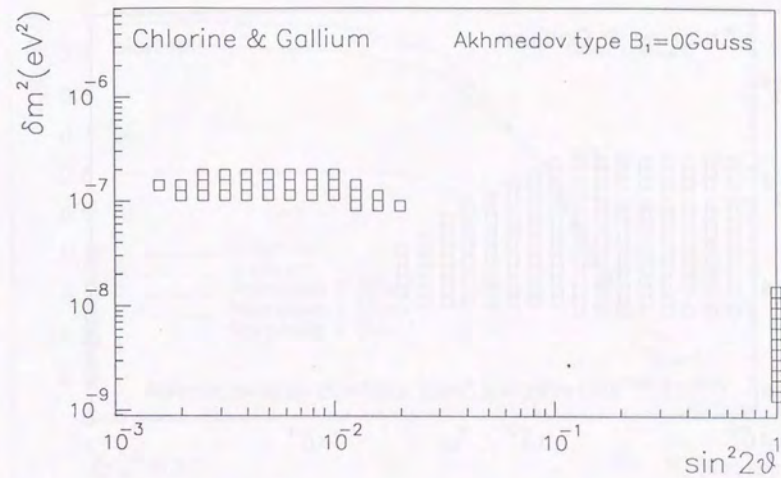
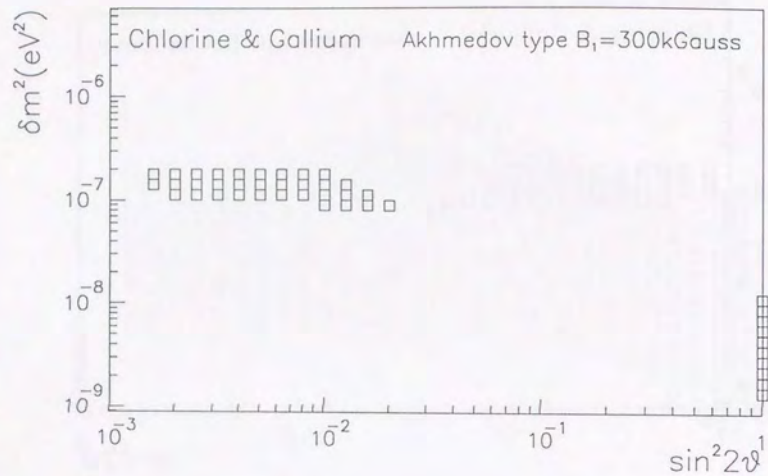


Fig. 7.20 cont.

Fig. 7.20 cont.

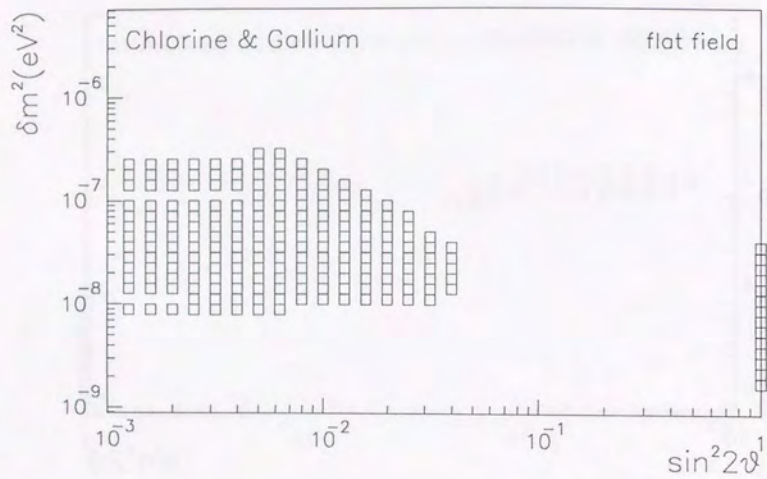


Fig. 7.20 cont.

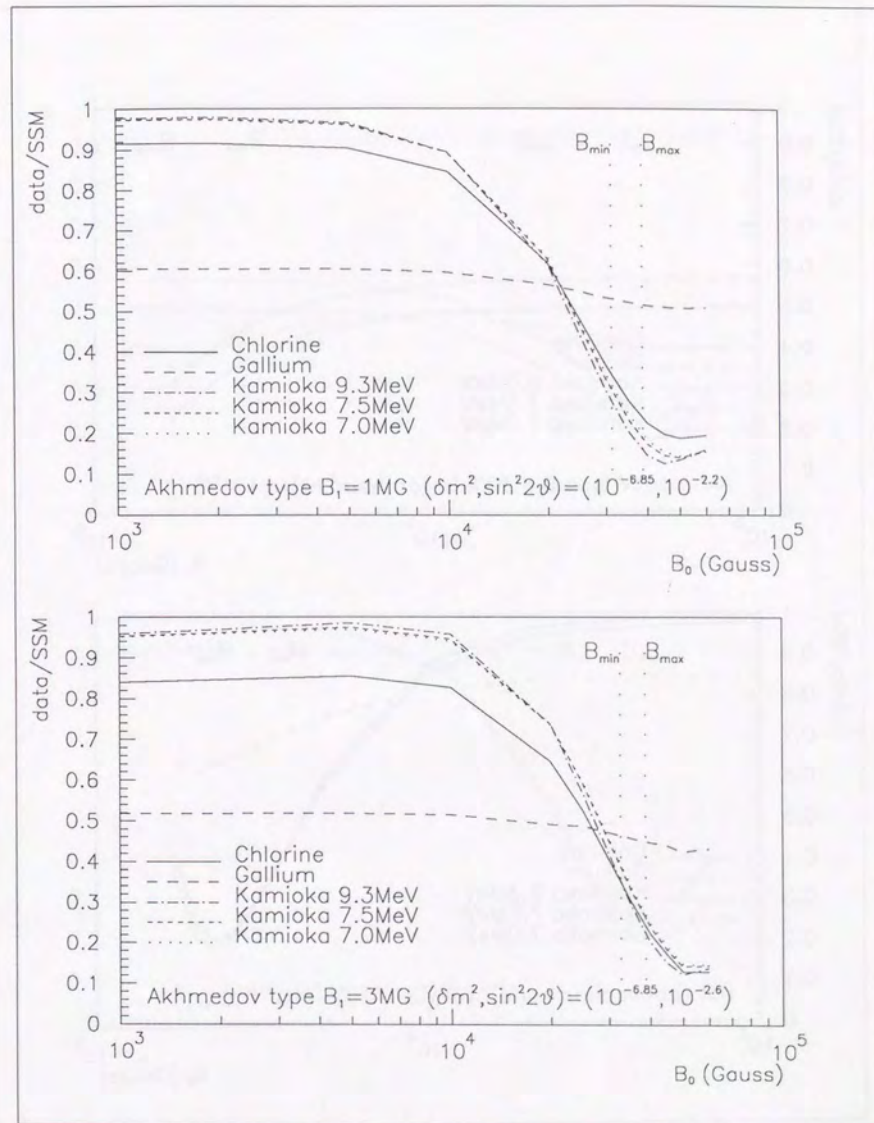


Fig. 7.21



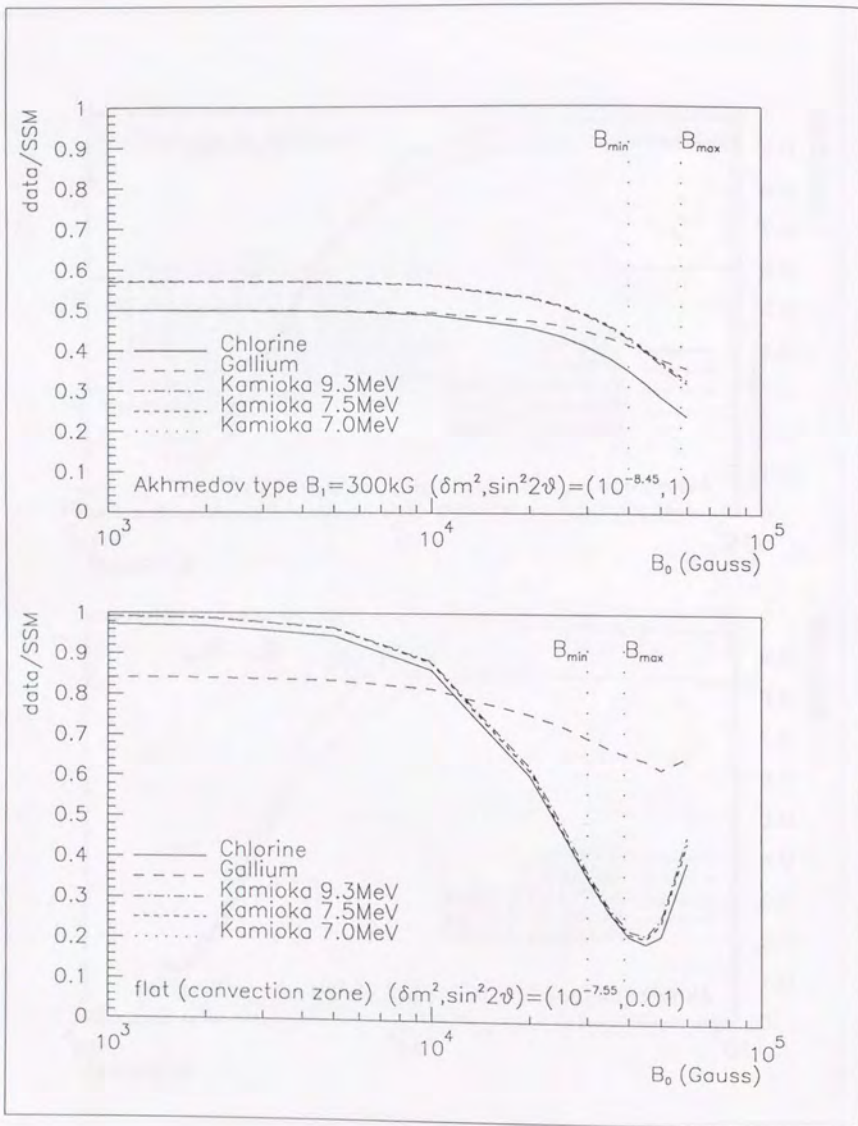


Fig. 7.21 cont.

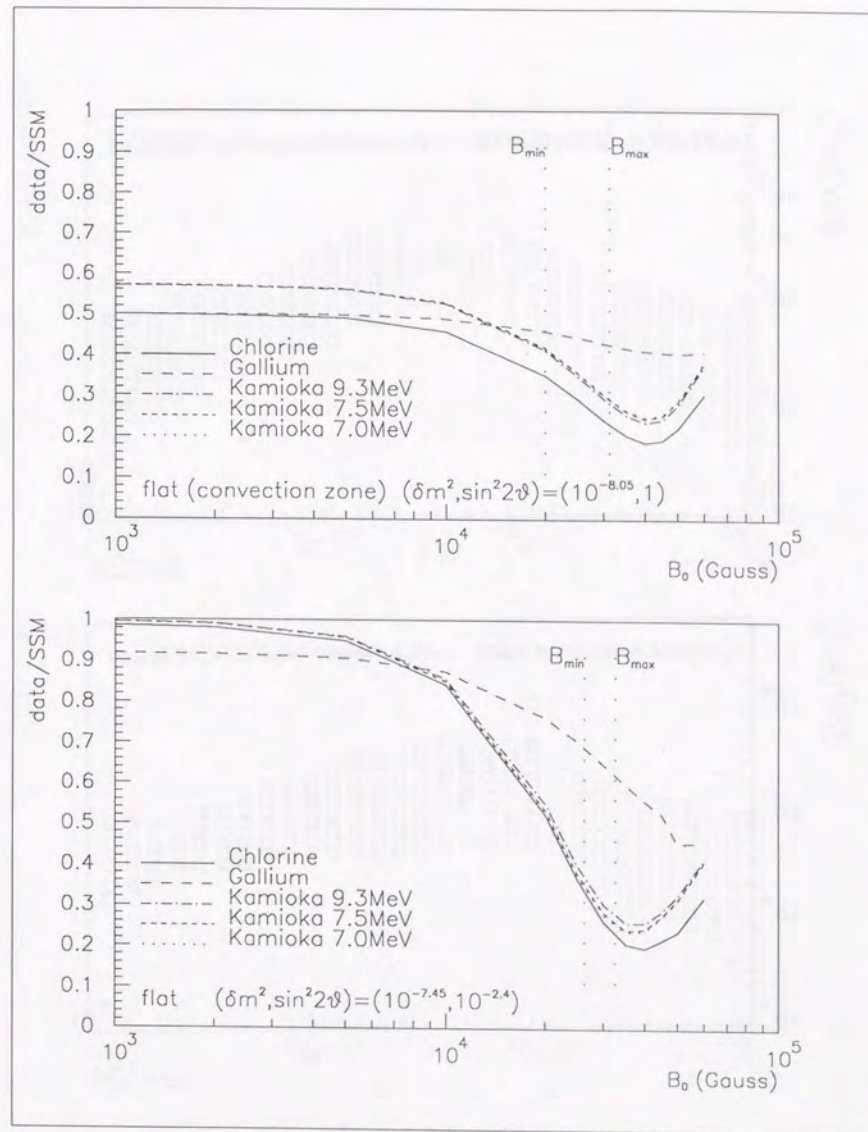


Fig. 7.21 cont.

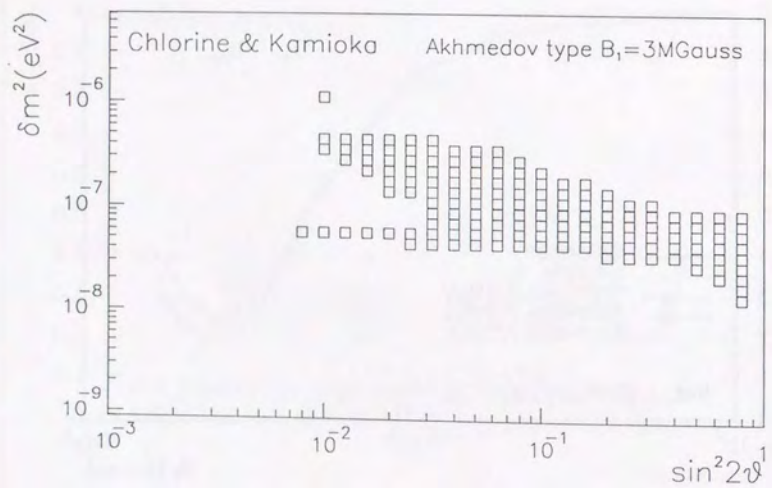
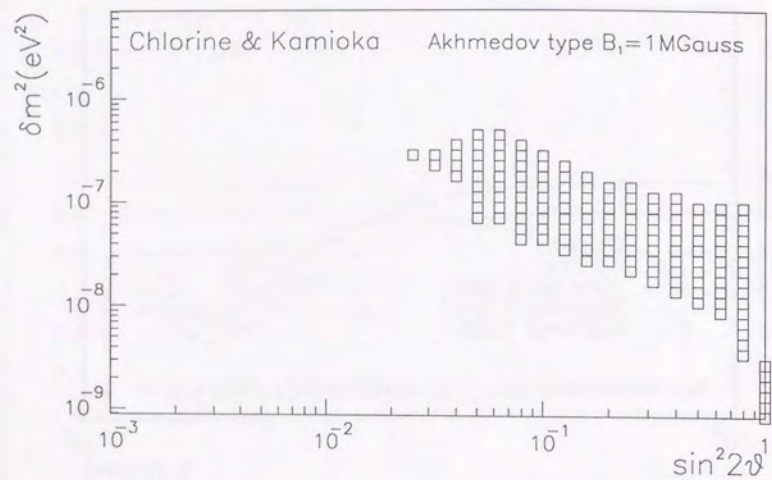


Fig. 7.22

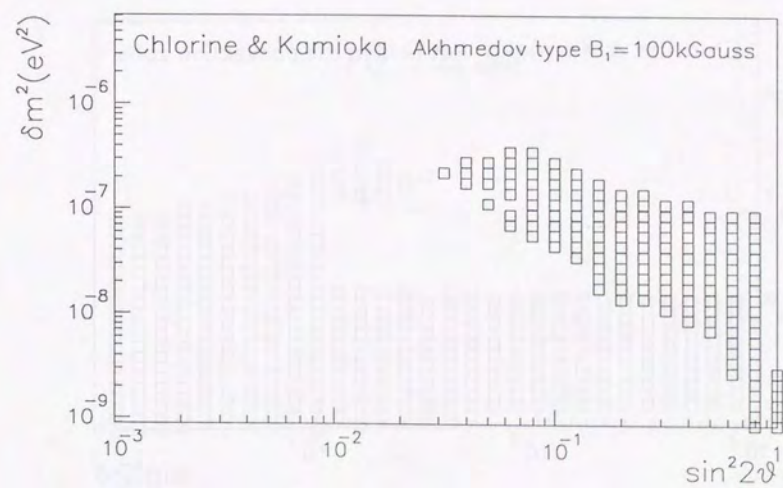
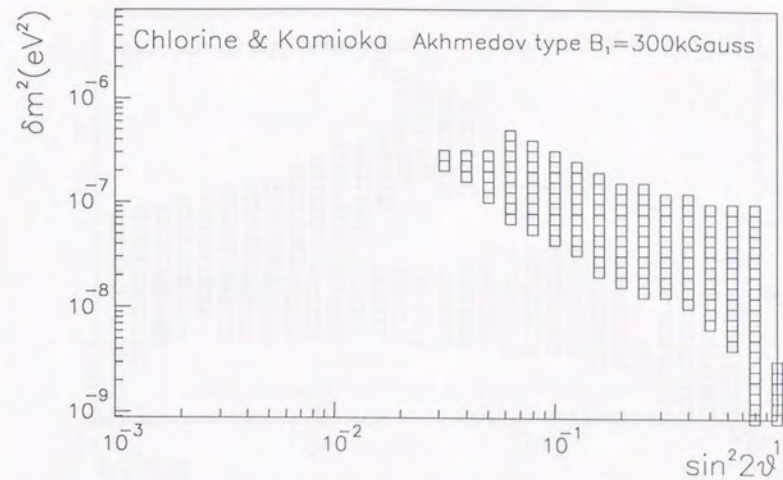


Fig. 7.22 cont.

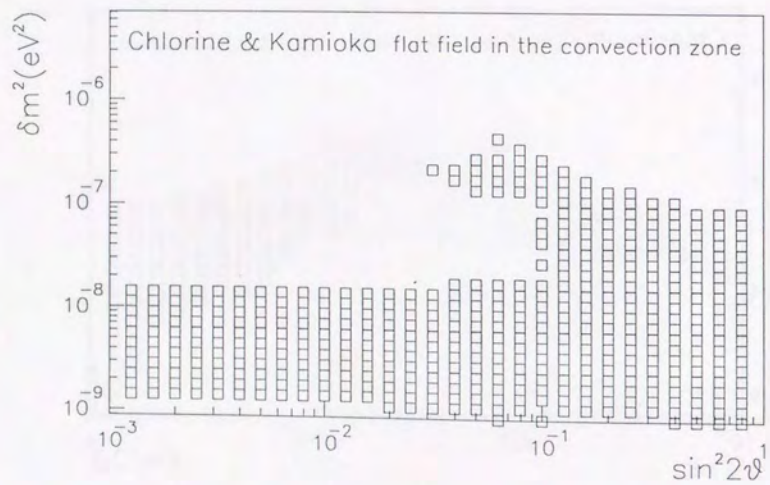
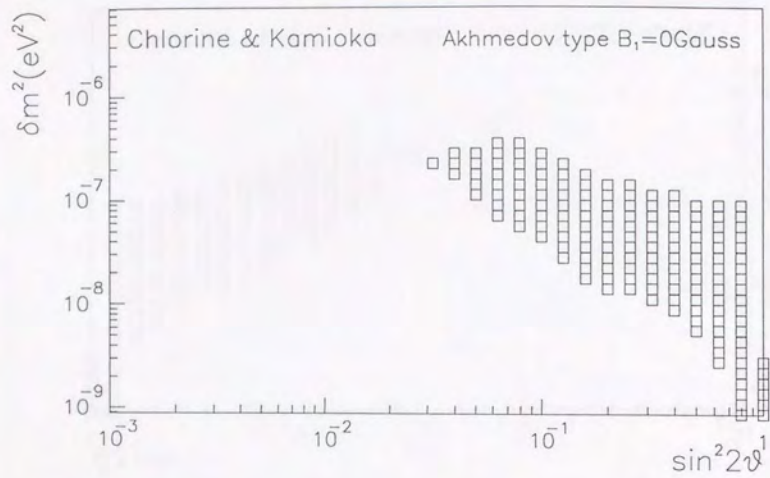


Fig. 7.22 cont.

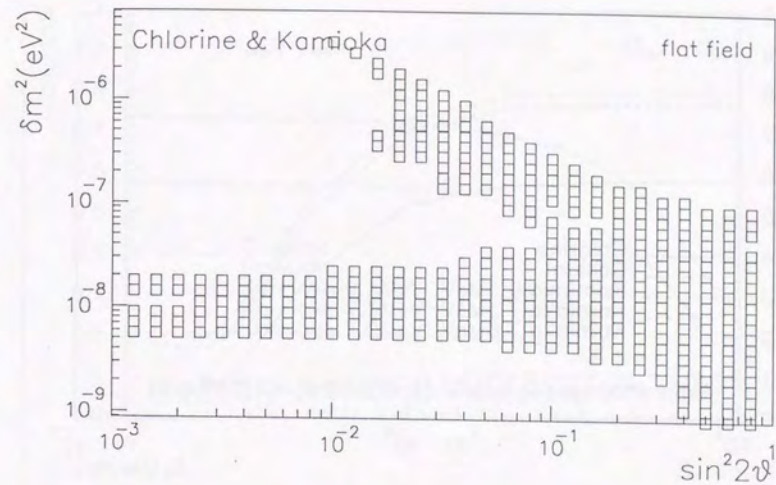


Fig. 7.22 cont.

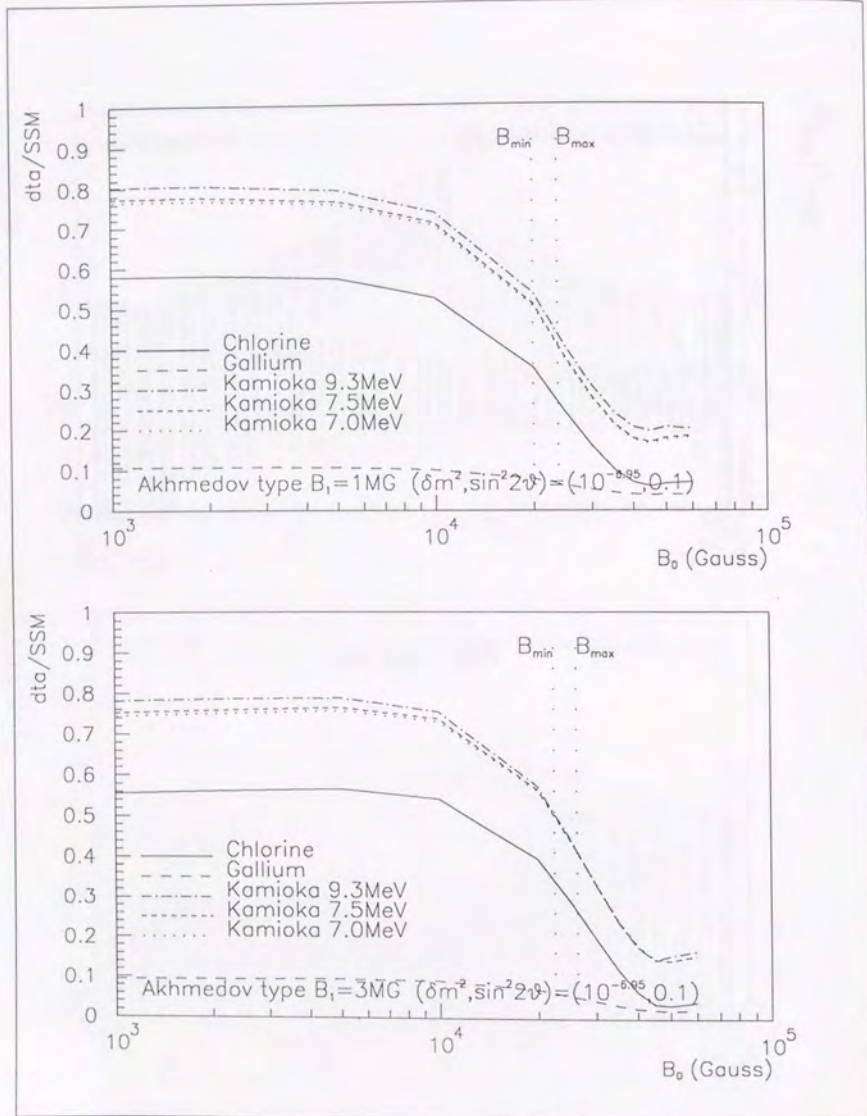


Fig. 7.23

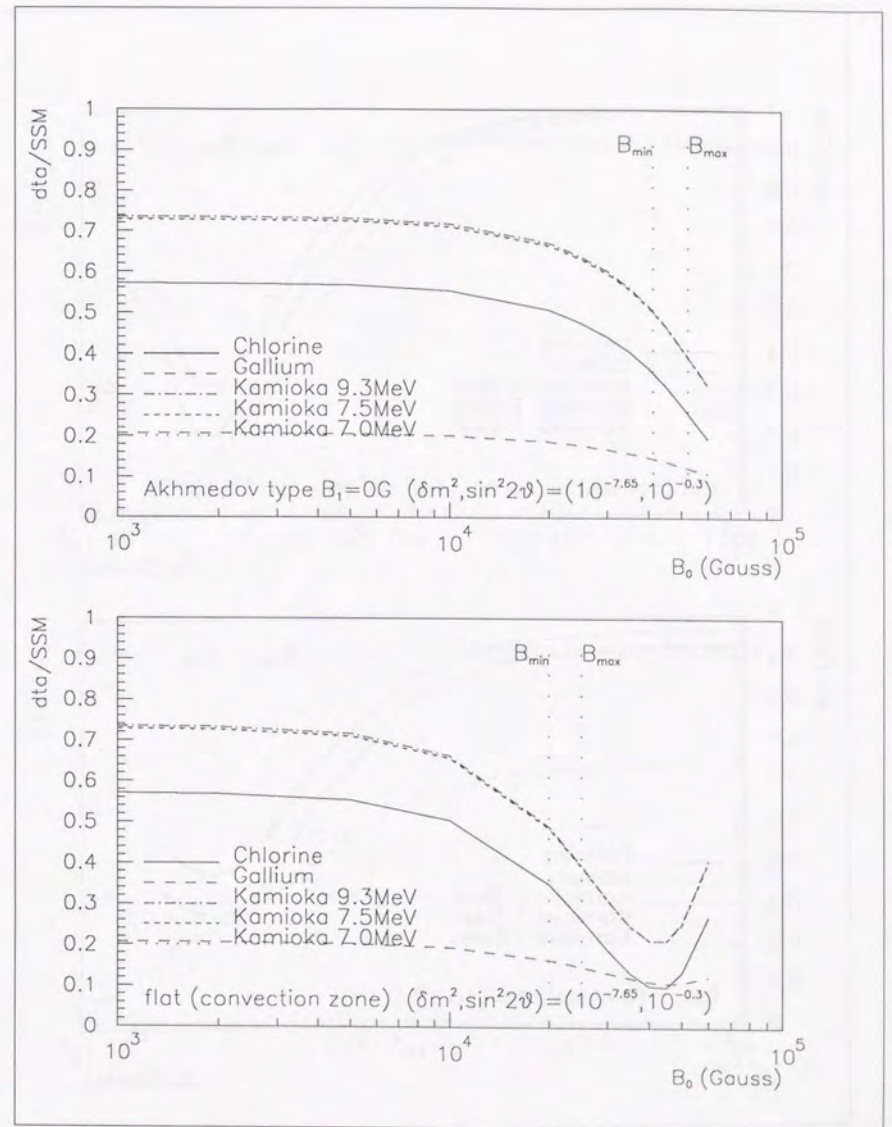


Fig. 7.23 cont.

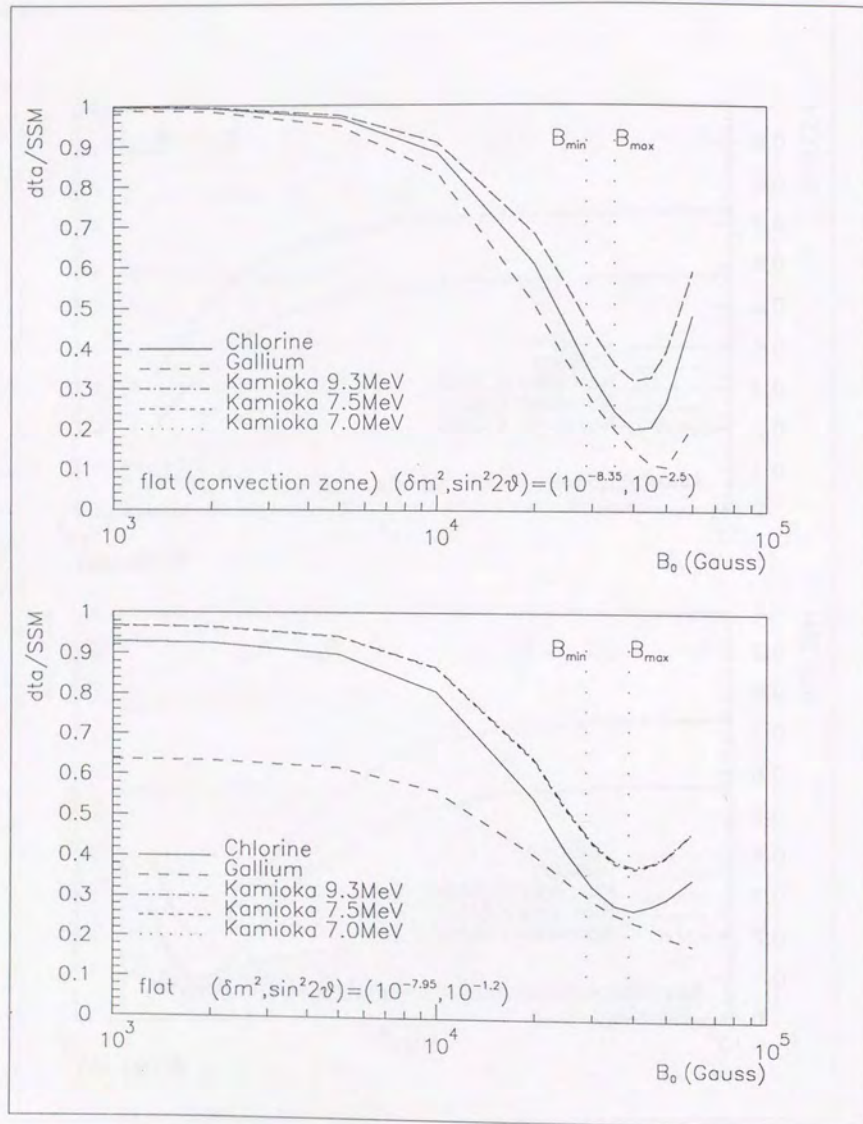


Fig. 7.23 cont.

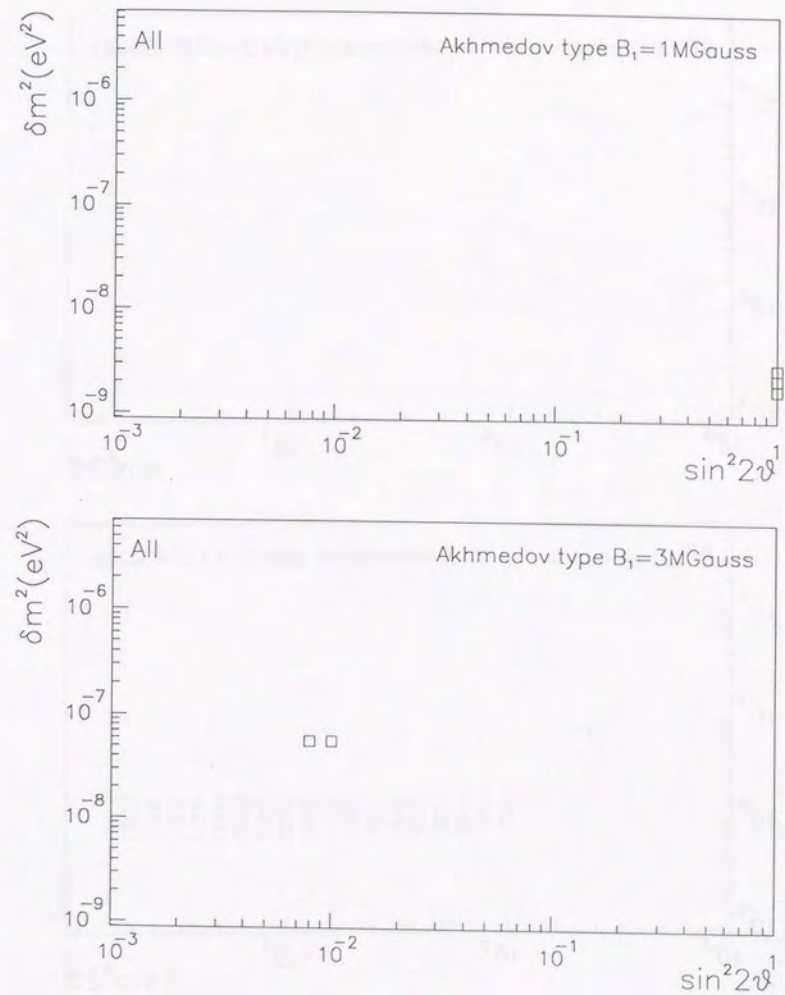


Fig. 7.24

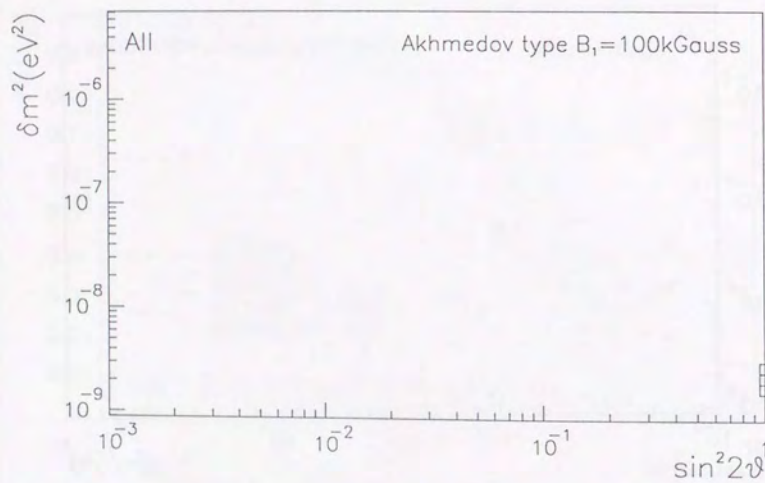
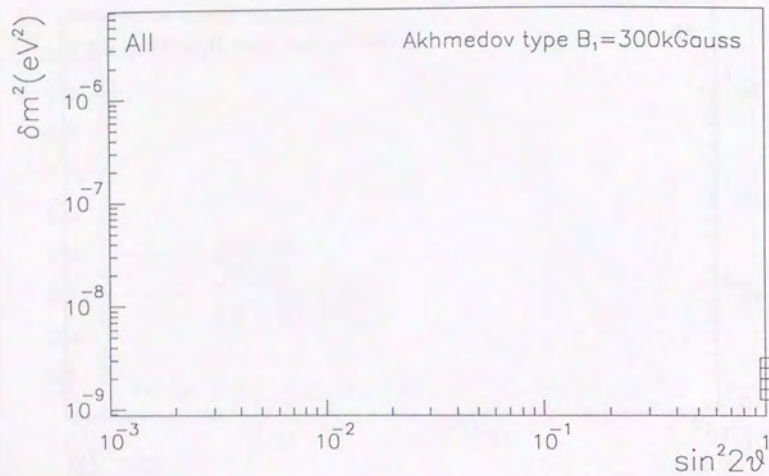


Fig. 7.24 cont.

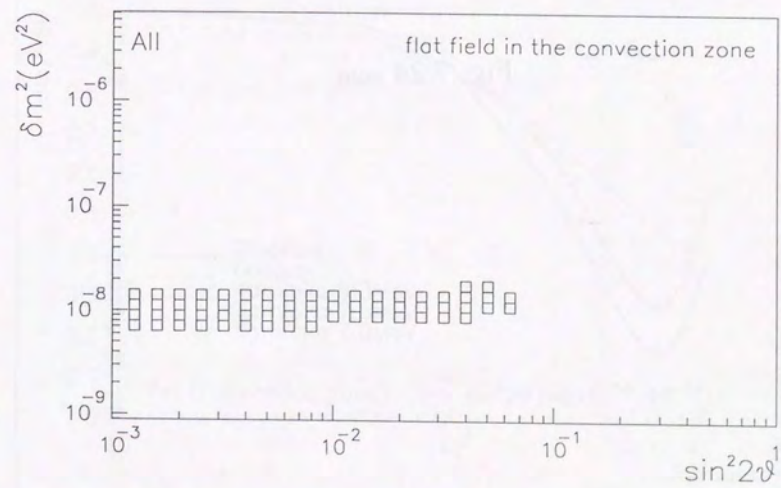
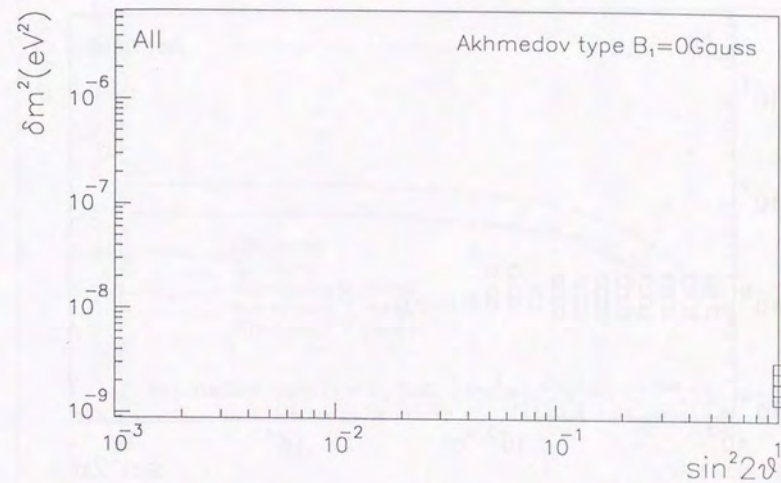


Fig. 7.24 cont.

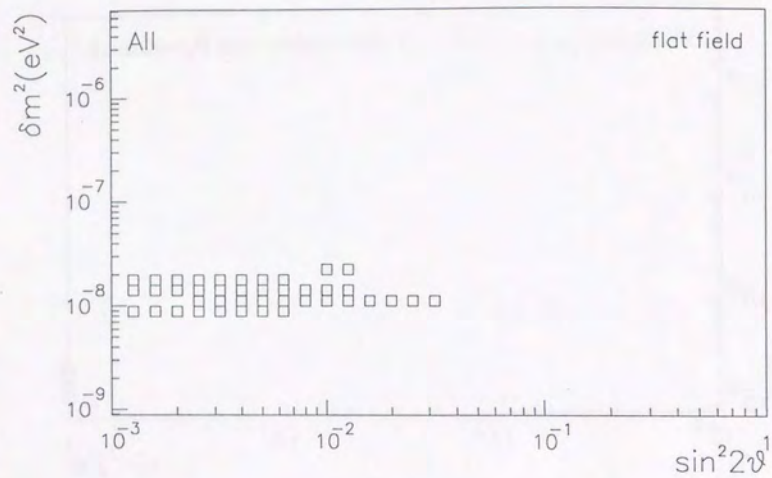


Fig. 7.24 cont.

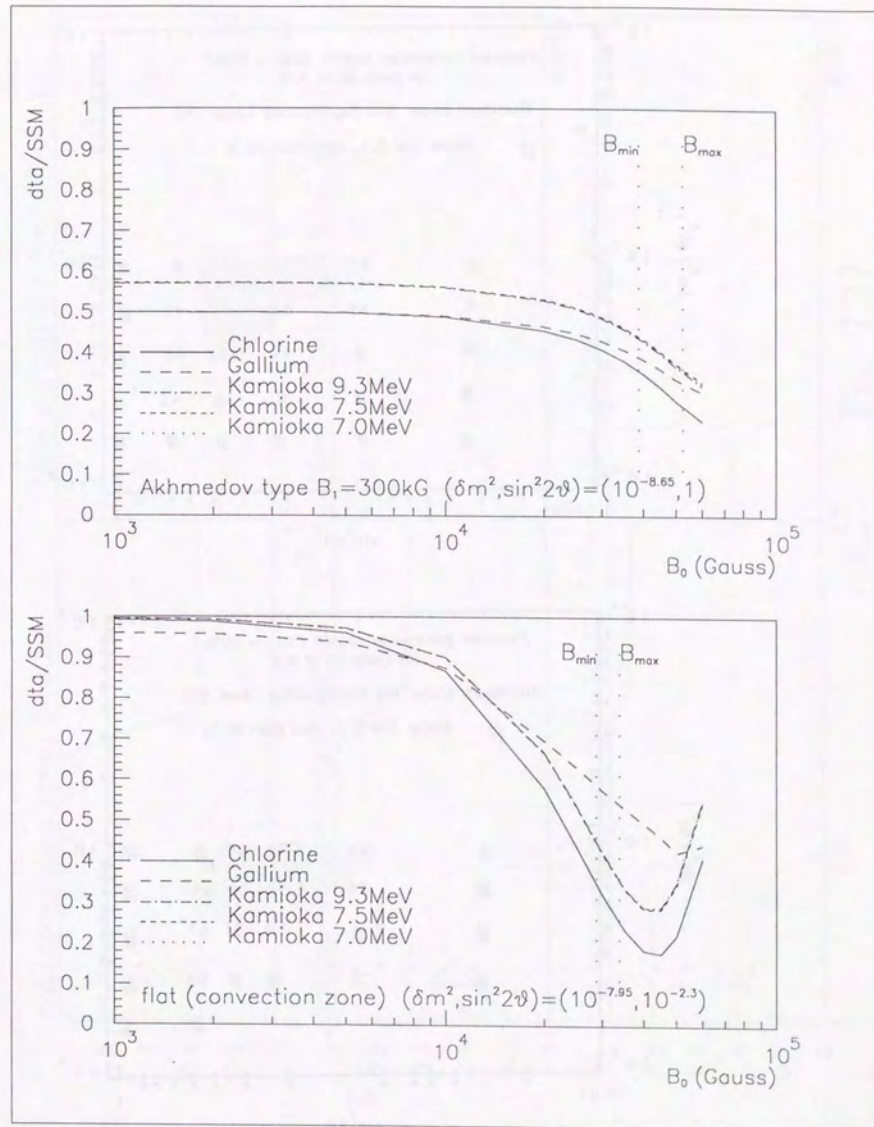


Fig. 7.25

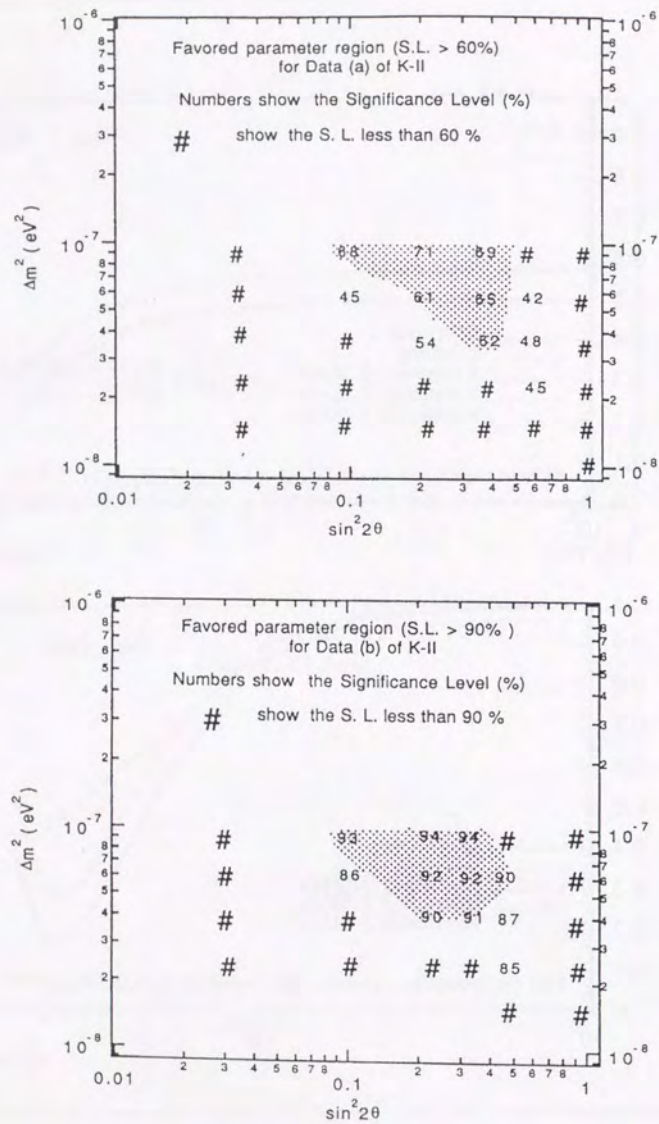


Fig. 7.26

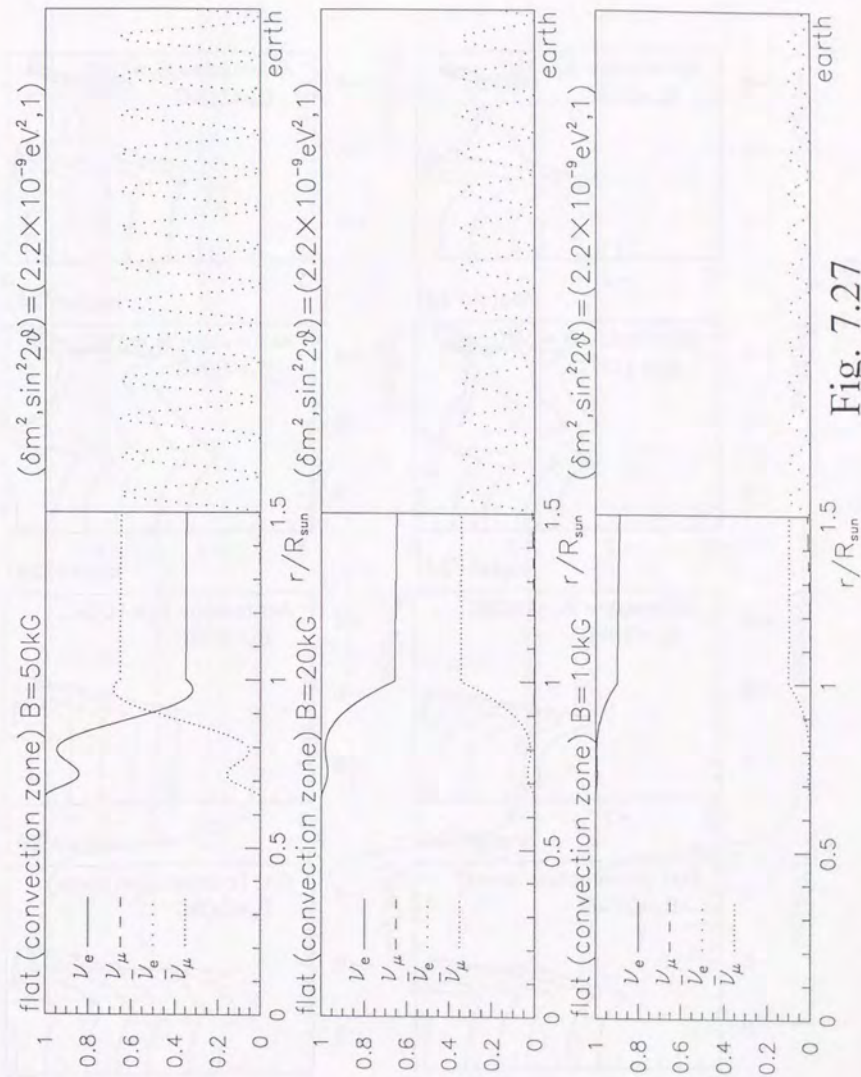


Fig. 7.27



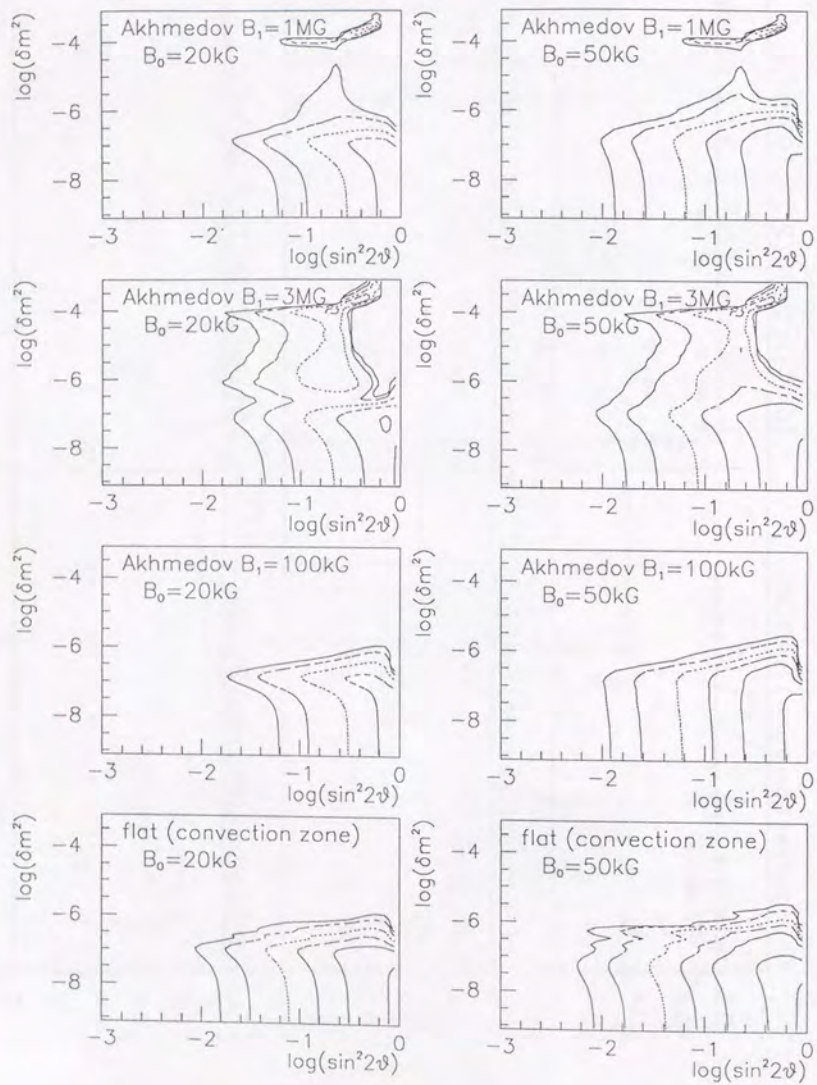


Fig. 7.28

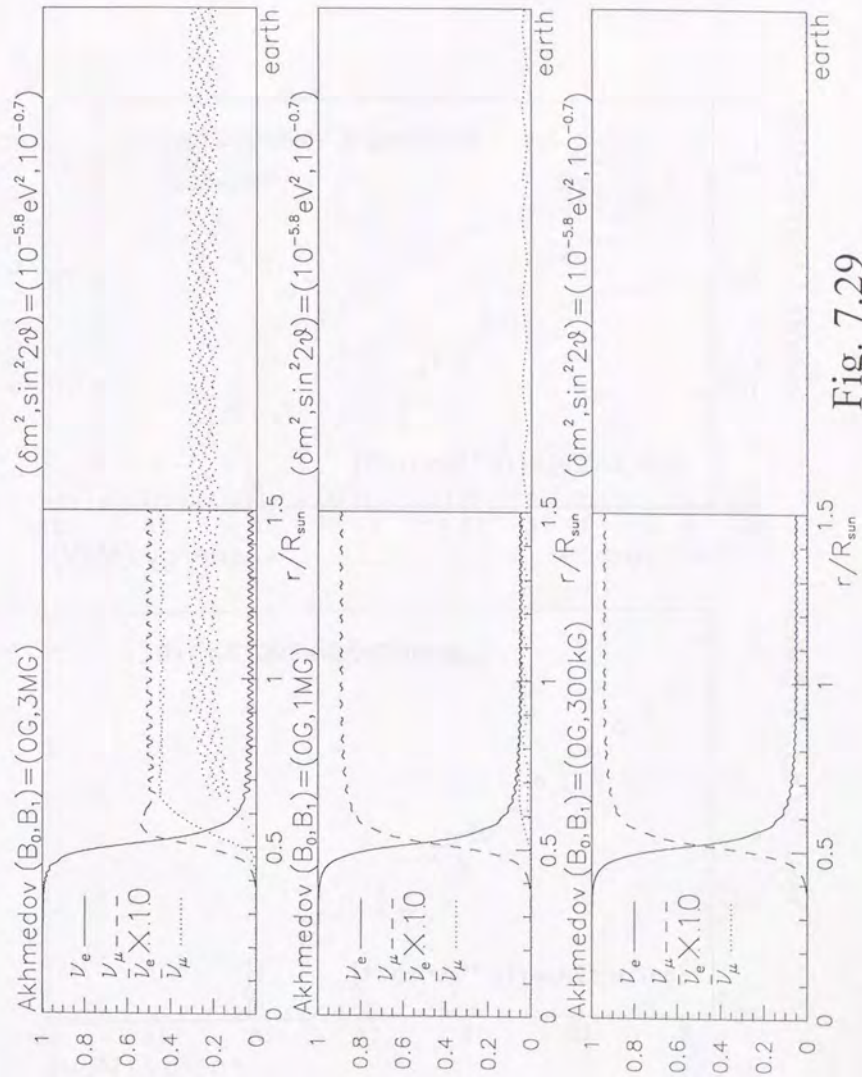


Fig. 7.29

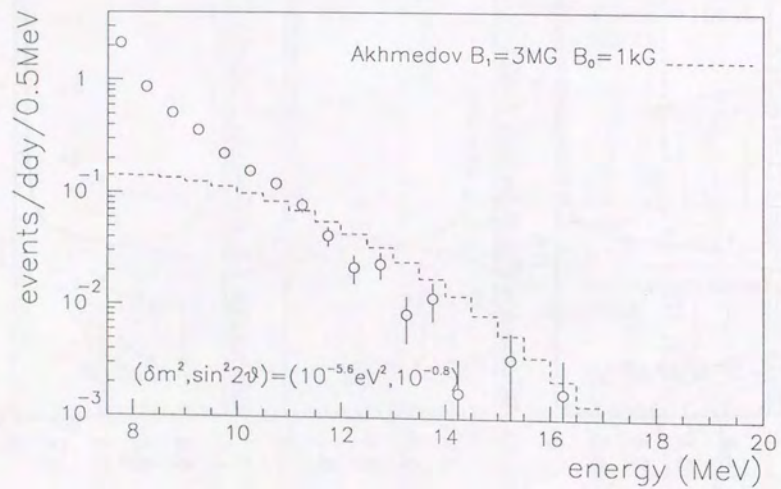
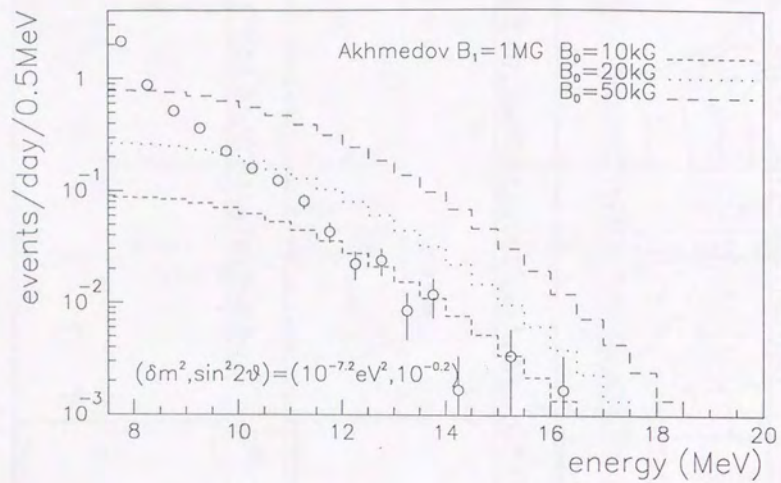


Fig. 7.30

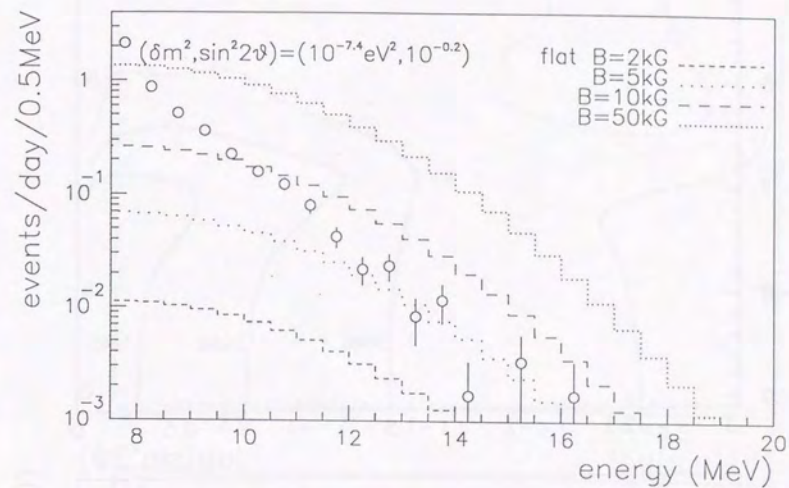


Fig. 7.30 cont.

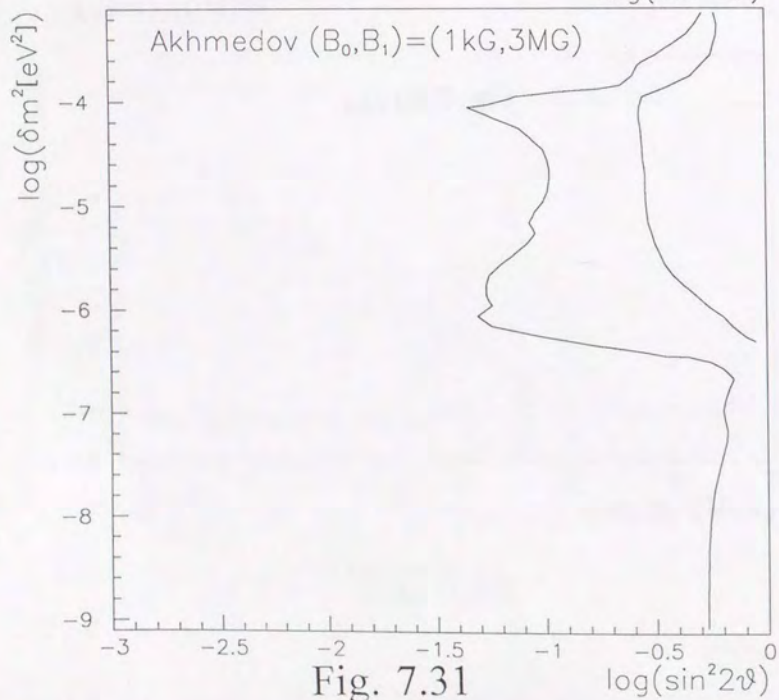
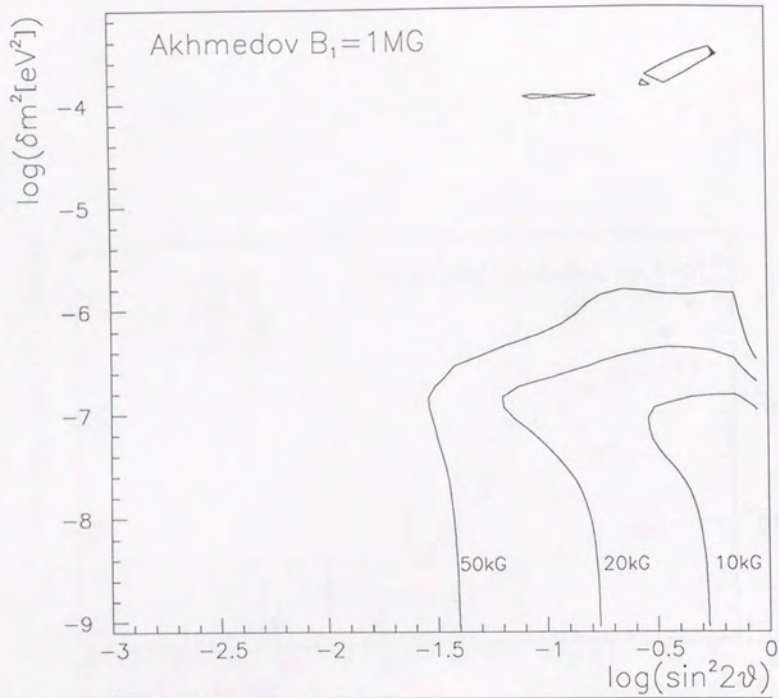


Fig. 7.31

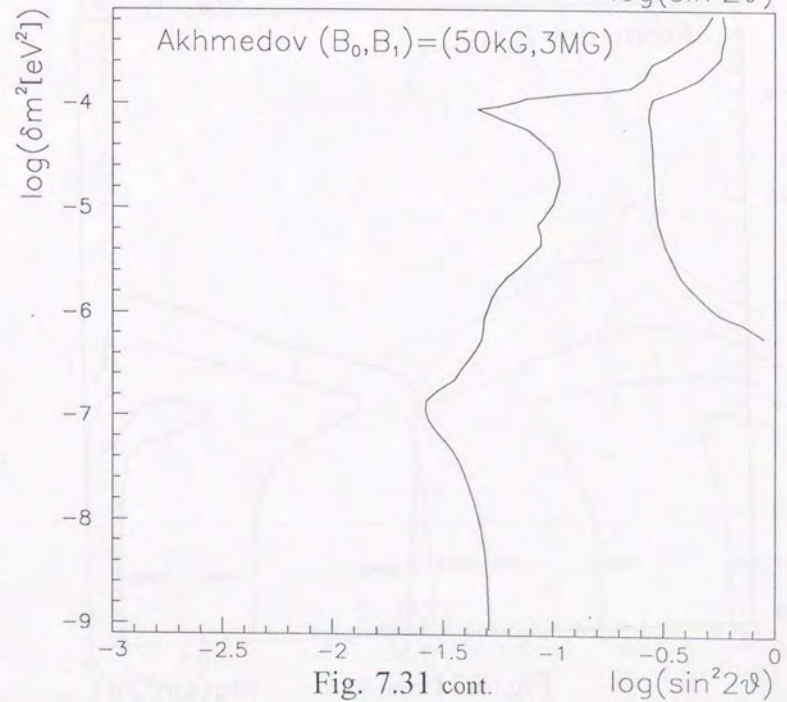
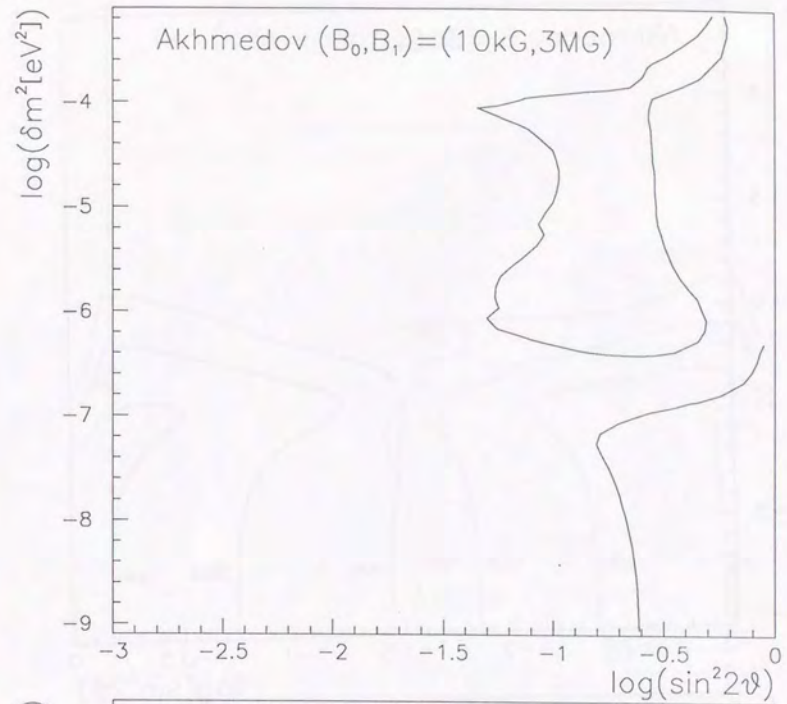


Fig. 7.31 cont.

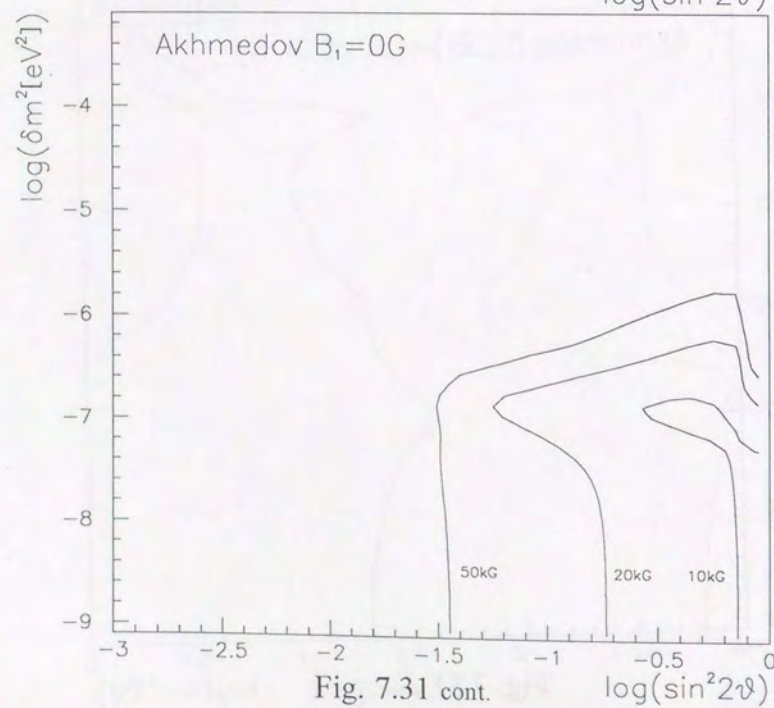
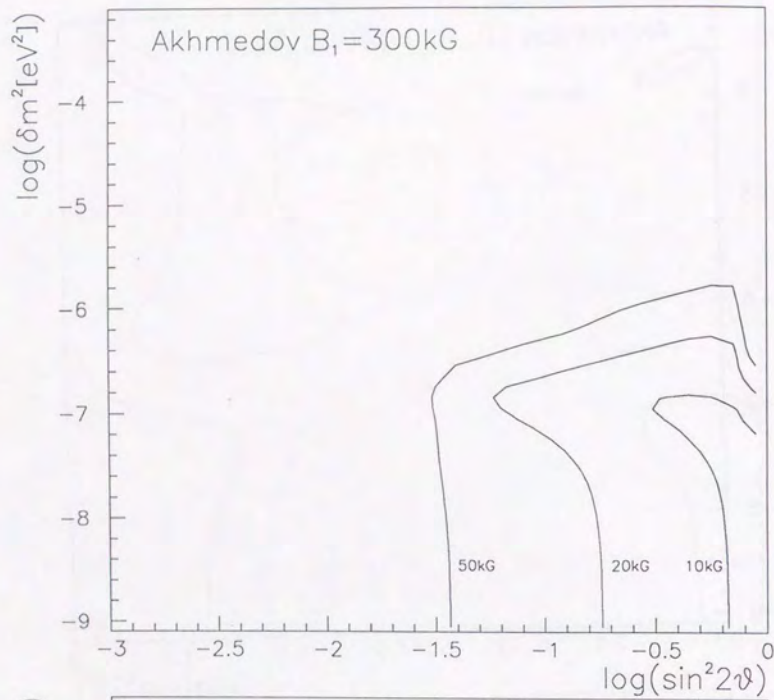


Fig. 7.31 cont.

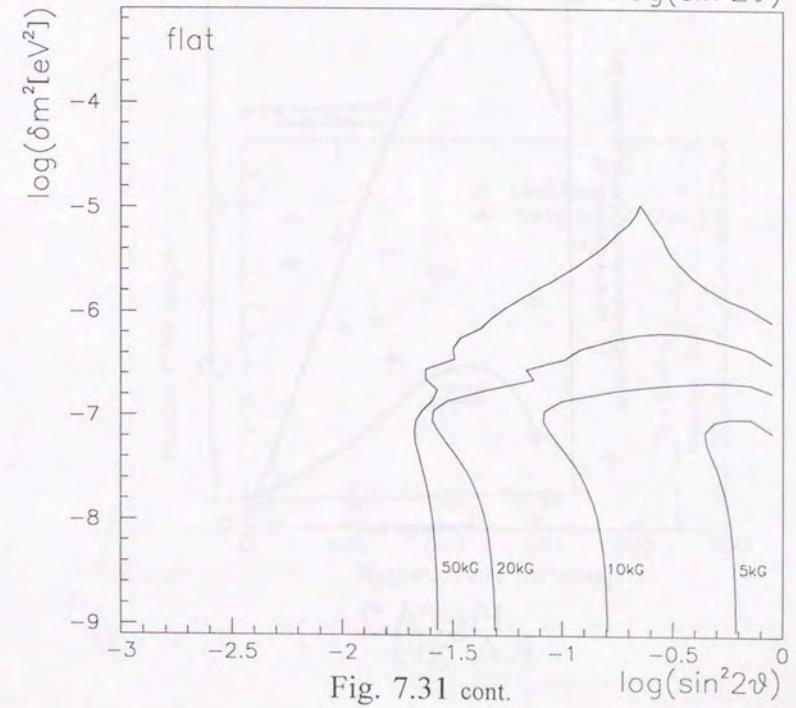
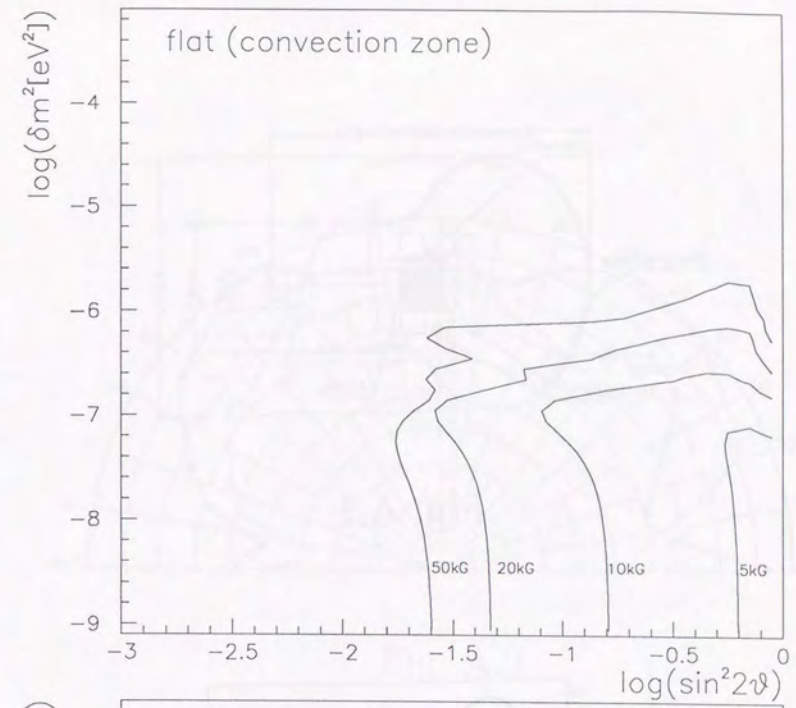


Fig. 7.31 cont.

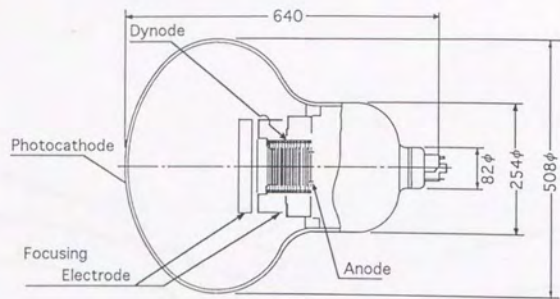


Fig. A.1

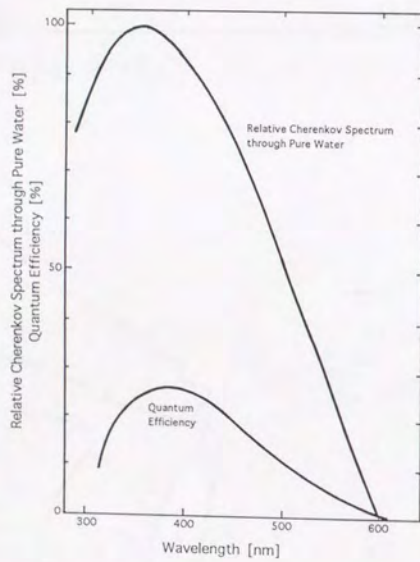


Fig. A.2

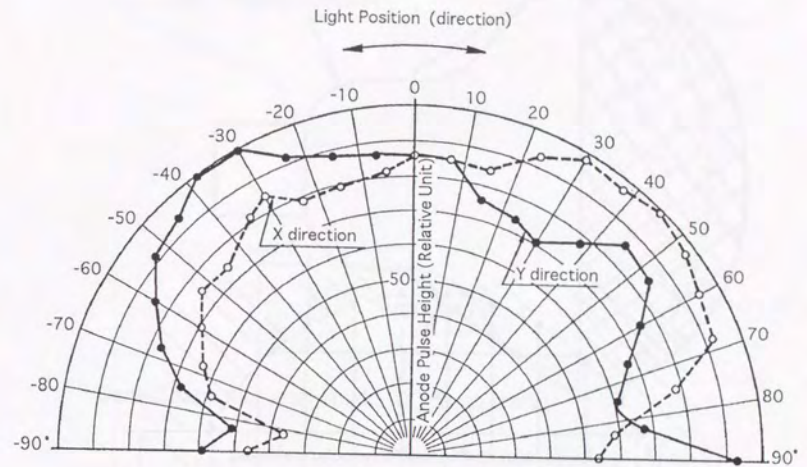


Fig. A.3

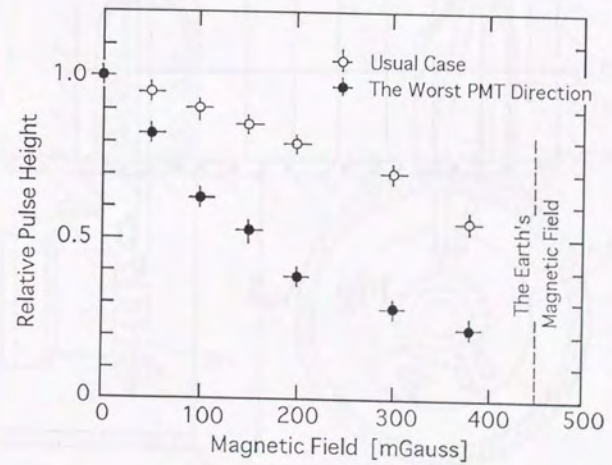


Fig. A.4

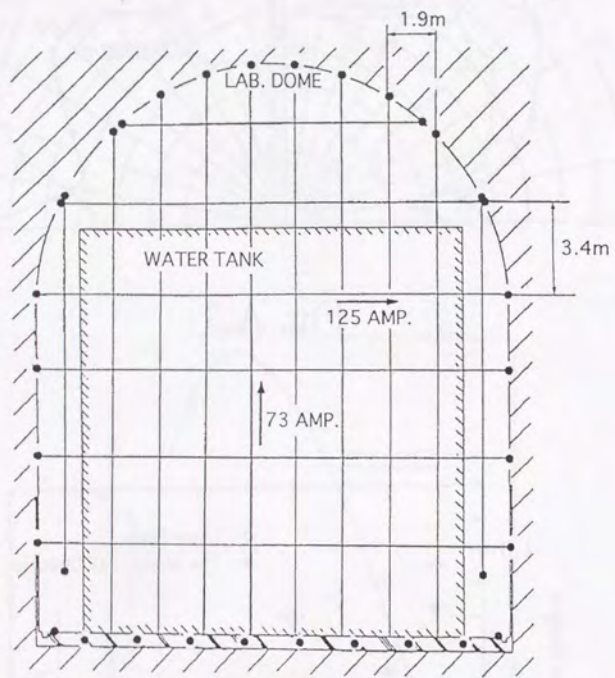


Fig. A.5

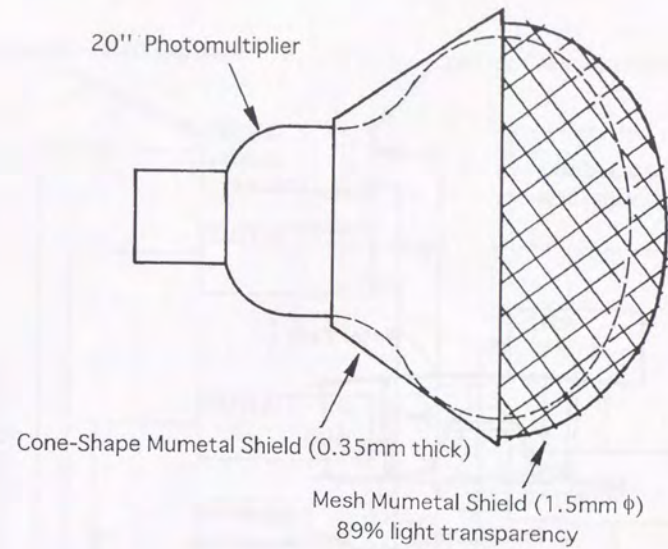


Fig. A.6

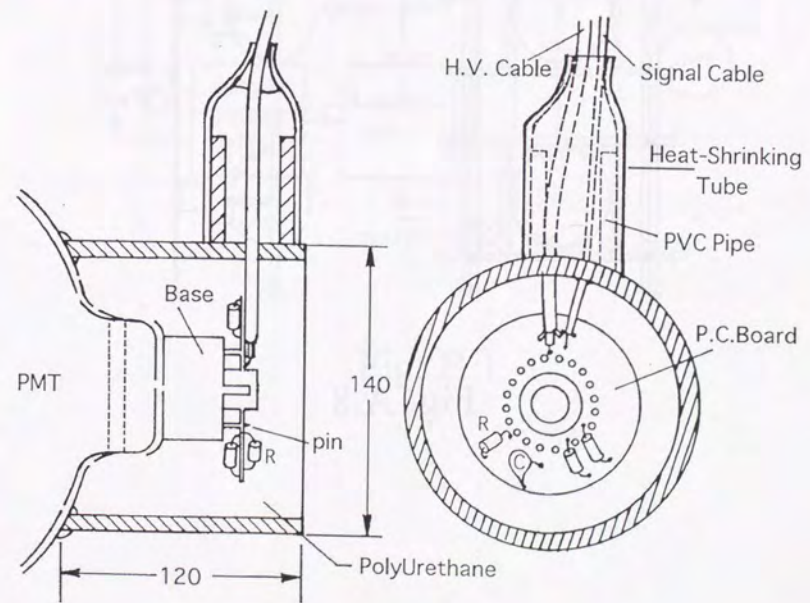


Fig. A.7

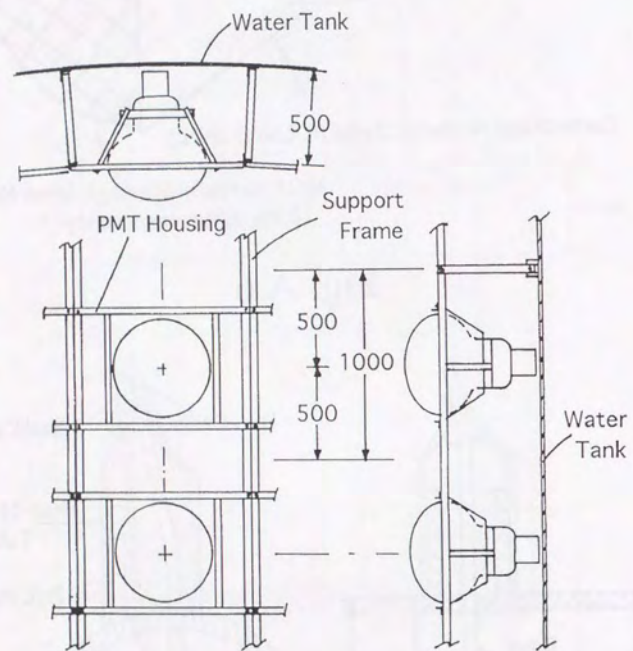


Fig. A.8

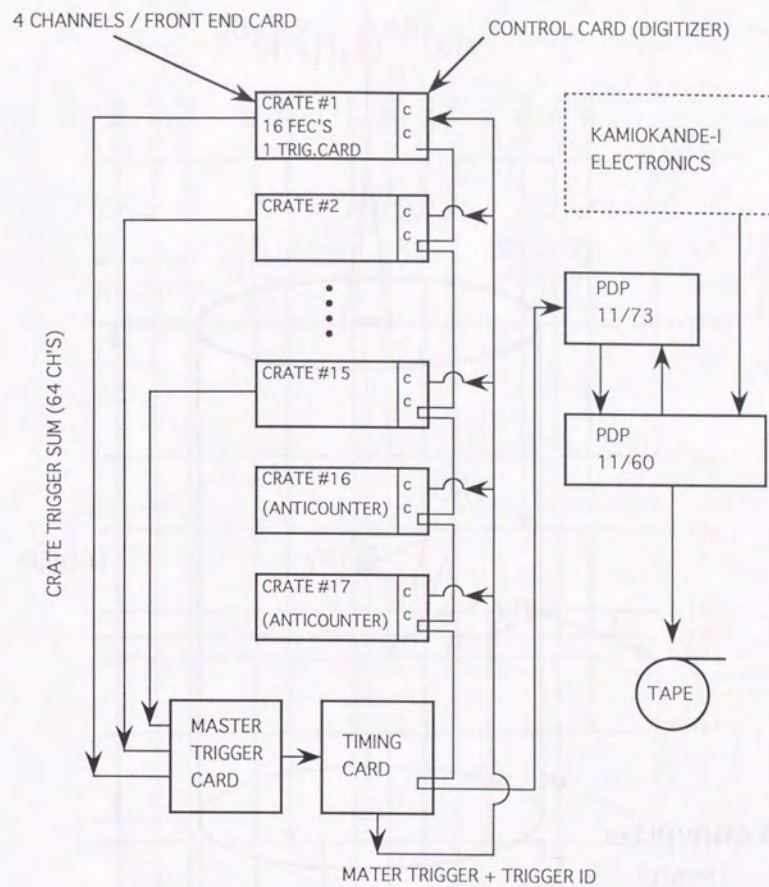


Fig. B.1

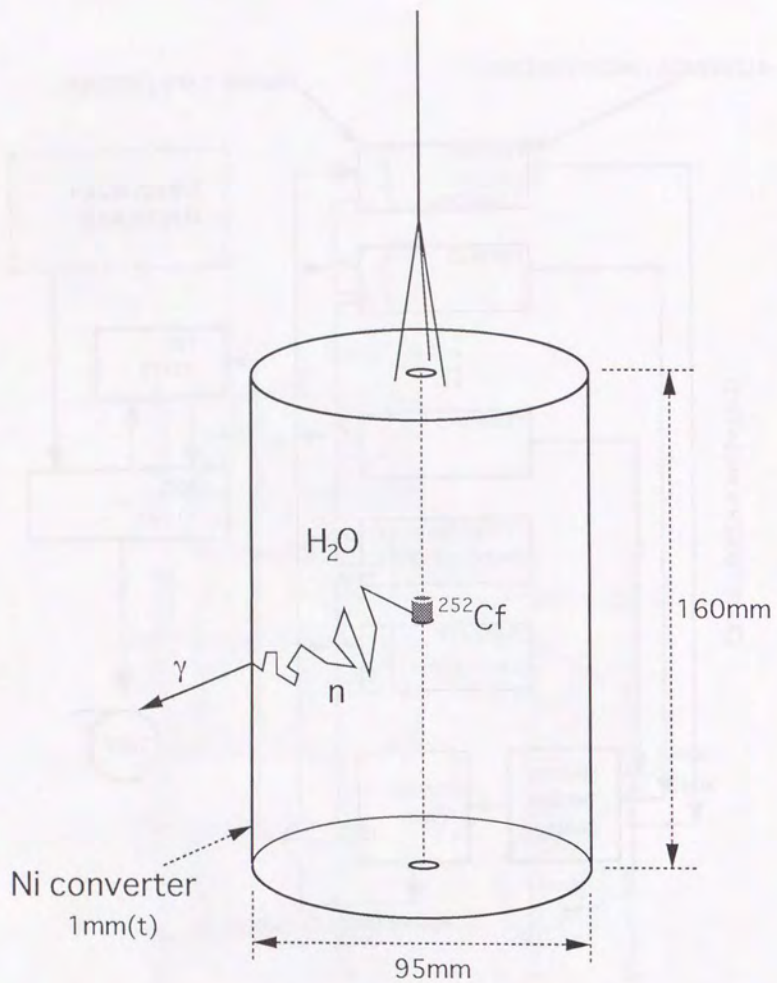


Fig. C.1

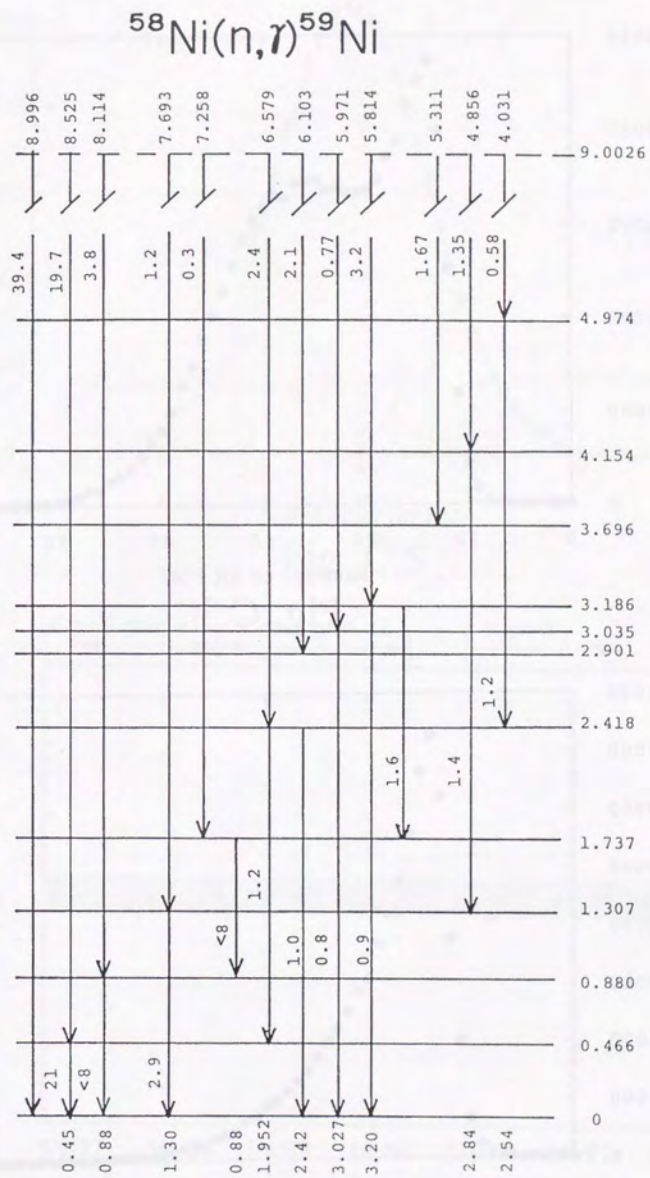


Fig. C.2



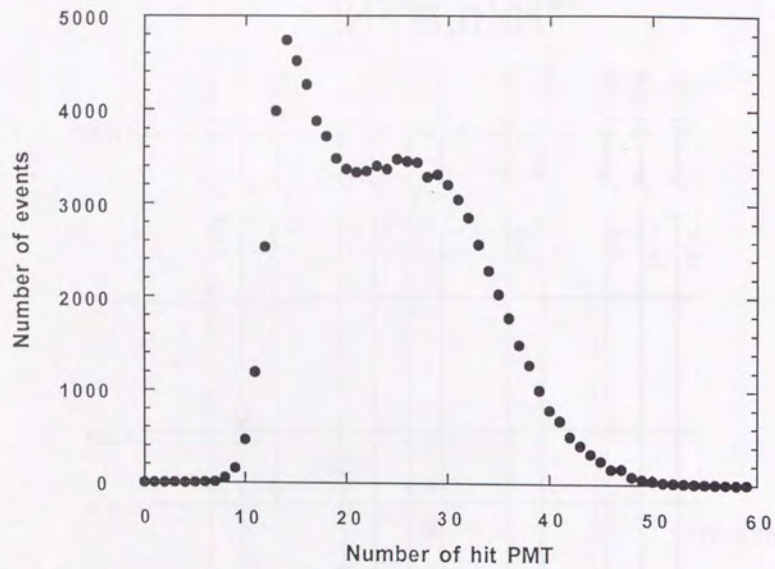


Fig. C.3

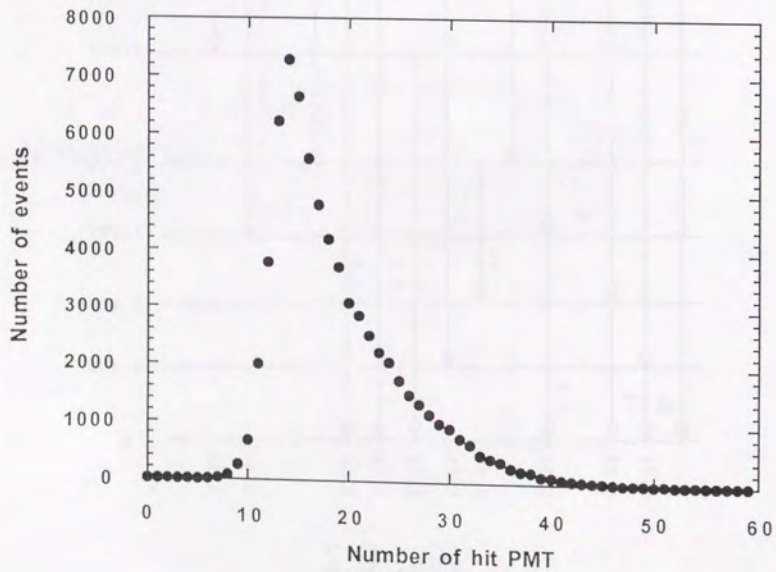


Fig. C.4

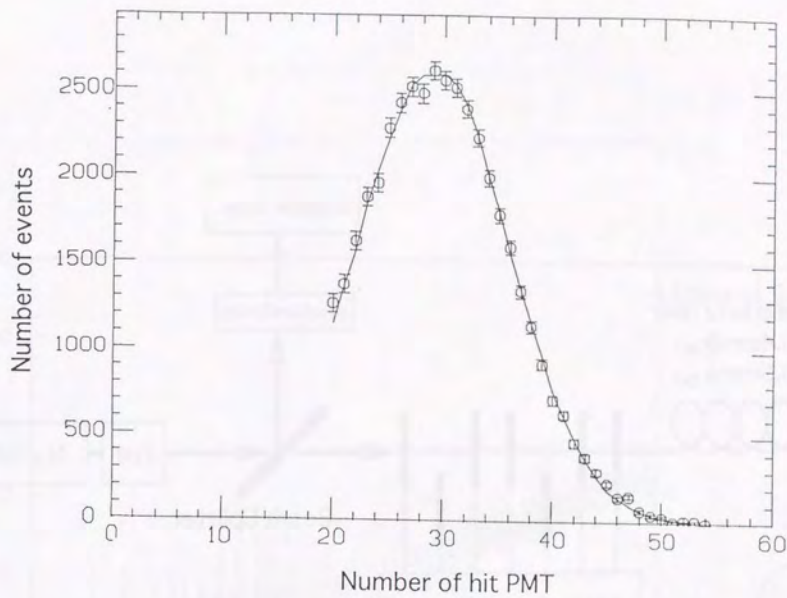


Fig. C.5

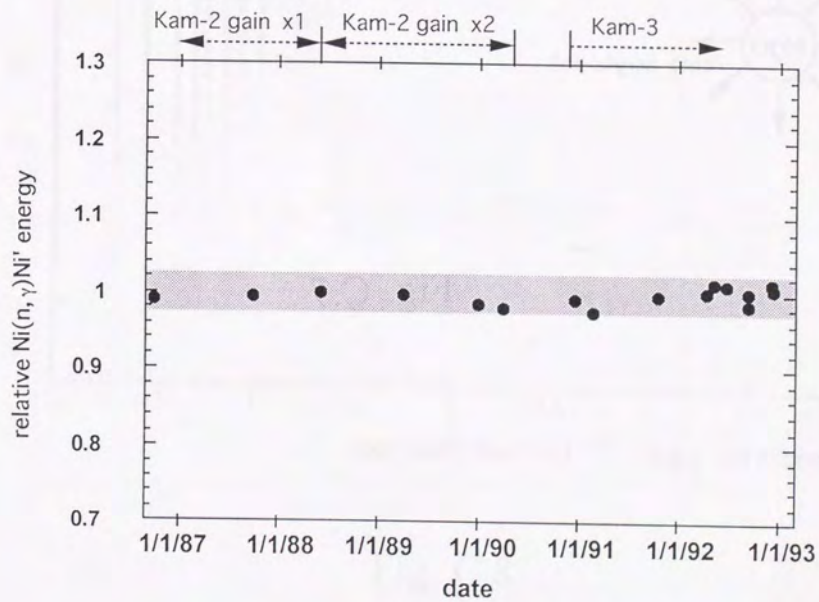


Fig. C.6

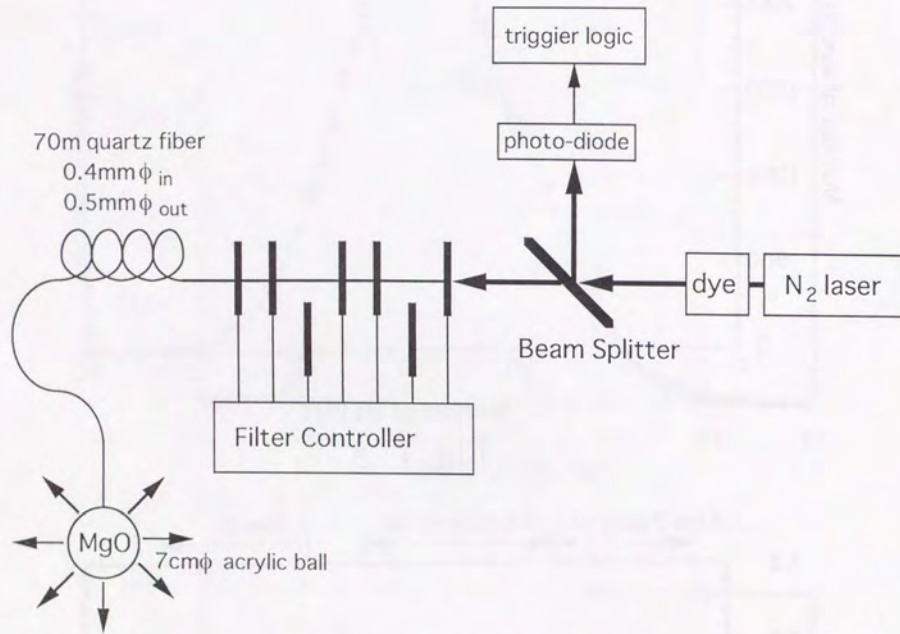


Fig. C.7

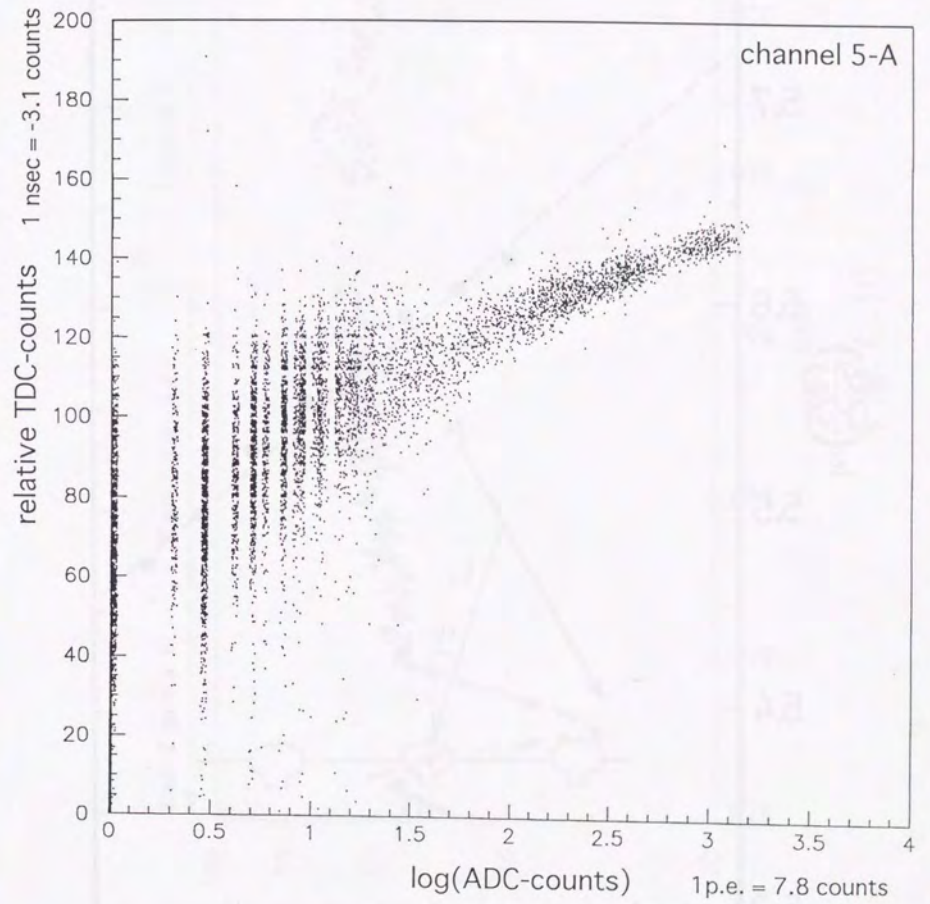


Fig. C.8

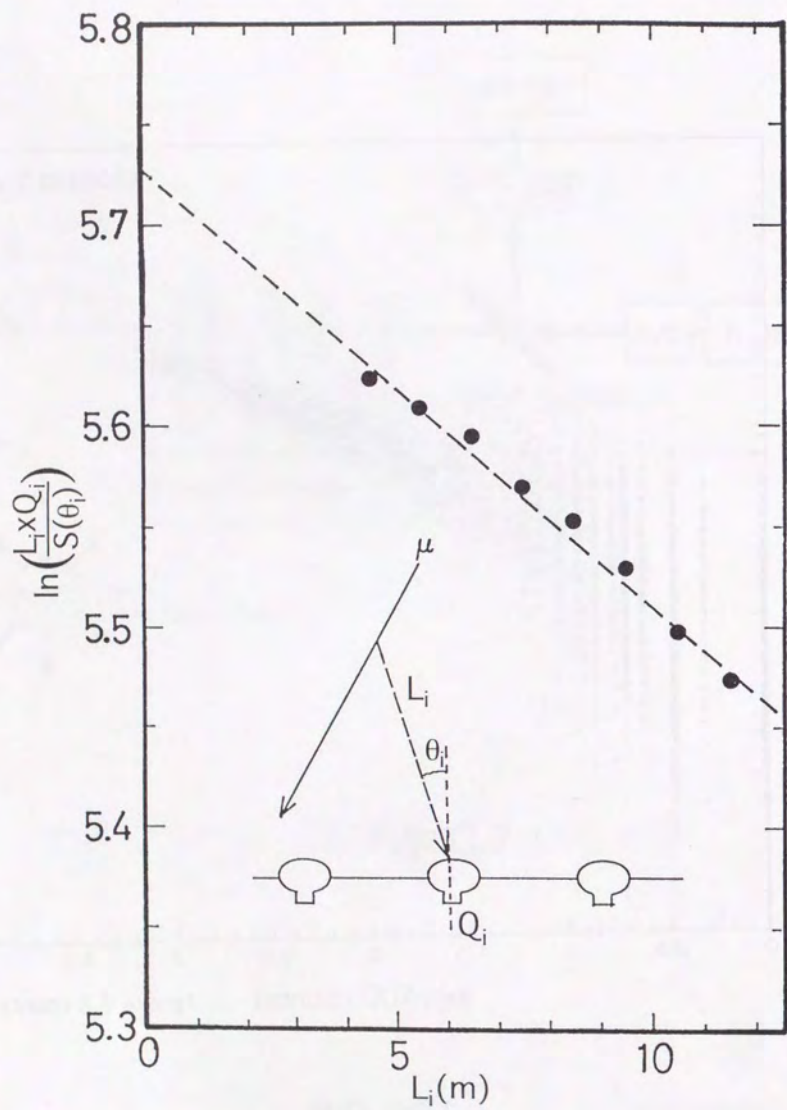


Fig. C.9

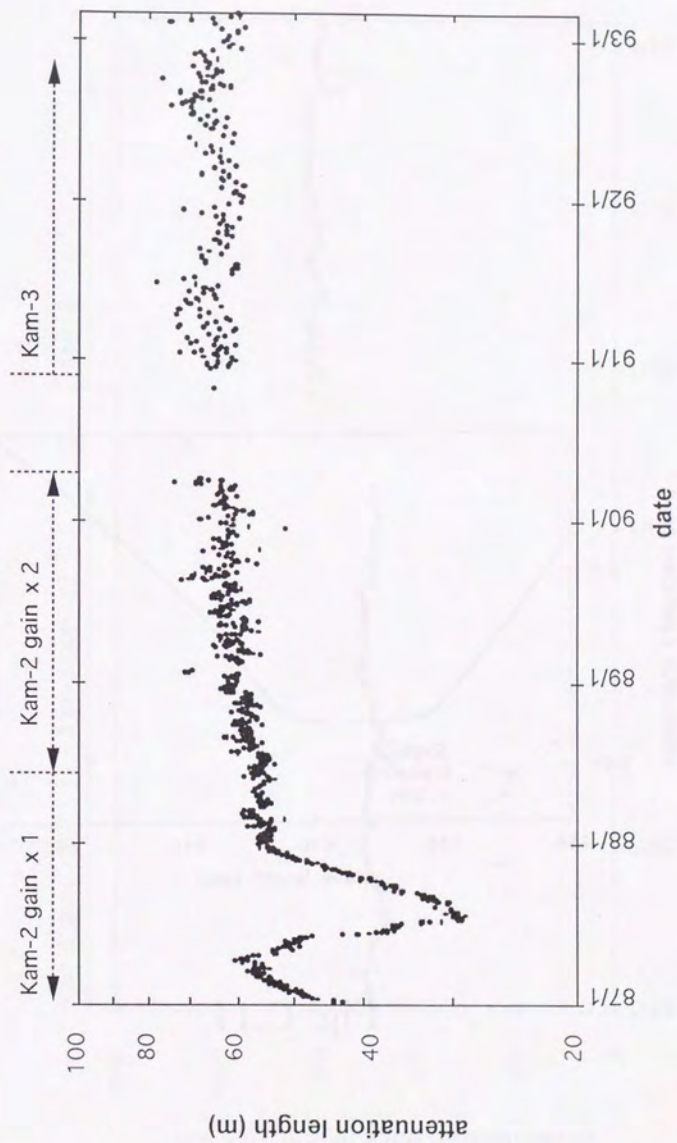


Fig. C.10

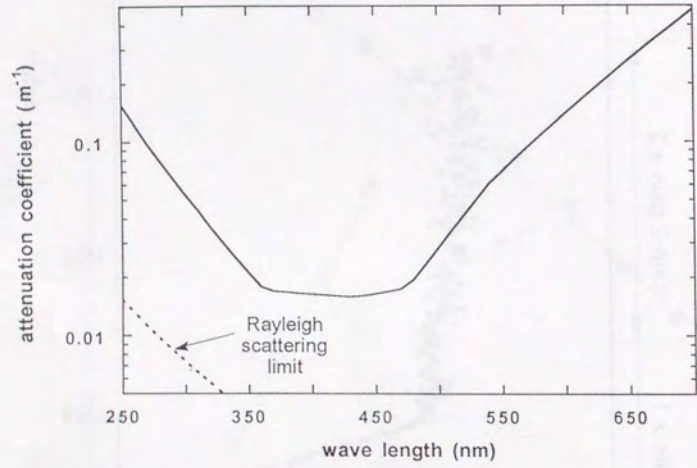


Fig. C.11

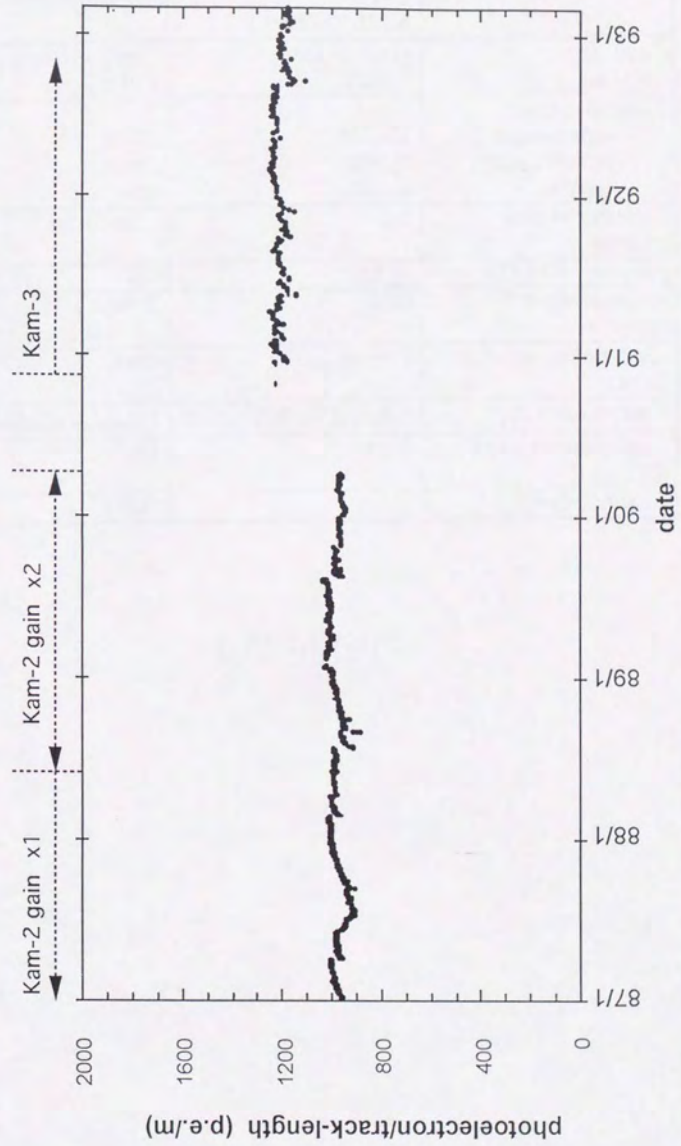


Fig. C.12

Parameters	Super-Kamiokande	Kamiokande-3
Total size	41m $\times$ 39m $\phi$	16m $\times$ 19m $\phi$
Total mass	50000t	4500t
Fiducial mass		
supernova $\nu$	32000t	2140t
proton decay	22000t	1040t
solar $\nu$	22000t	680t
Thickness of anti-counter	2m	1.2m~1.5m
Number of PMTs	11200	947
Photosensitive coverage	40%	20% $\times$ 1.27 (light reflector)
PMT timing resolution @1p.e.	2.5nsec	4nsec
Energy resolution	16% $\sqrt{E/10\text{MeV}}$	19% $\sqrt{E/10\text{MeV}}$
Position resolution @10MeV	50cm	1m
Analysis threshold	5MeV	7MeV

Table D.1

